Point defects in Aluminium Nitride for quantum technologies

Azin Aghdaei

Point defects in Aluminium Nitride for quantum technologies
Défauts ponctuels dans le nitrure d'aluminium pour les technologies quantiques

par

Azin Aghdaei

Thèse présentée au département de physique
en vue de l'obtention du grade de docteur ès science (Ph.D.)

FACULTÉ des SCIENCES

UNIVERSITÉ de SHERBROOKE

Sherbrooke, Québec, Canada, March 13, 2023

Le 13 mars 2023

le jury a accepté la thèse de Madam Azin Aghdaei dans sa version finale.

Membres du jury

Professeur Denis Morris
Directeur de recherche
Département de physique

Professeur René Côté
Membre interne
Département de physique

Professeur Richard Leonelli
Membre externe
Université de Montréal

Professeur Jeffrey Quilliam
Président rapporteur
Département de physique

To my family and friends

Science knows no country, because knowledge belongs to humanity, and is the torch which illuminates the world.

Louis Pasteur

Résumé

Les défauts ponctuels affectent fortement les propriétés électroniques et optiques des semiconducteurs : une meilleure compréhension de l'impact de ces défauts sur les performances des dispositifs basés sur ces matériaux est donc d'un grand intérêt technologique. Ces dernières années, il a été démontré que les défauts ponctuels possédaient des propriétés intéressantes pour les applications liées à l'informatique, à la détection et à la communication quantiques. Les défauts ponctuels dans l'AlN ont récemment attiré une attention considérable en raison de leur capacité à agir comme qubit pour les applications quantiques. En effet, les lacunes d'azote chargées négativement, les paires d'impuretés du groupe IV (Ge, Sn, Ti et Zr) et, plus récemment, les paires ions métalliques-lacunes (Y, La, Zr et Hf) dans l'AlN, ont été théoriquement signalées comme des candidats prometteurs pour les qubits.

Cette thèse présente le résultat de l'étude de divers nouveaux défauts ponctuels dans l'AlN pour des applications en technologie quantique. L'objectif principal de ce projet exploratoire est de déterminer l'influence de différentes espèces d'implantation et de différentes conditions de recuit thermique sur la création de défauts ponctuels dans l'AlN. Deux types de films d'AlN sont étudiés dans cette thèse, à savoir l'AlN en couche mince épitaxié sur un substrat de saphir et une couche d'AlN mince polycristallin déposé par pulvérisation cathodique sur un substrat de silicium hautement dopé.

Tout d'abord, nous avons étudié la formation de défauts dans les films d'AlN (sur le substrat de saphir), soumis à l'implantation soit d'ions d'hydrogène ou soit d'ions de titane à haute énergie, suivie d'un recuit thermique sous une sous atmosphère d'argon à différentes températures. La diffraction des rayons X et la spectroscopie Raman montrent que les espèces d'ions et le processus d'implantation peuvent modifier la quantité de déformation locale dans les films d'AlN. La spectroscopie de résonance de spin électronique révèle des pics de résonance avec une valeur de g supérieure à celle d'un électron libre (2,0023) pour les films d'AlN implantés (H ou Ti) après un recuit de 1 heure à 1050 $^{\circ}C$. L'origine de ces pics est attribuée à différents types de défauts ponctuels. Pour le film implanté Ti-, en plus du pic central, un pic de résonance à la demie valeur du champ magnétique a été détecté et attribué à un triplet de spin (S=1) qui pourrait être intéressant pour des applications quantiques.

Les propriétés optiques des défauts dans les films AlN implantés en H et en Ti ont été étudiées à l'aide d'un configuration de photoluminescence conventionnelle via une excitation à 532 nm et à 266 nm. En raison du niveau élevé du signal de fond qui provient très probablement du substrat de saphir, nous n'avons pas pu détecter de signal de luminescence en provenance de

défauts ponctuels isolés dans l'AlN. Nous avons donc décidé de concentrer le reste de nos études à des films d'AlN sur un substrat de silicium fortement dopé.

Ces films substrat de silicium ont été implantés avec des ions hydrogène, titane, zirconium, et hafnium. Afin de réparer partiellement les dommages structurels causés par le bombardement ionique, les échantillons implantés ont été recuits à différentes températures et sous différentes atmosphères, notamment de l'argon, l'azote et le gaz mélange (désigné forming gaz en anglais avec l'acronyme (FG, 95 % d'azote + 5 % d'hydrogène). Nos résultats montrent que les spectres de photoluminescence de la plupart des échantillons recuits et du film d'AlN sont très similaires ce qui montre qu'aucun nouveau défaut n'a été introduit dans l'AlN. La seule exception concerne les films AlN implantés de Zr.

Pour les films d'AlN soumis à l'implantation d'ions Zr à haute énergie, des mesures de diffraction des rayons X, de spectroscopie Raman, de microscopie électronique à balayage et de microscopie à force atomique montrent que les propriétés structurelles et morphologiques des films AlN implantés au Zr dépendent de l'environnement gazeux du recuit thermique. Le recuit post-implantation sous atmosphère d'argon donne une rugosité de surface la plus faible avec une taille de grain accrue tandis que les échantillons recuits sous atmosphère de FG ont montré un niveau élevé de récupération des dommages et la plus faible quantité d'oxygène en proximité de la surface. La spectroscopie de photoluminescence a révélé de multiples défauts ponctuels et des bandes d'émission liées aux complexes de défauts dans la gamme visible. Une série de bandes d'absorption a été observées en utilisant la spectroscopie d'excitation par photoluminescence. En comparaison avec le film d'AlN tel que déposé, de nouveaux pics d'émission et d'absorption à 1.7 eV (730 nm) et 2.6 eV (466 nm), respectivement, ont été identifiés et attribués aux complexes de défauts $(Zr_{Al} - V_N)^0$.

Afin d'étudier l'émission de ces complexes de défauts $(Zr_{Al} - V_N)^0$, nous avons conçu un montage micro-PL au sein de notre équipe de recherche. En utilisant ce montage, les propriétés optiques des émetteurs dans les films d'AlN implantés en Zr ont été étudiées. Le but de cette étude était d'examiner le potentiel de ces défauts ponctuels pour des applications aux sources de photons uniques. Par conséquent, nous avons choisi les échantillons qui ont été recuits sous atmosphère de gaz mélange FG en raison de leurs faibles dommages structurels et du faible niveau d'oxygène présent en surface. Nos résultats révèlent des points brillants de taille micrométrique avec une raie fine sans phonon (ZPL) à 4 K autour de 685.5 nm (1.808 eV) et une bande latérale phononique de plus faible énergie visible autour de 700 nm. Sur la base de nos études précédentes, ces raies sont attribuées aux complexes $(Zr_{Al} - V_N)^0$. Nos résultats ont montré un facteur de Debye-Waller relativement élevé autour de 18,5% à 4K, ce qui pourrait être intéressant pour les applications quantiques à photons uniques. Cependant, pour étudier

le potentiel de ces défauts en tant qu'émetteurs de photons uniques, une mesure d'antibunching $g^{(2)}(\tau)$ est fortement recommandée.

Nos recherches sur les films d'AlN implantés avec Hf et Ti n'ont pas révélé l'apparition de nouveaux pics de PL. De plus, aucun signal ESR n'a été détecté dans ces échantillons. Ce manque de signal pourrait être attribué à la température de recuit relativement basse utilisée dans notre étude, qui pourrait ne pas avoir été suffisante pour permettre une récupération complète des films d'AlN endommagés par l'implantation. La structure cristalline différente du film d'AlN pourrait également avoir joué un rôle dans l'absence de signal ESR. De plus, la faible concentration de défauts paramagnétiques présents dans les échantillons pourrait également avoir contribué à l'absence de signal.

Il est important de noter que notre étude n'a pas totalement exclu la possibilité d'apparition de pics de PL ou de signaux ESR avec des températures de recuit plus élevées ou différents paramètres d'implantation. Des investigations supplémentaires sur les effets de la variation de ces paramètres sur les propriétés des films d'AlN implantés avec Hf et Ti pourraient fournir des informations précieuses sur le comportement de ces matériaux dans différentes conditions.

D'un point de vue général, les résultats de la présente étude montrent que l'ingénierie des défauts ponctuels dans l'AlN est intéressante pour les applications quantiques ainsi que pour le développement de matériaux optoélectroniques. Des améliorations doivent encore être apportées à ces procédés afin d'augmenter la densité de ces défauts ponctuels, tout en minimisant la présence d'agrégats de défauts et l'apparition d'un fort niveau de signal de PL large-bande.

ABSTRACT

Point defects strongly affect the electronic and optical properties of semiconductors: a better understanding of the impact of these defects on the performance of devices based on these materials is therefore of great technological interest. Over recent years, point defects have been shown to possess properties of interest for applications related to quantum computing, sensing, and communication. Point defects in AlN recently attracted considerable attention due to their ability to act as a qubit for quantum applications. Indeed, negatively charged nitrogen vacancies, group IV impurity (Ge, Sn, Ti, and Zr)–vacancy pairs, and, more recently, large metal ion (Y, La, Zr, and Hf)–vacancy pairs in AlN, have been theoretically reported as promising qubit candidates.

This thesis presents the result of the study of various new point defects in AlN for quantum technology applications. The main goal of this exploratory project is to determine the influence of different implantation species and different thermal annealing conditions on the creation of point defects in AlN. Two types of AlN films were studied in this thesis, namely, single crystal AlN on the sapphire substrate and polycrystalline AlN layer on a highly-doped silicon substrate.

First, we studied the formation of defects in AlN films (on the sapphire substrate), subjected to high-energy hydrogen and titanium ion implantation followed by thermal annealing under argon atmosphere at different temperatures. X-ray diffraction and Raman spectroscopy show that ion species and the implantation process could alter the amount of local strain in AlN films. Electron spin resonance spectroscopy reveals resonance peaks with g-value higher than that one of a free electron (2.0023) for both H-implanted and Ti-implanted AlN films after annealing for 1h at 1050 $^{\circ}C$. The origin of these peaks is attributed to different types of point defects. For the Ti-implanted film, in addition to the central peak, a half-field resonance peak has been detected and assigned to spin-triplet (S=1), which might be interesting for quantum applications.

The optical properties of defects in H-implanted and Ti-implanted AlN films were studied using a conventional PL setup exciting at 532 nm and 266 nm. It should be noted that the PL studies of the samples revealed a broad background, which could be associated with the sapphire substrate. This broad peak could potentially mask the PL peaks originating from point defects in AlN. Therefore, our subsequent studies will focus on the AlN films grown on highly doped Si substrates. Consequently, we have not examined the effects of Zr and Hf implantation on these AlN films.

AlN on the silicon substrate films were implanted with hydrogen, titanium, zirconium, and Hafnium ions. To partially repair the structural damage caused by ion bombardment, the implanted samples were annealed at different temperatures and under different atmospheres including argon, nitrogen, and forming gas (FG, 95 % nitrogen + 5 % hydrogen). Our results show that the photoluminescence spectra of most of the annealed samples and the as-grown AlN films are very similar, which demonstrates that no new defects were introduced in AlN. The only exception was the Zr-implanted AlN films.

For the AlN films subjected to high-energy Zr ion implantation, the X-ray diffraction, Raman spectroscopy, scanning electron microscopy, and atomic force microscopy measurements show that the structural and morphological properties of the Zr-implanted AlN films depend on the annealing gaseous environment. Post-implantation annealing under argon atmosphere yields the lowest structured surface roughness with increased grain size while the samples annealed under the forming gas atmosphere showed a high level of damage recovery and the lowest amount of oxygen in close proximity to the surface. Photoluminescence spectroscopy revealed multiple point defects and defect complexes related to emission bands in the visible range. A series of absorption bands have been observed using photoluminescence excitation spectroscopy. Compare to as-deposited AlN film, new emission and absorption peaks at 1.7 eV (730 nm) and 2.6 eV (466 nm), respectively, have been identified and attributed to the $(Zr_{Al} - V_N)^0$ defect complexes.

To study the emission from $(Zr_{Al} - V_N)^0$ defect complexes, we designed a micro-PL setup whitin our research team. Using this setup, the optical properties of the emitters in Zr-implanted AlN films were studied. The study aimed to investigate the potential of these point defects for single photon emitter, applications. Hence, we chose the samples annealed under forming gas atmosphere due to their lower structural damage and the lowest level of oxygen at the surface. Our results reveal micrometer-sized bright spots with ZPL at 4 K at 685.5 nm (1.808 eV) and a lower energy phonon sideband around 700 nm. Based on our previous studies these spots are assigned to the $(Zr_{Al} - V_N)^0$ defect complexes. Our results showed a relatively high Debye-Waller factor of around 18.5% at 4K, which might be interesting for quantum single-photon source applications. However, to investigate the potential of these defects as single-photon emitters an antibunching $g^{(2)}(\tau)$ measurement is highly recommended.

Our investigations into Hf and Ti-implanted AlN films on highly doped Si, did not reveal the emergence of any new PL peaks. Additionally, no ESR signal was detected in these samples. This lack of signal could be attributed to the relatively low annealing temperature employed in our study, which may not have been sufficient to facilitate the complete recovery of the AlN films from the damage caused by implantation. The different crystal structures of the AlN film may

have also played a role in the absence of an ESR signal. Furthermore, the low concentration of paramagnetic defects present in the samples could have also contributed to the lack of signal. It is important to note that our study did not entirely rule out the possibility of PL peaks or ESR signals appearing with higher annealing temperatures or different implantation parameters. Further investigation into the effects of varying these parameters on the properties of Hf and Ti-implanted AlN films could provide valuable insights into the behavior of these materials under different conditions.

Taken as a whole, the findings of this study underscore the importance of manipulating point defects in AlN for the purpose of advancing quantum applications and the development of optoelectronic materials. However, further refinements are necessary to enhance the density of these point defects, while concurrently minimizing the incidence of defect clusters and the occurrence of a high broadband PL signal level. Such improvements will be vital in ensuring the optimal performance of AlN-based devices for various applications, including sensing, photonics, and quantum information processing.

Acknowledgment

When writing a PhD thesis, one must rely on the help and support of numerous individuals. I am immensely grateful to all those who provided assistance during this journey, including those whose names are not mentioned here.

I would like to extend my special thanks to Professor Denis Morris, who gave me the opportunity to pursue my PhD within his research team. His expertise, knowledge, and passion for science were crucial in completing this work, and I am deeply appreciative of his guidance. I also admire his personality and the way he cares for his students.

I wish to express my gratitude to Professor Jeffrey Quilliam and Professor René Côté, who served on my thesis committee, for their valuable contributions through their insightful questions, remarks, and suggestions. I also want to acknowledge and thank Professor Richard Leonelli for accepting the role of the external examiner for my thesis.

Additionally, I express my gratitude to Professor François Schiettekatte and Dr. Martin Chicoine for their valuable contributions in ion implantation of AlN films and paper writing guidance. I thank Professor Luc G. Frechette, and Dr. Rajesh Pandiyan for teaching me about the structural properties of AlN thin films and Professor Giovanni Fanchini, and Dr. Arash Akbari-Sharbaf for their support in ESR spectroscopy and EasySpin simulation.

I am especially grateful to all the other members of the Femtosecond laboratory. Vincent, thank you for our insightful discussions about various point defects and PL spectroscopy techniques. I appreciate Défi Junior Jubgang Fandio for our scientific conversations over the years. Your hard work and kindness have been a constant source of inspiration. Thank you, Bavneet, for being a great office mate and for our enjoyable conversations. Special thanks to Gabriel Laliberté and Paul-Ludovic Karseni for their availability to help me overcome technical difficulties in the lab, which significantly contributed to the results of this thesis.

I extend my gratitude to my family and friends, especially Marie-Lucie, Romain, Jonathan, Genevieve, and my parents Azar and Mohsen, my brother Shervin, and sister Ronak, for their unwavering support and for making my life outside work so joyful. I also appreciate my mother-in-law Fatemeh for her pure love and support, and I am grateful for all the emotional support from my father-in-law Mansour, who passed away tragically last year. Mansour, I miss you every day, and I will never forget you.

Lastly, Masoud, my husband, and best friend, I want to personally express my immense gratitude to you. I cannot put into words how much I owe you for your unwavering support and

unconditional love. Without you, none of this would have been possible. Even when everything seemed to be falling apart, your steadfast belief in me helped me to find the strength and confidence to persevere. I want you to know that I love you deeply.

Thank you, everyone!

List of Figures

List of Tables

Contents

INTRODUCTION

Over the past few decades, spin defects in wide-band materials have garnered significant attention for their use in quantum technology. In materials science, a spin defect refers to a type of defect in a crystal lattice that involves an unpaired electron with a spin. This unpaired electron creates a localized magnetic moment that can affect the properties of the material.

One particular single-spin center that has emerged as a prime candidate for a solid-state qubit is the charged nitrogen-vacancy (NV^-) defect in diamond. This defect is formed by a nitrogen substitutional impurity (N_C) located adjacent to a carbon vacancy (V_C) and has the unique ability to be initialized, manipulated, and read out at room temperature [6–8]. However, the challenges associated with the growth and control of diamond lattice have hindered the use of NV centers for scalable quantum technologies. Therefore, researchers have turned to other materials, such as $III-V$ crystals, to generate and engineer similar defects. Recent studies have shown that spin defects in silicon carbide (SiC) [1, 9–13] and hexagonal boron nitride (h-BN) [14–17] can also be manipulated as qubits at room temperature, indicating that these materials could potentially act as hosts for qubits. Nevertheless, it is still desirable to explore other centers in semiconductors that can be grown with high-quality crystal growth techniques and doping processing.

The focus of our research is to explore various point defects in AlN, which can serve as a source for qubits. AlN possesses the necessary characteristics to function as a host for qubit centers. Its large band gap of 6.12eV [18] effectively minimizes the coupling between defect levels in the band gap and bulk states, while its spin-orbit splitting of only 19meV [19] increases the lifetime of the qubit state. Moreover, AlN's high-quality films can be grown and doped through established techniques [20–23], which makes it a promising candidate for applications in quantum technologies.

The presence of nitrogen vacancies (V_N) in AlN, along with their interactions with donor defects, has recently garnered significant attention. This is due to their potential as qubits with spin character, which can be manipulated through spin engineering [24], as well as their use as room-temperature single-photon emitters [2, 4, 25]. Research has demonstrated that the formation of $(Zr_{Al}-V_N)^0$ and $(Ti_{Al}-V_N)^0$ is energetically favorable in AlN, and these defects possess spin-triplet ground states similar to NV centers in diamond [26, 27].

The formation of defect complexes can be achieved through post-growth ion implantation tech-

niques. This involves either bombarding a lightly (Zr, Ti)-doped AlN film to create the vacancy in the doped film or directly implanting Zr or Ti atoms into the AlN films. Following ion implantation, a post-implantation thermal annealing treatment is necessary to eliminate most of the implantation damage and facilitate the formation of complex defects. The first method requires optimizing deposition conditions to obtain a film with the appropriate doping level, which has yet to be achieved within our group, and commercially acquiring this type of film is still challenging. The second method, which we advocate for this study, regulates the Zr or Ti concentration through the implantation dose and depth distribution of these atoms, but results in greater damage and defects in the AlN film. Therefore, it is crucial to study the impact of thermal annealing conditions on the structural and optical properties of implanted AlN films.

The objective of this thesis is to investigate the effects of ion implantation and various annealing protocols on the formation of complex defects in AlN thin films. Additionally, it seeks to establish a stronger correlation between the structural properties of AlN films, such as strain, and their optical properties and spin character. The thesis culminates in the development of a protocol for creating and regulating point defects in AlN thin films, along with a comprehensive study of the optical and spin properties of these defects. These findings may prove valuable in future quantum applications.

This study focuses on investigating the properties of defects in AlN thin films using photoluminescence (PL) spectroscopy and electron spin resonance (ESR) spectroscopy. Three types of samples, namely Zr-implanted, H-implanted, and Ti-implanted AlN films, were investigated.

Chapter 1 provides an overview of quantum technologies and potential quantum platforms for quantum applications. The electronic band structure of semiconductors and properties of defects in semiconductor materials are also discussed.

Chapter 2 reviews the structural and optical properties of AlN and highlights recent studies on spin defect investigations and single-photon emitters in w-AlN.

Chapter 3 reviews the experimental methods used for creating defects in AlN films and characterizing the structural and optical properties of these treated films.

The main results of the study are presented in Chapters 4 to 6. Chapter 4 covers the effects of ion implantation and thermal annealing under different gaseous atmospheres on the structural and optical properties of the AlN films.

Chapter 5 focuses on the optical studies of $(Zr_{Al} - V_N)^0$ complex defects and their comparison with previous theoretical and experimental results.

Chapter 6 presents the results of investigating the spin character of defects in Ti-implanted and H-implanted AlN films using ESR spectroscopy. A comparison between the experimental results

and simulations from EasySpin software revealed the spin character of these defects

CHAPTER 1 Semiconductors as Quantum Platform

This chapter provides an overview of the potential role of semiconductors in the field of quantum technology. The purpose of this chapter is not to provide an exhaustive review, but rather to introduce the most relevant concepts for the present work. The chapter begins with a brief introduction to the three primary categories of quantum technology, namely quantum sensing, quantum computing, and quantum communication. The chapter then discusses potential platforms for these quantum technologies. Next, the electronic structure of semiconductors and the properties of their defects are examined. Finally, the importance of point defects in semiconductors for quantum applications is discussed.

1.1 Quantum Technology

The field of quantum technology (QT) utilizes quantum mechanics to achieve greater efficiency than classical technologies in various techniques and functionalities [28]. Quantum bits, or qubits, serve as the building blocks for QT and must be available in a superposition of two or more quantum states. QT has grown rapidly in recent years, finding applications in quantum sensing, quantum computing, and quantum communication, where the basic rules of quantum mechanics such as entanglement and superposition are crucial. As this thesis focuses on the formation and characterization of qubits, each of these technologies will be briefly explained, followed by a discussion of the various possible material platforms for local physical qubits in QT.

1.1.1 Quantum Sensing

Quantum systems are inherently unstable and easily affected by external factors, which makes them vulnerable to decoherence. These systems are commonly found on the nanoscale and can react to even the smallest and most localized changes in their environment. The field of quantum sensing aims to take advantage of this sensitivity by detecting variations in physical quantities like temperature and electromagnetic fields. This enables the development of more precise measurement tools for use in sensing, metrology, and imaging. What sets quantum sensors apart from their classical counterparts is that they are prepared in a specific quantum state, and can use isolated quantum objects, coherence of quantum superposition, or quantum entanglement to detect changes in physical quantities. The precision of a quantum sensor can ideally increase as the number of particles in the system, N, increases, which is known as the

Heisenberg limit. In comparison, the precision of a classical sensor can only approach the square root of N [29, 30].

To implement quantum sensors, a system with discrete energy levels is necessary. Additionally, the system should have the potential for controlled initialization and state read-out, as well as the ability to be coherently manipulated by time-dependent fields. Finally, the system must interact with the physical quantity to be measured through a coupling parameter. Up to this point, the primary applications of quantum sensing that have been widely adopted include atomic clocks, magnetic field sensing, and nanoscale imaging. However, as quantum technologies continue to advance, further advancements in quantum sensing are expected [30].

The concept of quantum sensing presents a fascinating dilemma, as it involves taking advantage of the inherent instability in the quantum nature of the sensor system. By doing so, we can obtain valuable and precise information about local fluctuations in the environment. However, it is important to note that a quantum system that strongly interacts with its environment will experience rapid decoherence. To achieve maximum sensitivity, it is crucial to select a sensor system that is tailored to the specific application. This means picking a sensor that couples strongly to the physical quantity being measured (such as a magnetic field) while retaining a long coherence time [30].

1.1.2 Quantum Computing

In the 1970s, the concept of merging quantum mechanics and information theory emerged. The idea gained popularity in 1982 when Richard Feynman pointed out that classical computing methods could not describe quantum phenomena [31]. The interest in quantum computing surged after mathematician Peter Shor created a quantum algorithm that could efficiently find prime factors of large numbers. While both quantum and classical computers aim to solve problems, they use different approaches. Classical computers use binary systems, whereas quantum computing uses qubits as basic units and leverages two principles of quantum mechanics: superposition and entanglement [32].

Superposition is the property of a quantum system to exist simultaneously in different states. For example, an electron can be in a superposition of states between a lower energy level and an upper energy level. A measurement would destroy this superposition, and the electron's state would collapse to either the lower or upper state. One way to understand the difference between binary position and superposition is to consider a coin. In a classical binary system, flipping a coin results in either heads or tails. However, in a superposition, the coin can exist in both states and all possible states in between. The concept of superposition underpins the

mechanism of qubits. In classical computing, bits are the basic units, representing the on and off states of a transistor, which correspond to 1 and 0 states. In qubits, the 0 and 1 states represent the lower and upper energy levels of an electron, respectively. Qubits can exist in a superposition of states with varying probabilities, and quantum operations can manipulate these probabilities during computations [33, 34]. Figure 1.1 illustrates the difference between classical bits and qubits.

Entanglement is a state where qubits are correlated, and obtaining information about one system immediately yields information about the other. By entangling more qubits in a system, quantum computers can compute exponentially more information and solve more complex problems [33].

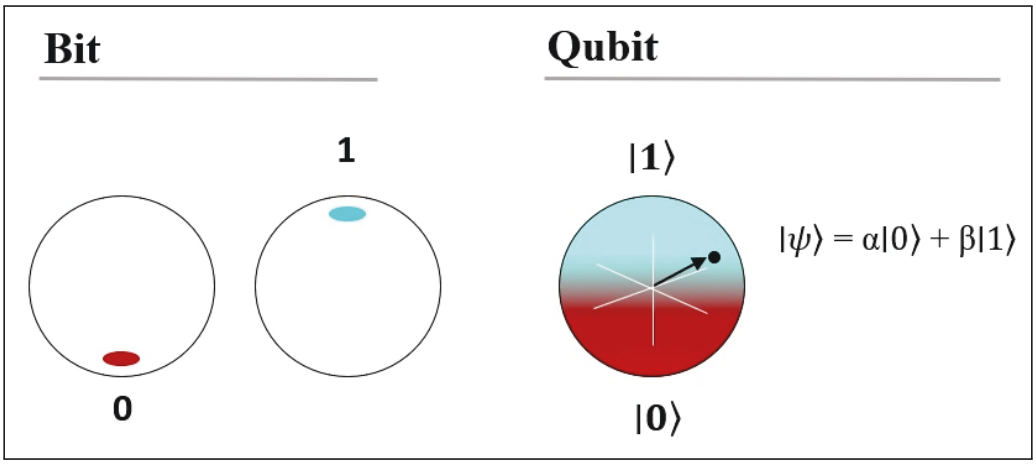

Figure 1.1 Bits are two separate states, 0 and 1, which are shown as two points. Qubits are a superposition of all possible states of 0 and 1, and are illustrated as a sphere (the Bloch sphere).

1.1.3 Quantum Communication

As quantum computers become more advanced, the security of transferring and storing information is at risk, posing a threat to our information-based society. Therefore, it is essential to develop protocols for the long-term secure management of data. Recently, quantum communication has emerged as a leading solution to this problem. Quantum communication involves generating and transferring quantum states over a distance, using protocols based on quantum random number generation (QRNG) and quantum key distribution (QKD).

QRNG (shown in Figure 1.2) uses a photon that enters a beam splitter and two detectors associated with bit values 0 and 1, where the randomness of the origin is clearly identified. QKD is a secure communication method that performs a cryptographic protocol based on the uncertainty principle [35].

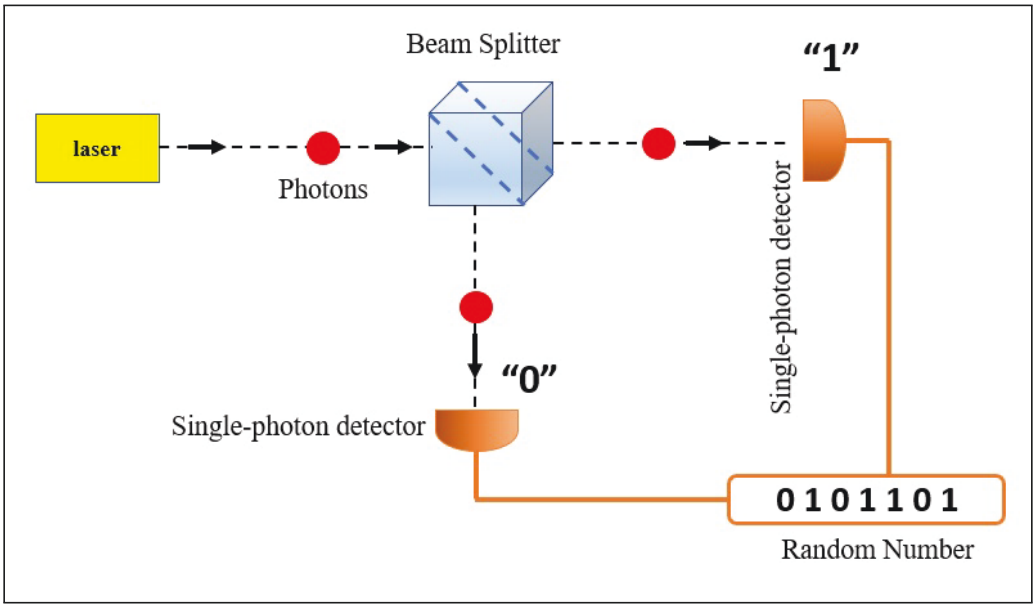

Figure 1.2 Schematics of a QRNG based on the single-photon splitting

The idea of quantum communication involves a sender (Alice) and a receiver (Bob) connected by a quantum communication channel that allows quantum states to be transmitted, typically using an optical fiber for photons. A third party may try to eavesdrop on the information exchanged, so the goal of QKD is to create a shared secure secret key between Alice and Bob. In the simplest version, Alice sends qubits in certain quantum states to Bob, who observes or measures them. If an eavesdropper tries to measure or change this qubit, it will leave a detectable trace due to the uncertainty principle. If the qubits have been changed, Alice and Bob both abandon the exchange and throw away the key. Otherwise, they can use the key to exchange perfectly secure communication. Alternatively, the eavesdropper might try to copy the flying photons and then send them to Bob. However, based on the no-cloning theorem, creating an independent and identical copy of an arbitrary unknown quantum state is impossible, which prevents eavesdropping on these flying qubits.

Quantum cryptography also exploits the unique correlations exhibited by entangled photons. For example, Alice and Bob could use one pair of entangled photons passing through an optical fiber, where Alice sends her message, and Bob can read this teleported message securely.

However, fiber-based QKD is limited by their transmission loss in optical fibers, which can function up to 100 km for commercial systems [29] and 833.8 km for academic prototypes [36]. In classical optics, the problem of transmission loss is solved by using a simple optical amplifier. However, conventional amplifiers are noisy and create many errors, so the photons carrying signals cannot be amplified with these systems to maintain quantum security. As a result, quantum

communication requires quantum hardware repeaters to preserve the quantum nature and entanglements of photons. These quantum repeaters could help break the transmission distance to a shorter distance where entanglement could be prepared and stored in a quantum memory [35].

1.1.4 Potential Quantum Platforms

A wide range of systems have been utilized as hosts for two-level qubit systems. These include single atoms confined in an optical lattice, electron spins, nuclear spins, trapped ions, superconducting circuits, quantum dots, and point defects in solids [28]. In the following sections, some of these promising material platforms will be discussed.l platforms are reviewed.

1.1.4.1 Single-Photons

Photons have shown great promise as a system for quantum technology since its emergence. These clean and decoherence-free quantum systems enable high-fidelity single-qubit operations to be easily performed [37]. Photonic qubits have various attractive characteristics such as minimal interaction with their surroundings, resulting in a system with low noise, inherent mobility, and the capability to transfer from one location to another without the need for low temperatures, in contrast to solid-state equivalents. However, photon-photon entanglement and multi-qubit control of these systems remain challenging. Despite the existing concept of photonic-based quantum computing, it requires high-efficiency single-photon sources and detectors, as well as optical quantum memories. Nonetheless, the quantum properties of light have already been utilized in QRNG and QKD, and play a crucial role in quantum communication. Thus, any advancement in the field of photonic-based quantum computing could have a significant impact on both quantum information processing and quantum networking.

1.1.4.2 Superconducting Josephson Junction

A Josephson junction is a quantum mechanical device composed of two superconductors that are weakly coupled by an insulating or non-superconducting region. The unique features of Josephson junctions stem from the underlying principles of superconductivity, a state of matter characterized by zero electrical resistance and the exclusion of magnetic fields. Below a critical temperature, pairs of electrons, known as Cooper pairs, bind together to enable zero-loss motion through the material [38]. Josephson junctions have emerged as promising candidates for qubits in quantum computers due to their long coherence times and the possibility of designing a large number of qubits using integrated-circuit processing techniques, which adds flexibility

to device functionality [33].

Although conventional linear circuit elements can form superconducting resonators, they cannot be used as qubits due to degeneracy in energy levels. However, Josephson junctions provide the nonlinearity necessary to turn a superconducting circuit element into a qubit, breaking the energy level degeneracy and limiting the system to two-qubit states. A schematic comparison between a conventional LC-circuit and an LC-circuit with a Josephson junction is shown in Figure 1.3.

Despite the progress made in superconducting quantum computing, several challenges and open questions remain. Current superconducting qubits have coherence times in the μs range, which must be increased. Additionally, higher-quality superconducting qubits must be developed and implemented by improving qubit connectivity and gate fidelity, both of which are key challenges for the development of superconducting quantum computing [39].

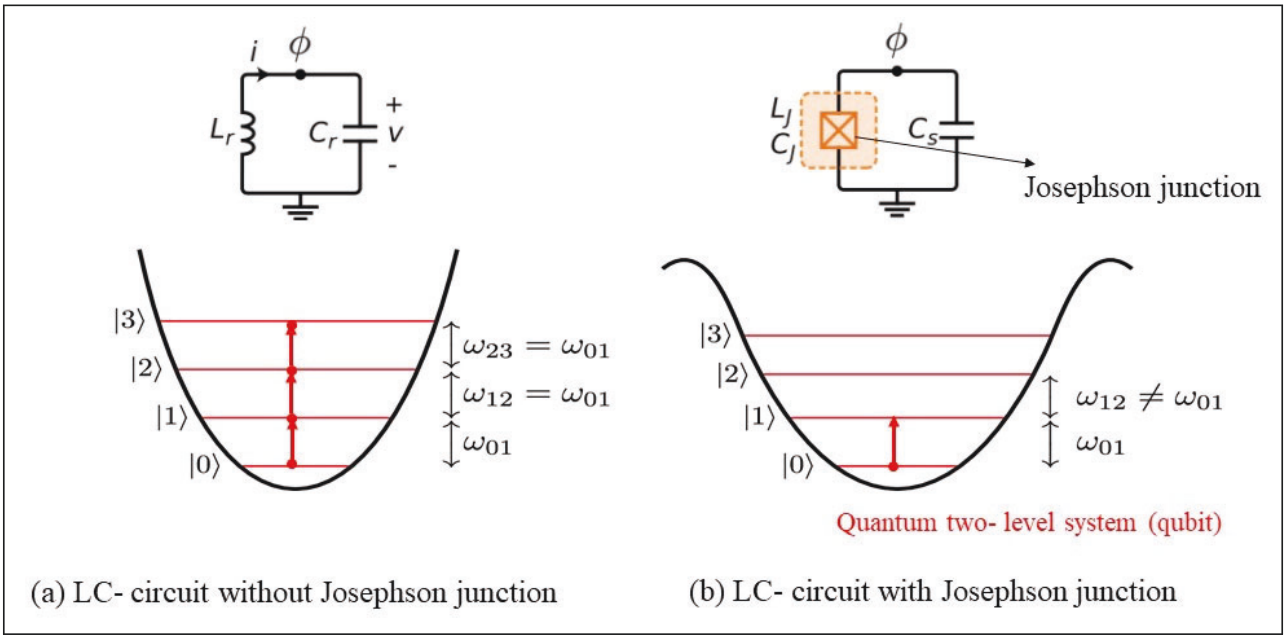

Figure 1.3 Schematics diagram for comparison of energy levels in a conventional LC-circuit (a) and a LC-circuit with a Josephson junction (b).

1.1.4.3 Trapped Atoms and Ions

Quantum computing utilizing trapped atoms or ions involves suspending a string of atoms or ions in free space using a combination of electromagnetic fields. The qubits in this system are stored in the energy levels of the trapped atom or ion, resulting in qubits with long T_1 and T_2 times [33]. These time constants are crucial for describing the coherence properties of a qubit

in a quantum computing system. T_1, also known as the "relaxation time," measures the time it takes for a qubit to lose its quantum information due to interactions with its environment. On the other hand, T_2, also known as the "dephasing time," measures the time it takes for a qubit's quantum state to lose its phase coherence. Achieving longer T_1 and T_2 times is ideal for quantum computing because it leads to more stable and accurate quantum computations. However, environmental noise and other sources of decoherence pose challenges to achieving long T_1 and T_2 times.

Trapped ions or atoms in a quantum computing system can be entangled by using lasers to induce coupling between their qubit states and external motion states. Optical pumping and state-dependent optical fluorescence detection can be used to initialize and measure these atomic qubits [33]. While trapped ions meet the necessary criteria for quantum computing [40], the implementation of such systems on a larger scale can be challenging due to the need for high-fidelity control and elimination of decoherence caused by interactions with the external environment.

1.1.4.4 Quantum Dots

Quantum dots (QDs) are artificial atoms that are placed within a semiconductor host. These structures act as a type of nanostructure within the semiconductor, capturing electrons or holes in energy levels that behave like trapped ions. Unlike other fabrication methods, they do not require cooling and trapping. However, the nuclear spin in the semiconductor host can lead to decoherence in QDs, which can be mitigated through isotope purification and dynamic decoupling of nuclear spin noise [33].

QDs can take many forms, including electrostatically defined QDs using metal grids or self-assembled nanoparticles. The main difference between these QDs is the depth of their potential. Electrostatically defined QDs are electrically controlled and operate at extremely low temperatures (mK), similar to superconducting qubits. Self-assembled QDs, on the other hand, operate at higher temperatures (4K) and offer an advantage over superconducting qubits [33].

Optical transitions in QDs are limited to discrete energies, making them a potential candidate for fast voltage control combined with optical initialization and read-out. However, for electrostatically defined QDs, the short-range exchange interaction makes large-scale entanglement difficult. Photonic connections could solve this problem, but reliable two-qubit gates remain a challenge. Self-assembled QDs, on the other hand, have strong coupling to photons, providing photonic connectivity. However, they form randomly, leading to a range of shapes and sizes that can result in varying optical absorption and emission energies. To ensure greater

optical homogeneity while retaining the beneficial properties of the artificial atom, the solution is to reduce the system size even further while embedding the qubit into a solid-state matrix. Bulk semiconductors and the point defects found within them offer a potential solution to this problem [33].

1.1.4.5 Point Defects in Semiconductors

Point defects are defects that occur naturally within a crystal lattice, such as vacancies, interstitials, or antisites, or impurity atoms that are incorporated into the lattice, as well as their complexes. These defects can be isolated from one another and, to some extent, from their environment within the semiconductor host. This results in long coherence times and optical homogeneity of the systems, allowing them to behave like trapped atoms without the need for complex isolation techniques. In Section 1.4, it will be explained in detail why point defects in semiconductors are suitable building blocks for quantum technology applications.

1.2 Electronic Band Structure of Semiconductors

Solid-state The electrical conductivity of materials is commonly classified into three categories: metals, semiconductors, and insulators. Semiconductors exhibit an intermediate electrical conductivity value between conductors and insulators. In an isolated atom, each orbital has a discrete energy level, and according to the Pauli exclusion principle for fermions, each energy level is occupied by two electrons with opposite spins (up and down).

When N atoms come together in a crystal lattice, the adjacent orbitals overlap in a solid, causing each energy level to split into N energy levels that are very close in energy. This can be thought of as an energy band. At $0K$, the highest energy of electrons is called the valence band (VB), while the conduction band (CB) is the lowest energy of the vacant bands. The VB and CB, located close to the Fermi level, are separated by a band gap, which represents a range of energy states that are forbidden for electrons. Figure 1.4 shows a schematic diagram of VB, CB, and the band gap as a function of interaction distance.

1.3 Defects in Semiconductors

Regardless of the growth method used, all semiconductors contain defects such as impurities, native defects, and extended defects. These defects have a significant impact on the fundamental properties of semiconductors and can be utilized for a wide range of applications. Recent advancements have shown that spin defects and colour centers are promising building blocks

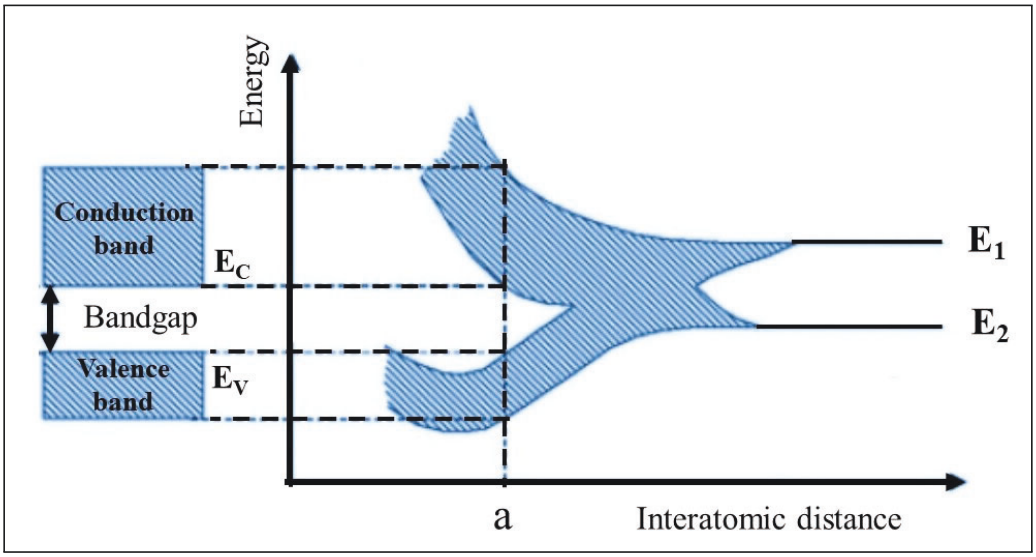

Figure 1.4 Schematic illustration of CB, VB, and band gap in semiconductors. With decreasing atomic distance, the nearby orbitals interact and sharp energy levels convert into bands.

for quantum technologies. This section will examine defects in semiconductors from both electrical and optical perspectives.

1.3.1 Electronic Properties of Defects

Incorporation and type of defects in semiconductors can alter their electrical properties. Hence, identifying and managing these defects is crucial for utilizing semiconductors in device applications. To classify the various types of defects in semiconductors, we divide them into two primary groups: shallow and deep centers.

1.3.1.1 Defects Classification

In the classification of defects in semiconductors based on their dimensionality, there are four categories: zero-, one-, two-, and three-dimensional defects. Point defects, including vacancies and interstitials, line defects such as dislocations, stacking faults, and grain boundaries, and precipitate voids, which are formed when impurities or foreign atoms precipitate in the crystal structure, all belong to these categories. [41]. Complexes, which consist of a small number of point defects bonding together, form another type of defect [42]. Point defects can be further classified into vacancies, interstitials, substitutional defects, antistes, and Frenkel defect pairs. A vacancy, denoted by V_A, is a missing atom (A) from a lattice site, while an interstitial, denoted by I_A, occurs when an atom (A) occupies an interstitial site. Substitutional defects occur when a different type of atom (C) replaces an original atom (A) in a lattice, and are denoted by

C_A. Antistes are substitutional defects in which one of the original atoms of the lattice (A) is replaced by another host atom (B), and are denoted by B_A. Frenkel defect pairs, named after their discoverer Yakov Frenkel, occur when an atom leaves its place in a crystal and becomes interstitial in a nearby location in the lattice. These defects can be considered complexes and are denoted by V_A-I_A [42]. Figure 1.5 shows a schematic illustration of different categories of point defects in semiconductors.

Point defects in a crystal lattice can have two origins: intrinsic and extrinsic. Intrinsic defects result from missing atoms (vacancies), displaced atoms (interstitials), or exchanged atoms (antisites) in the crystal, while extrinsic point defects form due to the presence of foreign atoms in the crystal structure. These foreign atoms can be substitutional or interstitial, with the former being called dopants. Dopant atoms exist in two types: donor and acceptor. A donor atom has one or more electrons in a high-energy orbital and can create an n-type semiconductor when added to a semiconductor. In contrast, an acceptor atom has one or more vacancies in a low-energy orbital, which can transform the semiconductor into a p-type one [43].

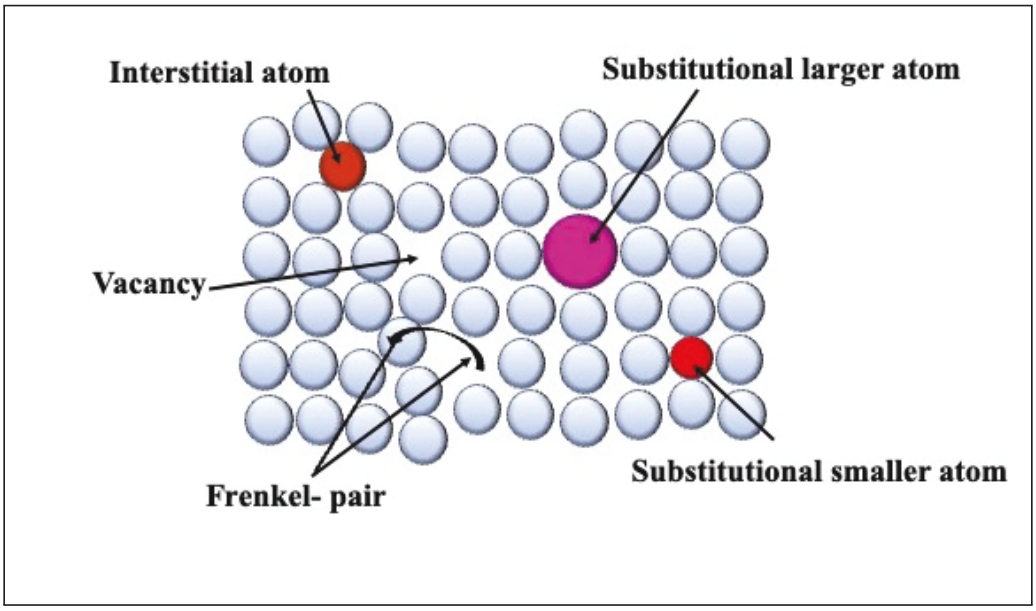

Figure 1.5 Illustration of different types of point defects in semiconductors.

1.3.2 Defect Levels

1.3.2.1 Shallow Levels

Shallow levels are energy levels induced by defects that exist within the bandgap of semiconductors, just below the CB or above the VB. These levels are typically located at an energy

difference of around k_BT from the band edges. Here, k_B represents the Boltzmann constant with a value of 1.38×10^{-23}[J/K], and T denotes room temperature which is 298°K. Shallow levels are generally responsible for controlled n-type or p-type conductivity in semiconductors. However, unintentional dopants can also create shallow levels that compensate for dopants and reduce doping efficiency. Unlike atoms, the ionization energy of donor- and acceptor-like impurities is only a few meV in most semiconductors, making them generally ionized at room temperature [44].

1.3.2.2 Deep Levels

Point defects in semiconductors can form deep levels when their energy levels are situated far away from the VB and CB edges in the bandgap. They are called deep levels because the energy required to transfer an electron or a hole from the defects band to the CB or VB is significantly higher than the thermal energy k_BT. These defects can result in uncontrollable radiative and non-radiative recombination channels, which may not be desirable for electronic and optoelectronic devices. However, they can be used constructively. For instance, deep spin defects in wide-bandgap semiconductors show promise for quantum technology applications. Two outstanding examples of these defects are nitrogen-vacancy (NV) centers in diamond and defects in SiC.

1.3.3 Optical Transitions in Semiconductors

1.3.3.1 Band-to-Band Transitions

In a state of thermal equilibrium, the concentration of intrinsic electrons and holes in a semiconductor is equal, denoted as ($pn = n_i^2$). If this balance is disturbed, processes will occur to restore it. In the case of carrier injection, the excess carriers can be recombined to restore equilibrium. In terms of the band diagram, an electron can gain energy and make a transition from VB to CB, leaving a hole in the VB. This is known as carrier generation, with the number of electron-hole pairs generated per cm^3 per second represented by the generation rate G_{th}. When an electron returns to the VB, an electron-hole pair is annihilated, which is called recombination and is represented by the recombination rate R_{th}. The net recombination rate is given by [45]

$$U \equiv R_{th} - G_{th} \tag{1.1}$$

Depending on the nature of the recombination process, it could be called radiative or non-radiative recombination. If the released energy from recombination is emitted in form of

photons, it is radiative recombination, otherwise, the energy is dissipated as heat to the lattice and the mechanism is called non-radiative recombination. Recombination processes also can be divided into two categories: direct and indirect recombination. The minimal-energy state in the CB and the maximal-energy state in the VB are each characterized by a certain crystal momentum (k-vector) in the Brillouin zone. If both electron and hole have the same k-vector, the material has a direct bandgap otherwise it has an indirect bandgap. Gallium nitride (GaN) and Si are examples of direct and indirect bandgap semiconductors, respectively.

Band-to-band recombination is another name for direct recombination and this process is generally dominant for direct band gap semiconductors. Under a low-injection regime and for an n-type semiconductor with a direct band gap in which holes are minority carriers, the net recombination rate can be written as follows:

$$U = \frac{p_n - p_{no}}{\tau_p} \tag{1.2}$$

where p_{n0} represents the hole densities in an n-type semiconductor at thermal equilibrium, and τ_p is the lifetime of the excess minority carriers. Photocarrier lifetime corresponds to the time of return to equilibrium after the pulsed optical excitation [45]. A similar equation for the calculation of recombination rate applies to electrons in p-type material, where electrons are minority carriers.

1.3.3.2 Free-to-Bound Transitions

Defects in semiconductors create localized energy states within the bandgap, which can act as intermediate levels between the VB and CB. At higher temperatures, recombination mainly occurs through direct band-to-band transitions. However, at lower temperatures, carriers can become trapped in defect/impurity states, leading to recombination between a carrier from the CB/VB and one bound to the defect/impurity level. This type of recombination is referred to as free band to bound state transitions. If the transition is radiative, the emitted photon can be used to determine the binding energy of the traps/impurities.

1.3.3.3 Donor–Acceptor Pair Transitions

It is common for semiconductors to contain both donor (D^+) and acceptor (A^-) impurities. Generally, these donors and acceptors compensate each other, however, after optical excitation or carrier injection at very low temperatures, electrons and holes can be trapped and form a neutral donor (D^0) and acceptor (A^0) centers. In order to return to the equilibrium condition

some of the electrons in (D^0) site and holes in (A^0) sites will recombine through a process which is known as donor-acceptor pair transition (or DAP transition). The DAP transition can be represented by

$$D^0 + A^0 \rightarrow \hbar\omega + D^+ + A^- \tag{1.3}$$

Where $\hbar\omega$ is the energy of emitted photon [42]. The emitted energy from DAP recombination depends on Coulomb interaction between the ionized donor and acceptor and can be given by [46]

$$\hbar\omega = E_g - (E_D + E_A) + \frac{e^2}{4\pi\epsilon_0 R_m} \tag{1.4}$$

where R_m is the electron-hole separation in a DAP pair, E_g is the band gap energy and E_D, and E_A are the donor and acceptor binding energies, respectively. The separation between donors and acceptors is not a continuous variable and depends on the crystal parameters. For instance, for an FCC lattice with randomly distributed D and A impurities, R_m is given by [47]

$$R_m = \left(\frac{1}{2}m\right)^{\frac{1}{2}} a_0 \tag{1.5}$$

where a_0 is the lattice constant and m is the shell number.

1.3.3.4 Free-Exciton Emission and Bound-Exciton Emission

In high-purity and high-quality semiconductors, the amount of energy required to create an electron-hole pair is equivalent to the value of the band gap, E_g. It is anticipated that the Coulomb interaction attracts the electron and hole to each other, resulting in the formation of excitons. As a result, these quasi-particles are no longer autonomous, and their internal energy is lower than the value of E_g. Excitons can be classified into three categories based on their localization and radius: Frenkel excitons, Charge transfer excitons, and Wannier excitons [48]. Frenkel excitons are small-radius excitons that arise in molecular crystals and are highly localized at particular atoms or molecules.

In comparison to Frenkel excitons, charge transfer excitons have a greater radius and are primarily found in ionic crystals. These excitons arise from the transfer of an anion to the nearest cation neighbor, resulting in the formation of a region with maximum electron charge density. Another type of exciton is the Wannier exciton, which is a large radius exciton where the electron-hole pair is separated by multiple unit cell lengths of the lattice. As the wavefunction of these quasi-particles is completely delocalized, they can move freely within the crystal and are referred to as free excitons. Wannier excitons are prevalent in conventional semiconductors, and their annihilation results in characteristic luminescence peaks [48].

Regardless of the semiconductor's growth process, intentional (doping) and residual impurities are typically present. These impurities create effective traps within the band gap, which can capture excitons. As the excitons become localized in these trap states, their kinetic energy decreases, resulting in the formation of bound excitons (BE). Typically, the luminescence efficiency of bound excitons is significantly greater than that of free excitons. Emission spectra of moderately doped or sometimes even nominally pure semiconductors are commonly dominated by bound exciton luminescence [48].

1.4 Point Defects in Semiconductors for Quantum Technology

Different platforms have been developed to design qubits, the building blocks of quantum computers. However, in order to qualify for quantum computing, qubits must meet five criteria outlined by [40]. In addition, two more criteria (explained below) are required for transferring quantum information.

To construct quantum computers, the qubits must be scalable and include universal quantum gates. The next three criteria pertain to the operation of quantum computers, including the ability to initialize the qubits, maintain long coherence time for calculations, and read out the final results [49].

In addition, secure transfer of quantum information (flying qubits) requires the ability to connect flying and stationary qubits [49]. Various systems such as trapped ions, superconducting circuits, and quantum dots have been proposed and developed to realize quantum technology, but they face several challenges that need to be addressed. Despite having a long coherence time, trapped ions and quantum dots struggle with entanglement. On the other hand, quantum dots (QDs) hold the potential for spin-based quantum computing with rapid initialization and control protocols that are much shorter than the coherence time. However, lithographically defined QDs only operate at the mK temperature scale, while self-assembled QDs emit light over a broader wavelength range [50].

Point defects found in semiconductors offer a promising option for qubits. For a point defect to be suitable as a qubit, it should have a deep energy level within the semiconductor's band gap. This results in highly localized defect orbitals that are isolated from the environment. Additionally, the low spin-orbit coupling of the material host would allow point defects to capture electrons in localized, high-spin states with long coherence times. The use of point defects has already been explored in various areas of quantum technology, including qubits for quantum computers, single-photon emitters (SPEs) for quantum communication, and nanoscale sensors for quantum magnetometers [6].

The use of point defects in semiconductors is a promising approach for creating qubits. An ideal qubit based on point defects should have a deep energy level in the semiconductor's band gap, which makes the defect orbitals highly localized, allowing for long coherence times by isolating the defect states from the environment. With low spin-orbit coupling, point defects can trap electrons in high-spin states, making them suitable for various applications, including quantum computers, single-photon emitters, and quantum magnetometers.

The negatively charged nitrogen-vacancy (NV^-) color centers in diamond are a promising system for quantum sensing and information applications among point defects in semiconductors. These defects have spin states that can be manipulated at room temperature on a nanosecond time scale, while still remaining coherent for milliseconds [51, 52]. They have been demonstrated to act like single-qubit gates [53], and the initialization [54] and readout [55] of their electronic spin states have been achieved. Moreover, entanglement between two NV center spins separated by 3 meters has been demonstrated [56]. However, growth and control difficulties of the diamond lattice and low zero-phonon line (ZPL) emission of NV centers pose challenges for using them in scalable quantum technologies. Thus, it raises the question of whether analogs to these defects can be formed in other semiconductor platforms, such as III-V crystals. It is important to note that the zero-phonon line (ZPL) emission is a spectral line observed in the luminescence spectra of certain materials, including diamond, in which there is no energy exchange with phonons or quantized lattice vibrations. ZPL emission occurs due to a transition between two energy states of a point defect that is not coupled to lattice vibrations, resulting in a very narrow and well-defined spectral line. This characteristic is particularly desirable for various applications, such as quantum computing and quantum sensing, where coherence and spectral purity play critical roles.

Density functional theory (DFT) calculations have recently shown that point defects in wurtzite Aluminum Nitride (w-AlN) have promising characteristics for quantum technology applications, potentially leading to new opportunities in the field [24, 26, 27]. Chapter.2 of this thesis will provide a detailed explanation of these results.

CHAPTER 2 Aluminium Nitride

AlN is not found naturally on Earth but has been synthesized since 1862 when Briegleb and Geuther grew it by heating aluminum under a nitrogen atmosphere, following the nitridation reaction of [57]:

$$Al(s) + \frac{1}{2}N_2 = AlN(s) \tag{2.1}$$

The first attempt at commercial production of AlN was carried out by Serpek in 1910 using the carbothermal reduction of alumina with coal and bauxite [58]:

$$Al_2O_3(s) + 3C(s) + N_2(g) = 2AlN(s) + 3CO(g) \tag{2.2}$$

In 1915, Fitcher and Oesterheld successfully grew AlN crystals in an electrical furnace [59]. Since then, various techniques have been used for the growth of AlN, leading to increased purity and a range of crystal structures.

There are four main methods for growing bulk AlN crystals:

- physical vapor deposition (PVD)
- hydride vapor phase epitaxy (HVPE)
- metalorganic chemical vapor deposition (MOCVD)
- growth from solutions

AlN has a III-V structure with three common phases: hexagonal wurtzite (w-AlN), zincblende (zb-AlN), and rocksalt (re-AlN). Under ambient temperature and pressure, wurtzite is the most stable phase, but under certain experimental conditions, metastable zb-AlN or high-pressure rs-AlN can exist [60–63].

In the wurtzite structure of AlN, each Al atom is surrounded by four equivalent N atoms, forming a tetrahedral structure with hexagonal $P6_3mc[186]$ space group [64]. Each Al atom has three half-occupied orbitals and one unoccupied orbital, while each N atom has three half-occupied and one fully occupied orbital. Each Al atom forms three short bonds and one long bond with N atoms located in the c-plane and along the c-axis of w-AlN, respectively [65]. The lengths of these short and long bonds are 1.885 Å and 1.917 Å, respectively [65]. The bond angle for the three short bonds is 110.5°, and that of the long bond is 107.7° [65]. The lattice constants of w-AlN are $a = 3.110$ Å and $c = 4.980$ Å [65]. Figure 2.1 shows a schematic illustration of w-AlN.

The AlN wurtzite structure consists of Al and N atoms arranged in a hexagonal close-packed

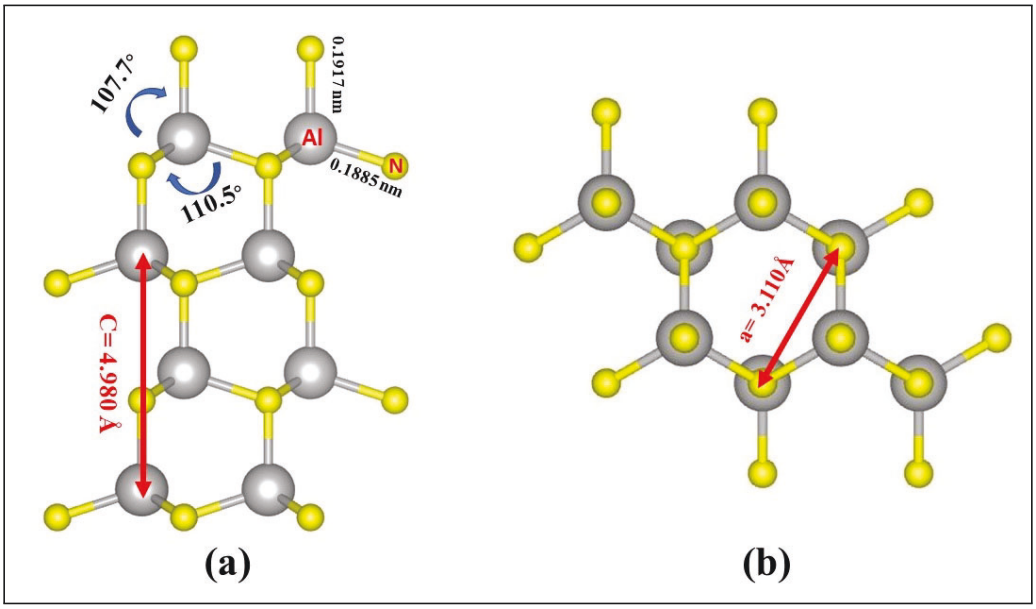

Figure 2.1 Illustration of wurtzite AlN structure showing the (a) a plane, and (b) c plane.

pattern with alternating layers of Al and N along the c-axis. AlN is a direct band gap semiconductor and has the widest direct band gap among III-V materials, measuring 6.12 eV [18]. Aside from its wide band gap, AlN exhibits high thermal conductivity (approximately 320 W/m K) [66], excellent optical properties [67] and dielectric characteristics, low dielectric constant, good mechanical strength [66], negative electron affinity [68–70], and high piezoelectric coefficient [71]. As a result, it has the potential to be employed in various applications.

2.1 Optical Properties and Impurities

Despite the expectation that pure AlN is transparent at excitation energies lower than its band gap (6.12 eV), high-quality AlN crystals exhibit emissions below the band gap, ranging from blue to red, indicating various energy levels below the bandgap. These emissions are typically attributed to transitions related to point defects in AlN, such as vacancies and substitutional atoms. Oxygen, carbon, and silicon are the most probable substitutional atoms in AlN, and vacancies and their complexes can form unintentionally during the growth process or intentionally via ion implantation. The incorporation of impurity atoms can be attributed to their involvement in the growth process, either as part of the source material (oxygen, silicon) or in the crucible or reactor parts (silicon, carbon, oxygen). The defects responsible for a wide range of energy levels within the AlN bandgap, including both shallow and deep levels, are typically associated with V_{Al} and oxygen-related defects.

According to both experimental and theoretical findings, defects in AlN crystals can result in optical emissions occurring below the band gap, with the emissions ranging from blue to red. Such emissions are believed to occur due to transitions from the states associated with point defects in AlN, including vacancies and substitutional atoms like oxygen, carbon, and silicon. These defects can form unintentionally during the growth process or intentionally through methods like ion implantation. The presence of impurity atoms in the growth process, such as oxygen and silicon, or in the reactor parts, like carbon and oxygen, can explain their incorporation.

Previous studies have shown that V_{Al} defects are responsible for optical emission ranging from 2.7 eV to 4.6 eV [72–75], while oxygen atoms substituting nitrogen atoms (O_N) result in energy levels within the band gap ranging from 3 eV to 4.2 eV [72, 73, 76–84]. The complex formation between O_N and V_{Al} leads to deeper energy states ranging from 2 eV to 4.7 eV [74–76, 85–96]. Other point defects such as V_{Al} [76, 97] ,carbon [95], and Si [85, 96] impurities also result in shallower energy states closer to the minimum of the CB in AlN. Additionally, recent studies have found that [27] transition-metal impurities like Ti, Zr, and Hf could form complexes with V_N, and they have potential applications as spin qubits in w-AlN. A summary of the optical studies of these point defects is provided in Table 2.1, while sections 3.3.1 and 3.3.2 will focus on the discussion of these complex defects in detail.

2.2 Applications

AlN, a wide-band gap semiconductor material, has attracted significant attention due to its impressive characteristics such as stable high-temperature performance, low energy loss, and good UV transmittance, making it an excellent material for high-frequency power applications [98]. With its wide direct band gap of 6.12 eV, AlN can be used to design Deep-UV LED devices that emit 210 nm deep-UV light, as demonstrated by previous studies [67, 99].

Furthermore, AlN's lattice constant is close to that of Si, sapphire, and SiC, making it a suitable substrate for epitaxial growth of III-V materials, thus solving the issue of large lattice mismatch and thermal mismatch common with other substrates [100, 101]. Due to its piezoelectric properties that are retained at high temperatures, high acoustic wave velocity, high Q factor, and low absorption coefficient, AlN is an ideal material for manufacturing surface acoustic wave (SAW) resonators and bulk acoustic wave (BAW) filters [102–105].

Moreover, AlN has excellent chemical stability, a small dielectric constant of 8.9, and a high breakdown field of over 800 kV/cm, making it an excellent material for micro-electromechanical systems (MEMS) applications [106, 107]. In recent investigations, AlN has also shown potential advantages in quantum technology applications, which will be

Type of impurity	Energy (eV)	Transitions	References
$V_{Al}^{3-/2-}$	4.6	CB $\rightarrow V_{Al}$	[72, 73]
	(3.37 ± 0.11)	Unknown Shallow level$\rightarrow V_{Al}^{3-/2-}$	[74, 75]
	2.7	V_{Al} $\rightarrow$VB	[72, 73]
V_N	4.2	$V_N \rightarrow$VB	[76, 97]
Oxygen related defects	3.3	$O - DX \rightarrow$VB	[76–78]
	3.1	O-DX $\rightarrow V_{Al}^{-3}$	[72, 73]
	(3.27 ± 0.3)	$O_N \rightarrow V_{Al} - O_N$	[77, 79–84]
Complex defects with Oxygen	2.03	$V_{Al} - O_N \rightarrow$VB	[74, 76, 85]
	2.53	$V_{Al} - 3O_N \rightarrow$VB	[86]
	2.6	SD $\rightarrow V_{Al} - 2O_N$	[80, 87–89]
	3.1-4.6	SD $\rightarrow V_{Al} - 3/4O_N$	[90]
	3.4	CB $\rightarrow V_{Al} - O_N$	[91]
	3.8	SD $\rightarrow V_{Al} - O_N$	[74, 75, 85]
	4.7	SD $\rightarrow V_{Al} - 2O_N$	[75]
Carbon	3.86	CB$\rightarrow C_N$	[92–94]
	4.3	CB$\rightarrow C_N - Si_{Al}$	[95]
Silicon	3.9	Si-DX $\rightarrow$VB	[85, 96]

Table 2.1 Color centers typically observed in AlN bulk and nanostructure crystals.

explored in sections 3.3.1 and 3.3.2 since the focus of this thesis is on the quantum applications of AlN.

2.2.1 Spin Defects in w-AlN

The application of optically active spin defects in wide band gap semiconductors in solid-state quantum technology has received significant attention. Among the atomic-like defects, the charged nitrogen-vacancy centers (NV^-) have gained recognition as a solid-state qubit due to their ability to be initialized, manipulated, and measured at room temperature. NV^- centers consist of a carbon vacancy (V_C) next to a substitutional nitrogen atom (N_C) [6]. However, the challenges associated with diamond crystal growth and control pose severe limitations to the use of NV^- centers as qubits, raising the question of whether similar defects can exist or be formed in other wide-band gap materials [24].

SiC is an alternative to diamond and has been found to possess point defects that can serve as

room-temperature qubits, which can be initialized, manipulated, and read out [12, 108, 109]. Experimental and theoretical investigations of Si vacancies (V_{Si}) in SiC have been carried out. While SiC's "NV-like" qubits may have several advantages, they also have some drawbacks, including low optical read-out fidelity [6] and small ground-state spin-transverse strain coupling of divacancies in SiC, which make it unsuitable for some hybrid quantum applications [110–112]. Therefore, identifying wide-band gap semiconductor materials, other than diamond, that can serve as suitable hosts for qubits remains a highly desirable goal.

Density functional theory (DFT)-based first-principles calculations have been employed to study w-AlN as a potential host for qubits. These calculations have suggested that quantum defects spin in w-AlN could provide new opportunities for the development of quantum technology [24, 26, 27].

AlN has been identified as a promising candidate to act as a host for qubits due to several of its unique features. Its large band gap of 6.12 eV allows for localized point defects and suppresses coupling between defect levels and bulk states. Additionally, AlN has a small spin-orbit coupling of 19 meV, which extends the qubit-state lifetime. Furthermore, AlN offers well-developed growth and doping techniques. As a piezoelectric material, it allows for measuring and controlling the vibrational motion of the lattice, which may offer a variety of control schemes for quantum spins. Despite these advantages, the non-zero nuclear spin of atoms in AlN can interact with localized spin qubits, resulting in decoherence of qubit states. However, appropriate pulsing and polarization techniques can control this spin-bath effect, allowing for the identification of single-spin centers in AlN.

Levels within the band gap of a semiconductor induced by point defects can generate controllable quantum states when appropriately occupied by electrons. Cation and anion vacancies among point defects can produce suitable atomic-like states. In AlN, the removal of a host atom leads to sp^3 dangling bonds (DBs), which interact and split the DB states into a symmetric a_1 state and three t_2 states. Depending on whether the vacancies are cation or anion vacancies, the t_2 states tend to be close to the valence band (VB) or conduction band (CB), respectively [1]. However, to avoid interference between the electronic states of the host and the optical transitions of qubits, the t_2 states must be engineered to move deeper into the band gap.

Figure 2.2 shows the position of the anion DB orbitals and the splitting between the a_1 and t_2 vacancy orbitals. To engineer these states, several approaches have been proposed, including applying strain, alloying the host material with a larger bandgap material, and introducing impurities adjacent to the vacancy [1, 27].

To form and manipulate centers related to cation vacancies in AlN, the Fermi level must lie

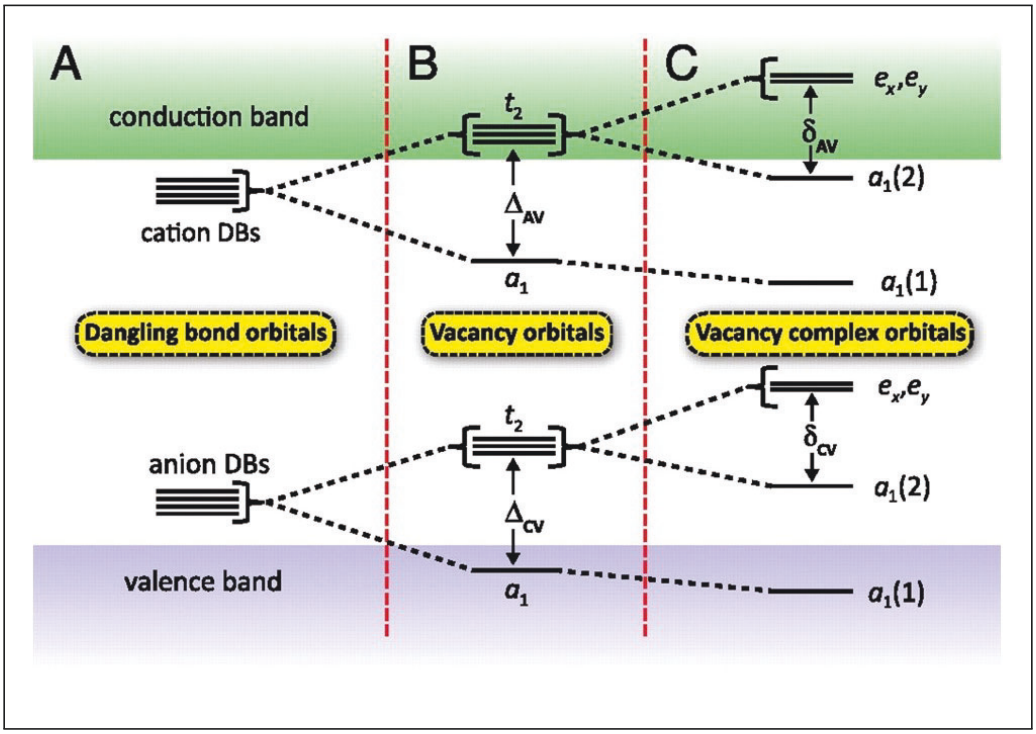

Figure 2.2 Defect level structure in a tetrahedrally coordinated compound semiconductors. sp^3 DBs (A) interact and split in a_1 and t_2 levels (B). Complexes between vacancies and adjacent impurities results in further splitting of t_2 levels. Figure is taken from [1].

below mid gap, indicating p-type AlN. However, achieving p-type doping in AlN is highly challenging [113], so current research on spin defects in AlN is limited to n-type w-AlN. Seo et al. [24] investigated the formation energy and spin of different charge states for the most likely defects in AlN. The first group of defects studied were those related to V_{Al}, including complexes between V_{Al} and O_N or V_N. The high formation energy of the V_{Al}—V_N divacancy makes it unlikely that these vacancies form spontaneously. Therefore, we exclude them and focus on $V_{Al} - O_N$ defects.

Although some theoretical studies have suggested that the $V_{Al} - O_N$ defects in AlN could be similar to the NV centers in diamond, Seo et al. argued that these defects are not suitable for most quantum applications [24, 114, 115]. According to their study, the spin state of V_{Al}-related defects in n-type AlN is zero, and spin states higher than $\frac{1}{2}$ exist only in p-type AlN samples, which are challenging to grow. Furthermore, the energy position of the dangling bonds left by the presence of an Al vacancy is very close to the VB, making these defects unsuitable for quantum applications.

Regarding the O_N defects, the oxygen atoms can either donate an electron to the host or trap an electron, leading to a filled DX state and consequently no effective spin in the ground state.

In this discussion, we will focus on the various charge states of V_N defects in AlN. According to results obtained from DFT calculations [24], V_N exhibits ground states of $S = \frac{1}{2}$ and $S = \frac{3}{2}$ for charge states of $q = 0$ and $q = -2$, respectively. The researchers also discovered a metastable state of V_N^- with a spin-triplet state (S=1), which can be localized by applying moderate uni- or bi-axial strain.

The investigation also looked into the hyperfine parameters of V_N^- defects, which are mainly determined by the interaction between the impurity's electron spin and the surrounding nuclear spins. Such measurements are critical in identifying point-like paramagnetic impurities in solids. The results revealed that hyperfine parameters are highly sensitive to both uni- and bi-axial strain, but they change more significantly as a function of bi-axial strain. This phenomenon is attributed to the transition in the local defect geometry of the S=1 state from C_{1h} to C_{3v} for biaxial strain larger than 2% [24]. Additionally, the researchers found that V_N^- has a number of spin-conserved excitation that could be used to optically address the spin, making them excellent candidates as qubits in w-AlN.

Another group of potential qubit candidates in w-AlN are the large metal ion-vacancy (LMI-vacancy) pairs. Seo et al. [26] investigated the effects of Hf and Zr impurity incorporation in w-AlN and suggested that they could form neutral Hf- and Zr-vacancy pairs, which are stable defects with a spin-triplet ground state of $^3A_2$ and an ^3E excited state. The researchers proposed that the optical zero-phonon lines (ZPLs) for these neutral pairs fall within the range of approximately 2.3 eV to 3 eV. Furthermore, Seo et al. showed that the spin-pressure coupling for the Hf vacancy in w-AlN is approximately twice as large as that of the NV center in diamond, which could be advantageous for nanoscale pressure sensors. The researchers suggested that these complex defects are promising candidates as qubits in w-AlN.

Varley et al. [27] conducted a separate study on the effects of transition-metal dopants in w-AlN. The researchers investigated a number of group-IV impurities and their complexes with V_N and found that most of these impurities have no significant effect on the position of t_2-derived defects, with the exception of transition metals such as Zr and Ti. The researchers calculated the formation energy of different defects in w-AlN and determined that the incorporation of transition-metal impurities on the N site is energetically unfavorable. As a result, after introducing Ti and Zr into the w-AlN crystal, they will be incorporated into Al sites and form Ti_{Al} and Zr_{Al}. Varley et al. proposed that neutral Ti- and Zr-vacancy pairs are stable under a wide range of conditions and exhibit a spin-triplet (S=1) state. Their results showed a spin-conserving excitation from $(Ti_{Al} - V_N)^0$ and $(Zr_{Al} - V_N)^0$ complexes with zero-phonon line emissions at 2.86 eV and 2.36 eV, respectively.

2.2.2 Single-Photon Emitters in w-AlN

The recent advancement in photonic technology has led to significant interest in non-classical light sources that produce streams of photons with controllable quantum correlations. Of particular interest in this field is the study of single-photon emitters (SPEs). An ideal on-demand SPE emits exactly one photon at a time into a given spatiotemporal mode, and all photons are identical, resulting in full interference when any two are sent through separate arms of a beam-splitter (a signature of indistinguishability) [116].

SPEs are crucial building blocks for scalable quantum information technology, including linear optical quantum computing and quantum secure communication [117, 118]. Despite the interesting features of NV^- centers in diamond for various quantum technology fields, their optical properties for SPEs are imperfect. The emission of the NV^- center is concentrated in the phonon-free line (ZPL) when the photon couples only to electronic states. However, if the transition involves the contribution of phonons, the resulting emission is contained in a sideband whose width depends on the number of phonons involved. The fraction of photons emitted in the ZPL is quantified by the Debye-Waller factor of the emitter, which is an important indicator of the ability of the luminescent defect to emit single photons [118]. The NV^- centers in diamond yield a Debye-Waller factor of only 3%, which is not ideal for SPEs [119]. Therefore, it is crucial to search for alternatives of luminescent defects.

Various wide-band gap materials, such as SiC, ZnO [120], GaN [121], and hBN [17], have been studied for point defect-related single-photon emitters (SPEs). Recently, attention has been given to AlN as a potential host material for defect-based SPEs, and some studies have investigated this material [2–4]. In particular, Xue et al. [2, 3] examined SPEs in 2 μm thick AlN films that were grown epitaxially by metal organic chemical vapor deposition (MOCVD) on nanopatterned sapphire substrates (NPSS). Using micro-PL measurement, they observed randomly distributed SPE spots on the AlN films in the spectral range from visible to near-infrared (550-1100 nm). Although the origin of emissions at 713 nm and 867 nm were assigned to antisite nitrogen vacancy complex ($N_{Al}V_N$) and ($V_{Al}V_N$) divacancy using DFT calculation, the exact nature of these SPEs remains unclear.

The researchers observed strong zero-phonon lines (ZPLs) with weak phonon sidebands in AlN defects, suggesting a high Debye-Waller factor for these SPEs (see Figure 2.3). At low temperatures, Debye-Waller factors ranging from 10% to 25% were measured, which is significantly higher than the 3% value observed for NV centers in diamond.

To verify that the ZPL is indeed a single-photon emitter, second-order autocorrelation function measurements (denoted as $g^{(2)}(\tau)$) were conducted. As shown in Figure 2.3, the $g^{(2)}(\tau)$ values

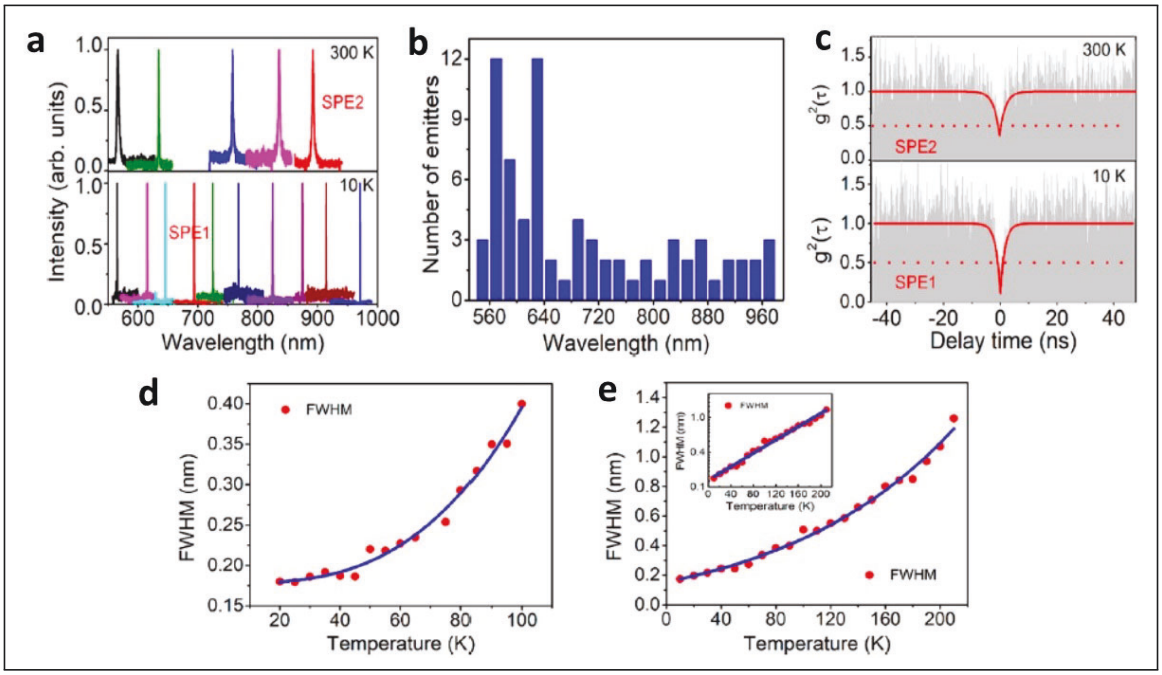

Figure 2.3 (a) PL spectra of AlN film at 300K and 10K. Two of the SPEs are denoted with SPE1 and SPE2 for further investigations with $g^{(2)}(\tau)$ measurements. (b) Histogram of the wavelength distribution of 74 emitters with a bin width of 20 nm. (c) $g^{(2)}(\tau)$ measurements of SPE1 and SPE2. (d) and (e) Temperature dependence of FWHM for two different emitters (solid red circles). Data have been fitted using a T^3 and an exponential functions for (d) and (e) respectively. Figure was taken from [2, 3]

for various bright spots were found to be below the classical threshold of 0.5, indicating the single-photon nature of the defect emissions.

Subsequently, the researchers investigated the optical performance of a single-photon emitter using excitation-power-dependent PL intensity measurements. The results showed that the optical emission intensity (I_∞) and the saturation excitation power (P_{sat}) were 4.6×10^5 counts/s and 2.23 mW, respectively. These findings indicate that the emission rate of the defect-related single-photon emitter is lower than that of epitaxially grown quantum dots [122].

Xue et al. conducted a study on the temperature dependence of the full width at half maximum (FWHM) of the zero-phonon line (ZPL) for different single-photon emitters (SPEs) in AlN. They observed that a greater number of emitters exhibit an exponential behavior rather than a T^3 dependence. They proposed two different dephasing mechanisms for these SPEs. The T^3 dependence was attributed to field fluctuations caused by phonon-induced dislocations of the crystal defects, similar to what has been observed for the silicon-vacancy (SiV) in diamond. On the other hand, the exponential dependence of the FWHM may be related to piezoelectric coupling to in-plane phonons, similar to what has been observed for SPEs in hBN. These findings

suggest the presence of multiple species of SPEs in AlN

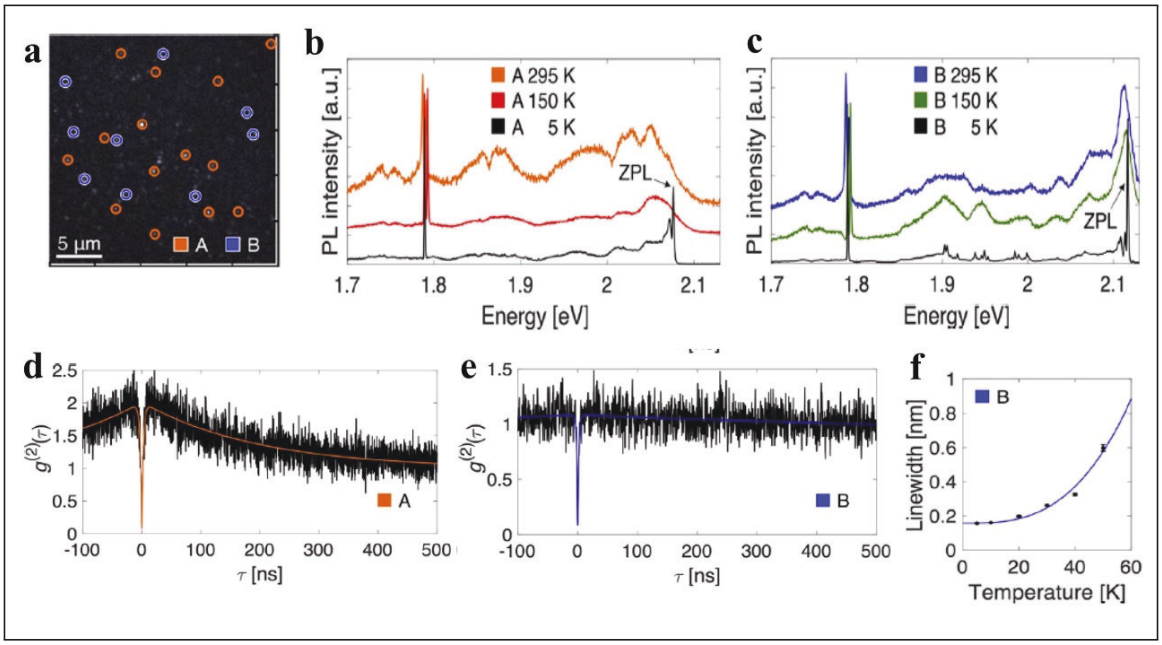

Figure 2.4 Spectral analysis of SPEs in AlN. (a) Quantum emitter density in a 25 $\mu m \times 25\ \mu m$ area. (b) and (c) Temperature-dependent PL spectra of type A and type B emitters respectively. (d) and (e) Continuous wave excitation second-order autocorrelation histogram with $g^2(0) = 0.08 \pm 0.06$ for type A emitter,and $g^2(0) = 0.09 \pm 0.08$ for the type B emitter. (f) Temperature dependence of the type B quantum emitter's ZPL line width. Figure was taken from [4].

Lu et al. [4] investigated the SPEs in 200 nm-thick AlN films grown by plasma vapor deposition of nanocolumns (PVDNC) on a sapphire substrate. They created vacancy-based SPEs by performing He implantation followed by thermal annealing under an Ar atmosphere. Two types of emitters, A and B, were observed. Second-order autocorrelation function $g^{(2)}(\tau)$ measurements confirmed that both types of emitters were predominantly SPEs ($g^2(0) < 0.5$), with $g^2(0) = 0.08 \pm 0.06$ and $g^2(0) = 0.09 \pm 0.08$ for type A and type B emitters, respectively. The temperature dependence of the type B quantum emitter's ZPL line width exhibited a T^3 behavior. A summary of their results is shown in Figure 2.4.

CHAPTER 3 Methods for Generating and Characterizing Point Defects

In this chapter, we will review the primary experimental methods used to investigate point defects in this study. The initial section will focus on defect formation using ion implantation and bombardment, followed by a discussion of techniques for structural and optical characterization. We will conclude with a brief overview of electron spin resonance spectroscopy (ESR).

3.1 Ion Implantation

The technique of ion implantation is commonly used to intentionally introduce foreign elements into a material for the purpose of doping or disrupting the crystal lattice. In this study, ion implantation was utilized to create point defects in an AlN film. While some defects, such as vacancies, naturally occur in materials to a certain extent, controlled fabrication is often required for systematic defect identification studies. In some cases, the generation of more complex defects may require the introduction of foreign elements such as Zr and Ti into the AlN lattice. The ion implantation experiments carried out in this study were designed to produce predominantly point defects rather than extended lattice damage. The impact of the implanted species on the resulting point defects is also discussed.

3.1.1 Physical Principle

Ion implantation is a process that involves accelerating ions of an element and introducing them into a target material, thereby altering its physical and chemical properties. The ions are first ionized and then accelerated using an electric field towards the target material. The position of the implanted ions, including their depth and distribution, is regulated by the acceleration energy (voltage), the mass of the implanted species, and the angle of the ion beam with respect to the surface normal. The amount of ions incorporated into the target material is regulated by the implantation fluence or dose, which represents the time for which the sample is exposed to the ion beam. The dose is carefully controlled by integrating the measured ion current. The total charge implanted during an ion implantation process can be calculated according to [123] using the formula:

$$Q_T = \frac{1}{q(\text{Area})} \int I dt \tag{3.1}$$

where Q_T is the total implanted charge, q is the elementary charge, Area is the irradiated area, I is the ion current density, and t is the implantation time.

Incident ions towards the target are scattered at random angles and slow down and eventually stop via two different mechanisms. They can be deflected by the positive nuclei of the atoms (nuclear collision) or collide with the sea of electrons of the target lattice atoms. The stopping power (S) is calculated by [123]:

$$S = \left(\frac{dE}{dx}\right)_{\text{nuclear}} + \left(\frac{dE}{dx}\right)_{\text{electronics}} = S_n + S_e \tag{3.2}$$

The dominance of nuclear scattering occurs for lighter elements and lower acceleration voltages, while electronic scattering is more important for heavier elements and higher ion energies. As the implanted ions experience a series of collisions, they start losing kinetic energy and eventually come to a stop. The collisions occur randomly, and the implanted ion distribution takes a nearly Gaussian form around some mean projected range, which depends on the ion mass and energy. It should be noted that the discussion on random collision events assumes that the implanted ion follows a random trajectory through the lattice. However, in crystalline materials, this is no longer true if the ion follows the open pathways between lattice sites through a process known as channeling. To prevent channeling, the impinging ion beam is made to hit the surface at an angle that is not parallel to the surface normal [123].

Ion implantation has several advantages, including precise control of impurity depth and dose, the possibility of having a complex profile by multi-energy implants, low sensitivity to the surface cleaning procedure, a low-temperature process which facilitates using the photoresists as a mask, and excellent lateral uniformity (less than 1% variation across 12-inch wafer). Despite the mentioned advantages of this method, ion implantation does have a few downsides. It is an expensive process and often requires extremely toxic gas sources. Not all the damage caused by ion implantation can be corrected by post-implant annealing, and it is difficult to create very deep or very shallow profiles using this method.

In this thesis, ion implantation was utilized to introduce heavy elements into an AlN film. In order to accurately predict the ion distribution and related damages when using ion implantation to create defects in semiconductor materials, Monte Carlo simulations were employed using the Stopping and Range of Ions in Matter (SRIM 2013) [124] code. Figure 3.1 displays an example of the results obtained from the SRIM simulation for Ti atoms. It is important to note that the results obtained from the SRIM simulation do not reflect the defect concentration and distribution following thermal annealing, as they only provide information about the initial damage events. During thermal annealing, the percentage of surviving vacancies is typically

between $2-5\%$ in most semiconductors. Additionally, during this high-temperature step, the implanted impurities will diffuse and broaden the implantation profile, resulting in some of the implanted ions migrating towards the vicinity of vacancies and creating complex defects with them. The formation of these complex defects is central to the study.

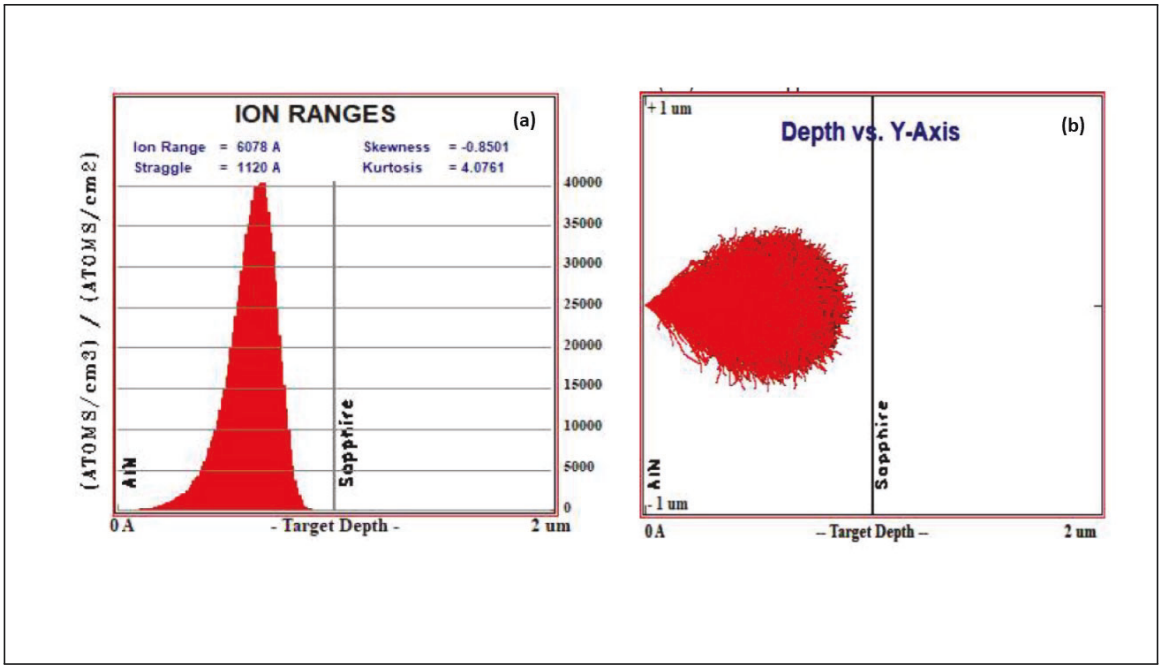

Figure 3.1 SRIM/TRIM simulation for 1 MeV Ti ion implantation in AlN film (a) Ion-depth distribution (b) estimated ion trajectories.

.

3.1.2 Experimental Conditions

In this experiment, ion implantations were performed to introduce a Gaussian-like distribution of point defects within the AlN film, with the peak located several nanometers from the sample surface. According to DFT calculations [24, 26, 27], nitrogen-vacancies and their complexes with group-IV impurities can create defects with spin-triplet states. Spin-triplet states are of great interest for quantum applications because they exhibit longer coherence times compared to spin-singlet states, making them more resistant to decoherence. In spin-triplet states, the spins of two electrons are parallel, leading to a larger magnetic moment and a stronger interaction with the environment. This stronger interaction makes it more difficult for the spin-triplet state to decoherence, which is essential for quantum computing and other quantum technologies. Furthermore, spin-triplet states can be utilized to perform two-qubit operations, which are necessary for scaling up quantum systems to perform larger and more complex computations.

To induce defects in the AlN films, we employed implantation techniques with H, Ti, Zr, and Hf atoms. The goal was to create V_N and defect complexes within the AlN material. In order to ensure a consistent defect concentration profile, we utilized different implantation energies and fluences for each sample. To prevent channeling, all implantations were carried out at an angle of 7° off the surface normal. We used two types of samples for the implantation process. The first type was a 1 μm AlN thin film, which was deposited on a (100) oriented silicon (Si) substrate using a reactive DC magnetron sputtering (MS) technique by Teledyne DALSA Manufacturing company. These samples were implanted with H, Zr, Ti, and Hf atoms. The second type of samples were 1 μm thick AlN epitaxial films grown by metal organic chemical vapor deposition (MOCVD) on a sapphire substrate by Dowa Electronics Materials Co. These samples were implanted with Ti and H atoms.

We chose these parameters to achieve a uniform distribution of vacancies throughout the AlN film. Additionally, in the case of heavy elements, our objective was to ensure that these elements remained within the AlN layer. We performed ion irradiation using Hydrogen, Ti, Zr, and Hf ions, with specific parameters as follows:

- For hydrogen irradiation, we employed 250 MeV at a fluence of 5×10^{15} $ions/cm^2$ and studied them in Chapter.6.

- Zr ions were used at different kinetic energies (250 keV, 1 MeV, 1.75 MeV, and 2.5 MeV) with a fixed fluence of 1×10^{14} $ions/cm^2$. These samples were investigated in Chapter.4 and 5.

- We conducted ion implantation using Ti ions with implant energies of 100 keV, 500 keV, 1 MeV, and 1.5 MeV and fluences of 2×10^{11} $ions/cm^2$, 4×10^{11} $ions/cm^2$, 6×10^{11} $ions/cm^2$, and 1.6×10^{12} $ions/cm^2$, respectively. The structural properties and spin character of defects in these samples were investigated in Chapter.6.

- Hf ions were used at different kinetic energies (1 MeV, 2.5 MeV, 4 MeV, and 5.5 MeV) with a fixed fluence of 1×10^{13} $ions/cm^2$. However, these samples did not show any feature related to the creation of new point defects in AlN.

In all cases, the irradiation was performed at room temperature (RT). To partially repair the structural damage caused by ion bombardment, we annealed the implanted samples in a quartz tube furnace. Post-implantation annealing was performed under different gaseous atmospheres including argon, nitrogen, and forming gas (FG, 95% nitrogen + 5% hydrogen) at 1050 °C for 1 hour. Since AlN films can be easily oxidized when exposed to air at high temperature, we

allowed the samples to cool down to room temperature at a rate of 5 $°C/min$ in the furnace, maintaining the same annealing gaseous atmosphere.

The effects of different annealing atmospheres were investigated in Chapter.4. We used an ion implantation system for this study, and an image of the system and a schematic figure of the implantation process are shown in Figure 3.2.

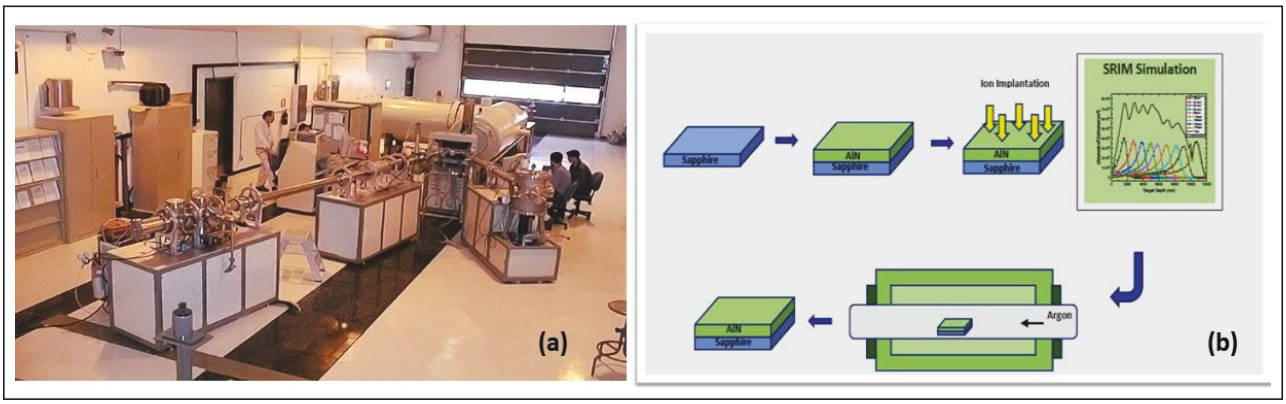

Figure 3.2 (a) Ion implantation system in Professor. Francois Schiettekatte's lab at the Department of Physics of Université de Montréal, (b) schematic image of preparation procedure of samples

.

3.2 Structural Characterization Method

In this study, the effects of ion implantation and subsequent annealing treatments on the structure of AlN films and the level of strain in these films were monitored using structural characterization techniques. To fully understand the structural properties of the samples, a combination of techniques was employed, which will be elaborated on in this section.

3.2.1 X-ray Diffraction

X-ray diffraction (XRD) is a powerful tool for analyzing the crystal structure of materials. It works by shining a beam of X-rays onto a sample and measuring the angles at which the X-rays are diffracted by the crystal lattice. The resulting diffraction pattern provides information about the crystal structure, such as the orientation, grain size, and defects within the material.

When ion implantation is used to modify the properties of a thin film, it can introduce lattice distortions and defects, which in turn affect the crystal structure of the material. These

changes can be detected by XRD, which makes it a valuable tool for analyzing the effects of ion implantation on thin films.

One of the most common changes that ion implantation can cause is lattice distortion. This occurs when the implanted ions create stresses within the crystal lattice, causing it to deform. The deformation can change the orientation of the crystal planes within the lattice, which in turn changes the positions of the diffraction peaks in the XRD pattern.

Another effect of ion implantation on thin films is the creation of defects, such as vacancies or interstitials, which can change the crystal structure. For example, defects can cause the crystal lattice to expand or contract, which can change the diffraction pattern. Defects can also cause the crystal planes to shift or tilt, which can affect the intensity and shape of the diffraction peaks.

In addition to changes in the diffraction pattern, ion implantation can also affect other properties of thin films, such as the surface morphology, electrical conductivity, and optical properties. By combining XRD with other analytical techniques, such as scanning electron microscopy (SEM) and Raman spectroscopy, it is possible to obtain a more complete picture of the effects of ion implantation on thin films.

3.2.1.1 Fundamental Principles

X-ray diffraction (XRD) is a non-destructive technique that provides valuable information about the crystal structure and properties of materials. In thin films, XRD can be used to study the orientation, thickness, and interfaces between the film and substrate. Two common XRD techniques used in thin film analysis are $\theta - 2\theta$ and the rocking curve.

Bragg's Law is the fundamental principle behind XRD. It states that when a beam of X-rays is incident on a crystal at an angle θ, the X-rays will be diffracted at an angle 2θ if the path difference between the diffracted rays is equal to an integer multiple of the X-ray wavelength. Mathematically, this can be expressed as:

$$n\lambda = 2dsin\theta \tag{3.3}$$

Where n is an integer, λ is the X-ray wavelength, d is the distance between adjacent planes of atoms in the crystal lattice, and θ is the angle of incidence. Figure 3.3 provides a schematic illustration of Bragg's law.

$\theta - 2\theta$ XRD is a widely used technique for characterizing thin films. In this method, the X-ray beam is incident on the sample at a fixed angle θ and the diffracted X-rays are detected at an

angle 2θ. The diffraction peaks are then analyzed to determine the crystal structure, orientation, and other properties of the thin film. The position, intensity, and width of the diffraction peaks provide information about the lattice spacing, crystallinity, and defects present in the film.

Ion implantation can affect the XRD peaks by altering the crystal structure and causing lattice distortions. This can lead to changes in the peak position, intensity, and width. For example, in a study of ion-implanted titanium thin films, researchers found that the peak position shifted to higher angles and the peak width increased with increasing ion fluence, indicating the formation of a distorted lattice structure [125].

Rocking curve XRD is another technique used to study the crystal structure and properties of thin films. In this method, the sample is rotated about a specific axis, and the intensity of the diffracted X-rays is measured as a function of the angle of rotation. The width of the rocking curve provides information about the thickness and crystalline quality of the film. A narrow rocking curve indicates a thin film with good crystalline quality, while a broad rocking curve suggests a thicker film with more defects.

XRD can be used to calculate the thickness of thin films by measuring the intensity of the diffraction peaks and comparing it to a reference sample of known thickness. By using a calibration curve, one can determine the thickness of the thin film based on the intensity of the XRD peak. For example, in a study of aluminum thin films deposited by ion beam sputtering, researchers used XRD to determine the thickness of the films based on the intensity of the (111) diffraction peak [126].

XRD can also be used to study the interfaces between the thin film and substrate. By analyzing the diffraction patterns at various angles, researchers can determine the degree of lattice matching between the film and substrate, as well as any interfacial reactions or defects. This information is critical for understanding the mechanical, electrical, and optical properties of thin film devices. For example, in a study of sputter-deposited copper thin films on silicon substrates, researchers used XRD to study the orientation and interfacial structure of the films [127].

3.2.1.2 Experimental Setup

X-ray diffractometers comprise three essential components: an X-ray tube, a sample holder, and an X-ray detector. X-rays are produced in a cathode ray tube by heating a filament to release electrons, accelerating these electrons towards a target by applying a voltage, and then bombarding the target material with electrons. When the energy of these electrons is high enough to displace the inner shell electrons of the target material, characteristic X-ray spectra are pro-

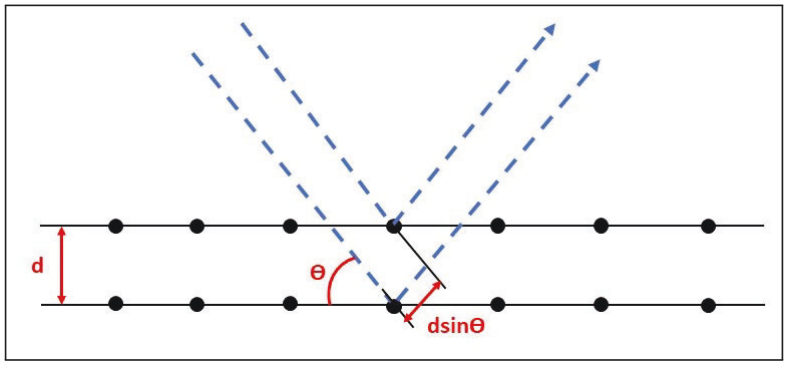

Figure 3.3 Bragg's law: The incident beam is scattered by atoms in two successive crystal planes. The lower beam traverses an extra length of $2dsin\theta$. Constructive interference occurs when this length is equal to an integer multiple of the wavelength of the radiation.

duced, including K_α and K_β components. K_α is composed of $K_{\alpha1}$ and $K_{\alpha2}$, with $K_{\alpha1}$ having a slightly shorter wavelength and twice the intensity of $K_{\alpha2}$. The wavelengths are specific to the target material (Cu, Fe, Mo, Cr), and filtering through foils or crystal monochromators is necessary to generate monochromatic X-rays for diffraction. The two K_α wavelengths are sufficiently close that their weighted average is used. Copper is commonly used as the target material for single-crystal diffraction, with Cu K_α radiation at 1.5418 Å. These X-rays are collimated and directed onto the sample, and as the sample and detector rotate, the intensity of the reflected X-rays is recorded. Constructive interference occurs and an intensity peak is produced when the incident X-ray geometry meets the Bragg Equation requirements. A detector records and processes this X-ray signal, converting it into a count rate output that can be displayed on a device like a printer or computer monitor. The AlN film's crystalline structure was examined using a Bruker (D8 Discover Model) X-ray diffractometer with high-intensity Cu K_α radiation ($\lambda = 1.5418$ Å) via $\theta - 2\theta$ scans and Rocking curve measurements.

In Chapters 4 and 6, we elaborate on the findings obtained from using X-ray diffraction (XRD) to investigate the structure and level of strain in AlN films.

3.2.2 Raman Spectroscopy

Raman spectroscopy is commonly used to study the strain induced in a material after ion implantation. The ion implantation process can introduce mechanical stress and strain in the target material, leading to changes in its Raman spectra.

Raman spectroscopy can be used to measure the frequency shifts and line broadening of the Raman modes, which are sensitive to the strain in the material. The shifts in the Raman spectra can be analyzed to determine the magnitude and distribution of the strain in the material

induced by the ion implantation process. By analyzing the strain induced by ion implantation, Raman spectroscopy can help optimize the process parameters to achieve desired strain levels for specific applications. This information can also be used to understand the mechanical behavior of the material and to design new materials with desired mechanical properties.

In this study, we utilized Raman spectroscopy in addition to X-ray diffraction (XRD) to investigate the alterations in both the strain levels and structure of AlN films subsequent to ion implantation and thermal annealing.

3.2.2.1 Fundamental Principles

Raman spectroscopy is a non-destructive and powerful technique for characterizing the chemical and structural properties of a sample. It was named after the Indian physicist C.V. Raman, who observed Raman scattering in collaboration with K.S. Krishnan in 1928 [128]. Similar to other spectroscopy methods, Raman spectroscopy involves the interaction of light with matter. When light is scattered coherently by a molecule, it results in an instantaneous process where the molecule passes to a virtual state. In most cases, the energy of the molecule remains unchanged, and the energy and wavelength of the scattered photon are the same as the incident photon. This is called elastic scattering or Rayleigh scattering and is the dominant process. However, in rare events, Raman scattering occurs through an inelastic scattering process, where energy transfer takes place between the molecule and the scattered photon. If the molecule undergoes a transition to a higher vibrational state than its original state, the scattered photon loses energy, and its wavelength increases. This is known as Stokes Raman scattering. Conversely, if the molecule relaxes to a lower vibrational level, the scatter photon gains energy, and its wavelength decreases, known as Anti-Stokes Raman scattering. Since the majority of molecules are in the ground vibrational level (Boltzmann distribution), Stokes scatter is the more statistically probable process. The energy diagram in Figure 3.4 illustrates these three types of scattering.

The wavelength of the Raman scattered light depends on the excitation light wavelength. Therefore, the position of a Raman peak is typically given in cm^{-1}, corresponding to the frequency shift relative to the excitation frequency:

$$\Delta\nu(cm^{-1}) = \left(\frac{1}{\lambda_0(nm)} - \frac{1}{\lambda_1(nm)}\right) \times \frac{10^7 nm}{(cm)} \tag{3.4}$$

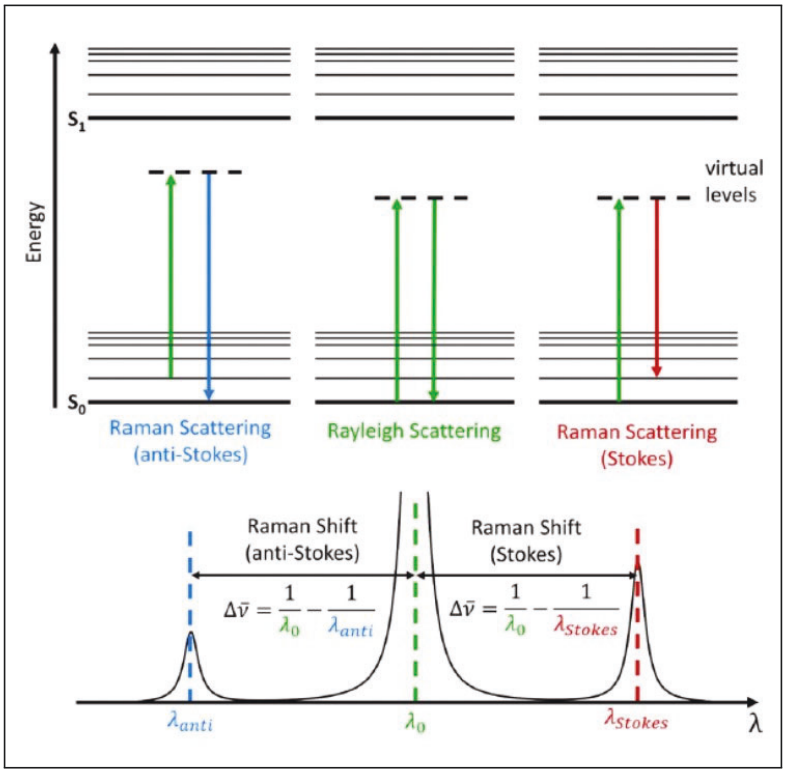

Figure 3.4 Jablonski diagram showing the three types of scattering (Rayleigh, Stokes, and Anti-Stokes) by a molecule excited by a photon with energy $E = h\nu$.

3.2.2.2 Experimental Setup

The Raman spectroscopy setup used in this work is illustrated in Figure 3.5. A He-Ne laser with an emission wavelength of 632.8 nm and a constant power of 1.3 mW was used as the excitation source. A 50X microscope objective was employed to focus the laser beam to a spot diameter of 3 μm on the sample surface. The light beam was directed towards the sample at a right angle by a dichroic mirror, and the resulting Raman scattering was focused back to the dichroic filter. This filter acted as a band-stop filter, attenuating the incident light from the light source nearly completely. Only light with a different wavelength, i.e. Raman scattered light, could pass the filter unaltered. The measured light was then directed by mirrors to a Labram-800 Raman spectrometer, which used a grating to diffract the beam into a narrow band of wavelengths. The number of photons at each wavelength was measured by a nitrogen-cooled CCD detector (charged-coupled device), which measured a certain number of photoelectrons contained in a pixel. Finally, the measured data could be saved and evaluated on a computer using appropriate software.

In Chapter4 and 6, we discuss the results of Raman spectroscopy for studying the structure and

amount of strain in AlN films.

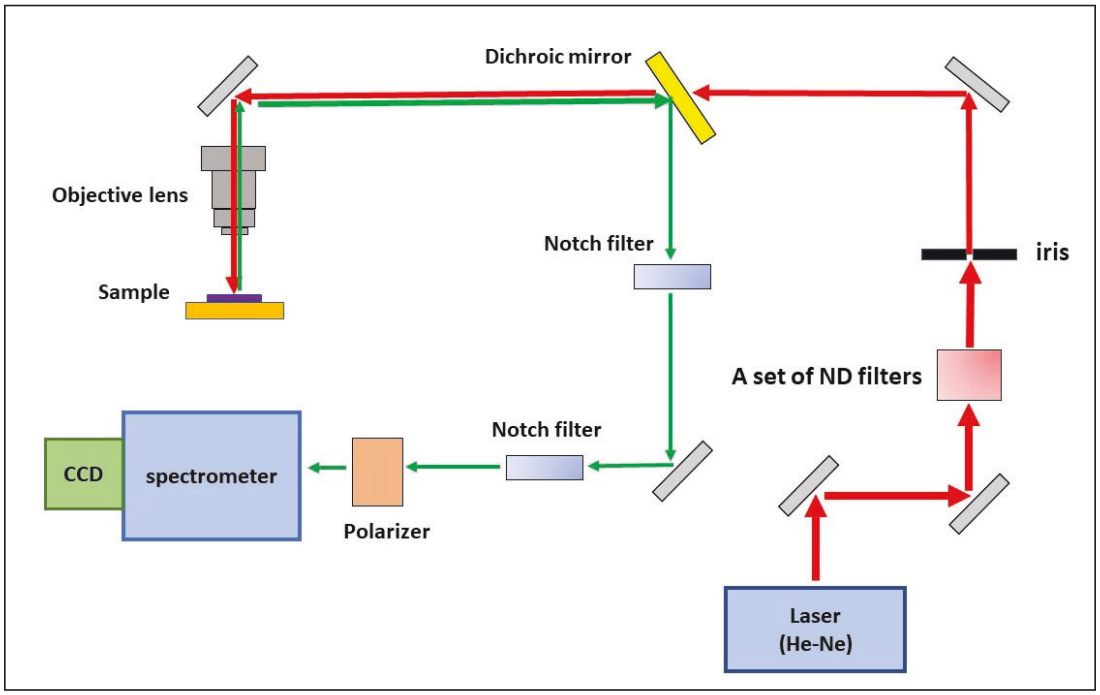

Figure 3.5 Experimental setup for Raman spectroscopy in the Department of Physics at the University of Sherbrooke

.

3.2.3 Scanning Electron Microscopy

A scanning electron microscope (SEM) utilizes a beam of electrons to create high-resolution images of a sample by scanning its surface. This differs from optical microscopes, which use light to produce images. Both optical microscopy (OM) and scanning electron microscopy (SEM) are essential techniques for investigating the surface and structure of materials. Electron microscopes offer higher resolution compared to light microscopes because the wavelength of electrons is much smaller than that of visible light. Therefore, electron microscopes can resolve down to approximately 0.1 nm, while light microscopes can only resolve down to about 200 nm.

3.2.3.1 Fundamental Principles

Electron microscopy involves using electrons to scan the surface of a sample. There are three common sources of electrons: tungsten filament, solid-state crystal, and field emission gun. These electrons are accelerated to a voltage of 1-40 kV by a positively-charged anode and

condensed into a narrow beam that is used for imaging and analysis. The electromagnetic lenses, including the condenser and objective, are used to focus the electron beam onto the sample surface to achieve a high resolution of a few nm (for a field emission gun). The SEM system also has a scanning coil, which is used to move the beam across the sample in a raster pattern. All components of the electron microscope must be placed under a high vacuum to protect the electron source from contamination, acquire high-resolution images, and increase the collection efficiency of electrons by the detectors in the column.

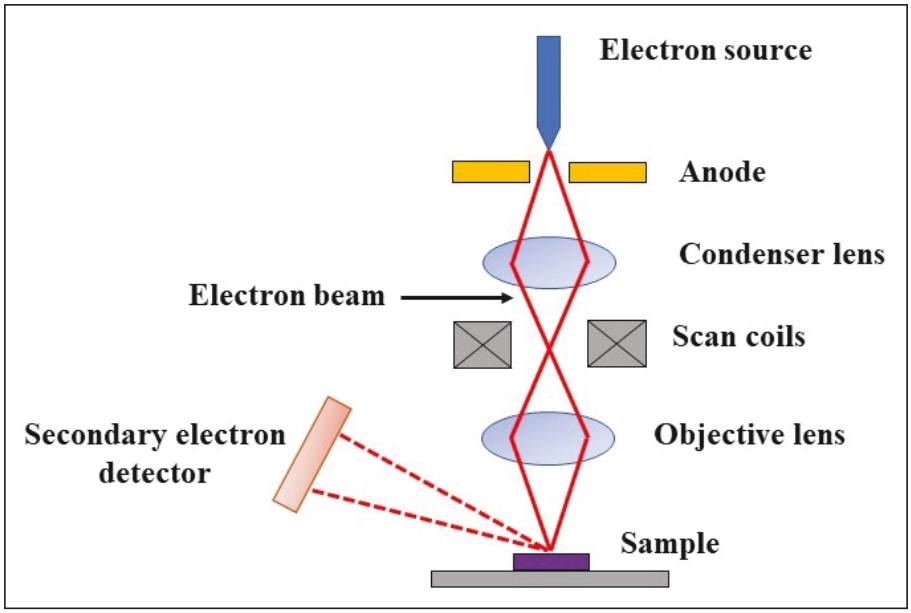

Figure 3.6 A schematic diagram of a scanning electron microscope.

When an electron beam interacts with a sample, different types of interactions can occur, such as the production of secondary electrons, backscattered electrons, Auger electrons, visible photons, or X-rays (shown in Figure 3.7). In scanning electron microscopy, backscattered (BSE) and secondary electrons (SE) are commonly used for imaging. Each detection channel provides different types of contrast and complementary information about the sample's local chemical composition and surface topography.

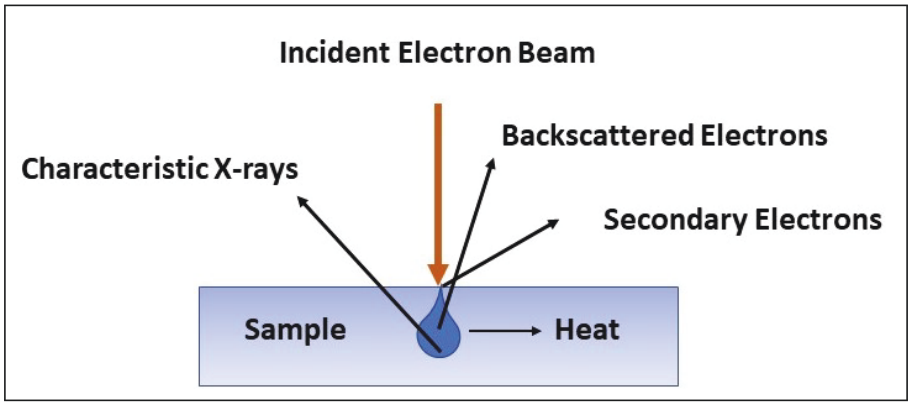

Figure 3.7 Electron Beam Interactions

.

3.2.3.2 Experimental Setup

All scanning electron microscopy (SEM) images presented in this thesis were obtained at the Interdisciplinary Institute for Technological Innovation (3it) at Université de Sherbrooke, using a Zeiss 1540 XB SEM. Prior to SEM imaging, the surfaces of the thin films were cleaned in a Plasmaline system and then coated with a thin metallic layer deposited by sputtering. The coating layer is an ultra-thin (5 nm) layer of gold/palladium (Au/Pd). As AlN is a poorly conducting material, this metallic layer serves to prevent charge accumulation on the sample surface. To evacuate these charges, a contact wire is connected between the metallic surface and the sample holder. The SEM was operated with a beam voltage of 20 kV, a spot size of approximately 1 nm, and a dwell time of $t_D = 10^4$ s. The image array size was 1024×884. It should be noted that these SEM working parameters remained constant for all measurements.

3.2.4 Atomic Force Microscopy

Atomic Force Microscopy (AFM) is a scanning probe method that was first introduced by Binnig, Quate, and Gerber in 1985 [129]. This precise and non-invasive technique is used to analyze the surface morphology and material properties of samples at the nanoscale in various environments, such as air, liquids, or ultrahigh vacuum. The basic principle of scanning probe microscopy is used, where a physical probe is employed to measure the surface characteristics of the samples, providing atomic resolution measurements for both lateral and vertical dimensions.

3.2.4.1 Fundamental Principles

The AFM (Atomic Force Microscope) utilizes a feedback loop to regulate the parameters required for surface imaging while a sharp tip is scanned over it. Unlike relying on the quantum mechanical phenomenon of tunneling, the AFM can utilize atomic forces to map the tip-sample interaction. Furthermore, the AFM is capable of imaging non-conducting samples. To accommodate varying surface types, different operating modes such as contact, non-contact, and tapping are available.

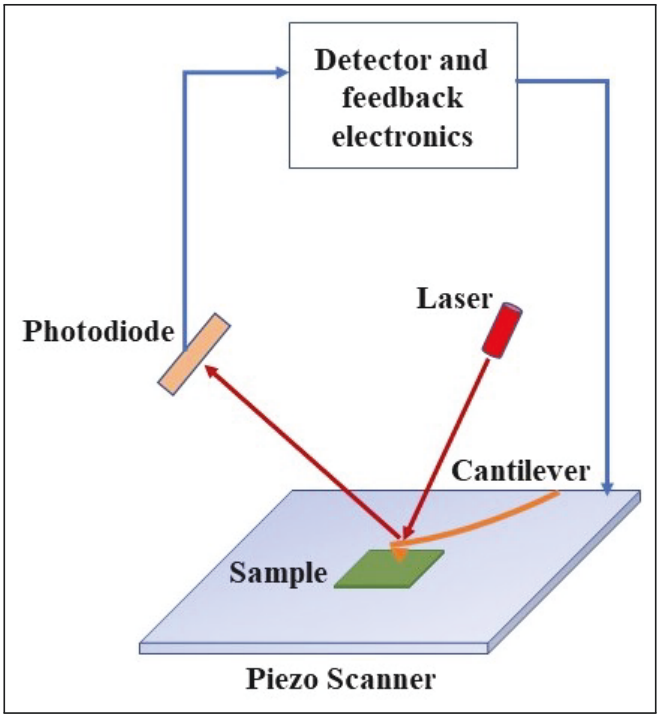

Figure 3.8 Schematic illustrations showing the basic principles of AFM.

The AFM operates based on the concept that a nanoscale tip is mounted on a small cantilever, which acts as a spring. When the tip makes contact with the surface, the cantilever deflects, and this deflection is detected with a laser diode and a split photodetector. The degree of deflection indicates the force of interaction between the tip and the sample. In contact mode, the tip is pressed onto the surface, and an electronic feedback loop maintains a constant deflection while scanning the surface.

Tapping mode is used to minimize damage to both the sample and tip by limiting the contact between them. In this mode, the cantilever is vibrated at or near its resonance frequency. The tip moves up and down in a sinusoidal pattern, which is attenuated by attractive or repulsive forces as it approaches the sample. A feedback loop is employed in a similar manner to contact

mode, but it maintains a constant amplitude of tapping motion rather than the quasi-static deflection. This method traces the topography of the sample line by line. Additionally, an AFM system can record force-distance curves point by point on the sample surface, which can be used to obtain quantitative measurements of the force between the tip and the sample.

3.2.4.2 Experimental Setup

To analyze the surface topography and root-mean-square (RMS) roughness of AlN thin films, the researchers utilized atomic force microscopy (AFM) in a non-contact mode, employing a Dimension Icon Bruker system. To determine the surface roughness parameters, the researchers used the statistical tools available in Gwyddion software [130].

3.2.5 Elastic Recoil Detection by Time-Of-Flight analysis

Elastic Recoil Detection by Time-Of-Flight (ERD-TOF) analysis is a technique used to determine the elemental composition and depth profile of materials. In ERD-TOF, a high-energy ion beam is directed at a sample, and the resulting elastic recoil atoms are measured by their time-of-flight (TOF) using a detector. The TOF provides information about the energy of the recoiled atoms, which is proportional to their mass. By measuring the TOF spectrum of the recoiled atoms, the elemental composition of the sample can be determined. Additionally, the depth profile of the sample can be obtained by varying the energy of the incident ion beam and measuring the corresponding changes in the TOF spectra. ERD-TOF is a powerful technique used in a variety of fields, including materials science, surface analysis, and nuclear physics. [131].

Elastic Recoil Detection by Time-Of-Flight (ERD-TOF) analysis is often used after thermal annealing to characterize the changes in the elemental composition and depth profiles of materials. Thermal annealing is a process that involves heating a material to high temperatures, which can result in changes to the surface and subsurface properties. ERD-TOF analysis can be used to determine how the annealing process has affected the elemental composition and depth profile of the material.

For example, in semiconductor device fabrication, thermal annealing is often used to activate dopants and repair crystal damage. ERD-TOF analysis can be used to determine the depth profile and concentration of dopants in the material before and after annealing. This information can be used to optimize the annealing process and improve device performance.

Our study utilized ERD-TOF analysis to investigate the impact of varying annealing atmospheres on the surface morphology and oxygen content of AlN films.

3.2.5.1 Fundamental Principles

Elastic Recoil Detection by Time-Of-Flight analysis (ERD-TOF) is a technique used for the analysis of the elemental composition of thin films and surfaces. It involves bombarding a sample with high-energy ions, which in turn cause elastic collisions with atoms in the sample. This results in the emission of recoiling atoms or ions from the sample surface. The recoiling particles are then detected and analyzed based on their energy and time-of-flight (TOF) using a detector system.

The basic principle of ERD-TOF analysis is that different elements have different masses, which results in different energies and TOF for their recoiling particles. The time-of-flight between a pair of timing detectors in a start-stop configuration is measured, as well as the energy of the recoils with an energy detector. The recoils originating from deeper in the sample will have less energy, or correspondingly longer time-of-flight, than those originating from the surface. This allows the recoiling particles to be separated and analyzed according to their mass and energy, providing information on the elemental composition of the sample [131].

Two key parameters in Elastic Recoil Detection by Time-Of-Flight (ERD-TOF) analysis are the overall time resolution of the detectors and the solid angle subtended by the detector telescope. The time resolution of the detectors is determined by $\Delta t = \sqrt{\Delta t_1^2 + \Delta t_2^2 + \Delta t_{geom}^2}$, where Δt_1 and Δt_2 are the resolutions of the first and second time detectors, respectively, and Δt_{geom} is related to geometric spreading, including multiple scattering, between the two detectors [132]. The solid angle can be optimized by shortening the distance between the time detectors (L) while maintaining mass resolution by improving the detector resolution. A schematic diagram of an ERD-TOF system is depicted in Figure 3.9. .

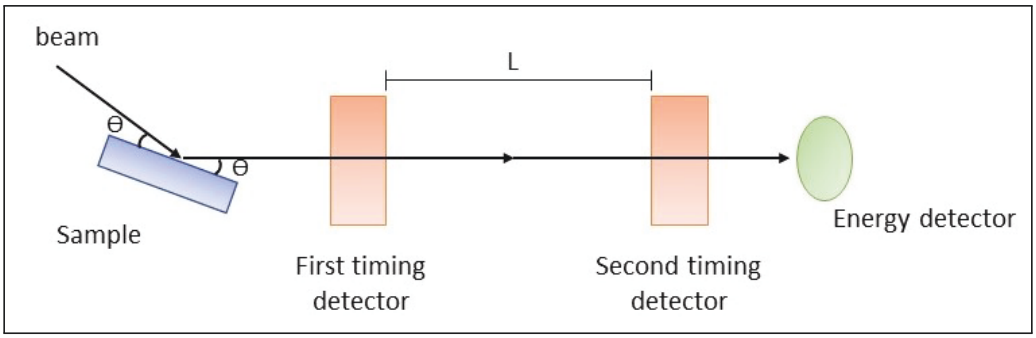

Figure 3.9 Schematic diagram of ERD-TOF setup. θ is the scattering angle and L is the distance between the first and second timing detector.

.

3.2.5.2 Experimental Setup

In this study, the Elastic Recoil Detection by Time-Of-Flight (ERD-TOF) technique was utilized at Université de Montréal. The time-of-flight unit includes two detectors with thin carbon membranes and microchannel plates (MCP) to generate start and stop signals, with a near-surface resolution of 4 nm. The AlN samples' O, H, and C content were measured using a Co 40 MeV ion beam, which was incident at 15° angle to the surface. Recoils were detected at 30° from the beam axis, except for H, which was detected at 46° through a beam-absorbing foil. The energy spectra were transformed into elemental depth profiles using the Allegria software [133]. The findings obtained from the ERD-TOF methodology are presented in Chapter 4.

3.3 Optical Characterization

3.3.1 Luminescence Processes in Semiconductors

Semiconductors are materials that have a conductivity between that of a conductor and an insulator. When semiconductors are excited by energy sources such as light or heat, they can emit light through a process called luminescence. There are two main types of luminescence processes in semiconductors: photoluminescence and electroluminescence.

Photoluminescence (PL) is the emission of light by a material that has been excited by photons, usually from a laser or other light source. In semiconductors, photoluminescence occurs when electrons in the material absorb photons and move to higher energy levels. As these electrons return to their lower energy levels, they release energy in the form of photons. The energy of the emitted photons is related to the bandgap of the semiconductor material, which is the energy difference between the valence band and the conduction band.

Electroluminescence (EL) is the emission of light by a material that is under the influence of an electric field. This process occurs in materials such as light-emitting diodes (LEDs) and is based on the injection of minority carriers (electrons or holes) into the semiconductor. When the minority carriers recombine with the majority carriers (holes or electrons, respectively), energy is released in the form of photons.

In both types of luminescence processes, the emitted light carries information about the material's properties, including the bandgap energy, the density of defects, and the distribution of carrier concentrations. Therefore, luminescence spectroscopy can be used as a powerful tool for studying the electronic properties of semiconductors, including their doping levels, purity, and crystal structure.

After ion implantation, the properties of a material can change significantly, which can lead to the introduction of new defects or changes in existing defects within the material. One way to detect these changes is by using PL spectroscopy, a non-destructive technique that measures the amount and type of light emitted from a material when excited by a laser. This technique is particularly useful because it allows for the detection of defects on a microscopic level, which cannot be seen with the naked eye.

PL spectroscopy works by exciting electrons within a material to a higher energy level, causing them to emit photons when they return to their original energy state. By analyzing the wavelengths and intensities of the emitted light, researchers can identify the types of defects present within the material. For example, changes in the intensity and wavelength of the emitted light can indicate the presence of new defects, while shifts in the energy levels can provide information about the location and type of defects within the material.

3.3.1.1 Fundamental Principles of Photoluminescence Spectroscopy

Photoluminescence (PL) spectroscopy is a widely used technique to study the electronic and optical properties of materials, particularly semiconductors. The technique measures the emission of light from a material after it has been excited by photons, which leads to the recombination of excited charge carriers.

The process of PL can be explained by the recombination of excited charge carriers in a semiconductor. When a semiconductor is excited by light, electrons in the valence band (VB) absorb energy and are excited to the conduction band (CB), leaving holes behind in the VB. The excited electrons and holes then migrate to the respective energy minima in the CB and VB and form bound excitons. These excitons can recombine either radiatively or non-radiatively. Radiative recombination occurs when the excited electron and hole recombine and emit a photon of light, which is detected by the PL spectrometer. Non-radiative recombination occurs when the excited electron and hole recombine without emitting a photon, resulting in energy loss as heat. Non-radiative recombination can occur through a variety of mechanisms, such as trapping of carriers by defects or impurities, Auger recombination, or surface recombination [134].

The efficiency of radiative recombination depends on the material's band structure, which is characterized by the energy bandgap between the CB and VB. In direct bandgap semiconductors, such as GaAs and InP, the energy difference between the CB and VB is such that the recombination of an electron and hole can directly emit a photon, resulting in a high PL efficiency. On the other hand, in indirect bandgap semiconductors, such as Si and Ge, the momentum conservation rule requires the involvement of a phonon to conserve momentum in the recombination

process, leading to a low PL efficiency [134].

Defects in semiconductors can have a significant impact on the efficiency and characteristics of PL emission. Intrinsic defects, such as vacancies, interstitials, or antisite defects, and extrinsic defects, such as impurities or dopants, can act as recombination centers, leading to non-radiative recombination and reducing PL intensity. Non-radiative recombination can occur when an excited electron or hole relaxes to a defect level within the bandgap instead of recombining with its counterpart. The excited electron or hole can then undergo a non-radiative relaxation process, releasing its energy as heat instead of emitting a photon. The presence of impurities in a semiconductor can introduce energy levels within the bandgap, leading to an energy transfer from the excited electron to the impurity center, causing non-radiative recombination. Additionally, structural defects, such as dislocations or stacking faults, can act as non-radiative recombination centers, reducing the PL intensity.

In contrast to non-radiative recombination centers, certain defects can act as radiative recombination centers, enhancing PL emission. Radiative recombination occurs when an excited electron and hole recombine and emit a photon. For example, quantum dots or nanocrystals can act as radiative recombination centers, leading to bright and sharp emission peaks. These nanocrystals have a confined size and shape, which leads to the quantization of energy levels and results in discrete energy levels that act as radiative recombination centers. The discrete energy levels within the quantum dots or nanocrystals are separated by energy gaps, resulting in sharp emission peaks [134].

The type of semiconductor also affects the radiative and non-radiative recombination processes. Direct bandgap semiconductors have a small energy difference between the conduction and valence bands, allowing electrons and holes to recombine radiatively with a high probability. Indirect bandgap semiconductors, on the other hand, have a large energy difference between the conduction and valence bands, leading to a low probability of radiative recombination. The electrons and holes in indirect bandgap semiconductors typically undergo non-radiative recombination via phonon emission, which results in heat dissipation rather than light emission.

Furthermore, the shape and position of the PL spectrum can provide valuable information about the material's properties. The position of the PL peak is related to the bandgap energy of the semiconductor, while the width of the peak is related to the broadening of the energy levels due to various mechanisms such as exciton-phonon coupling or impurity-related recombination. The PL spectrum can also provide information about the material's defects, such as their type, concentration, and distribution. By analyzing the PL spectrum, one can obtain information on the material's quality, doping level, carrier lifetime, and other important properties [134]. Figure(3.10) shows a schematic illustration of the radiative and non-radiative recombination

processes in both direct and indirect bandgap semiconductors.

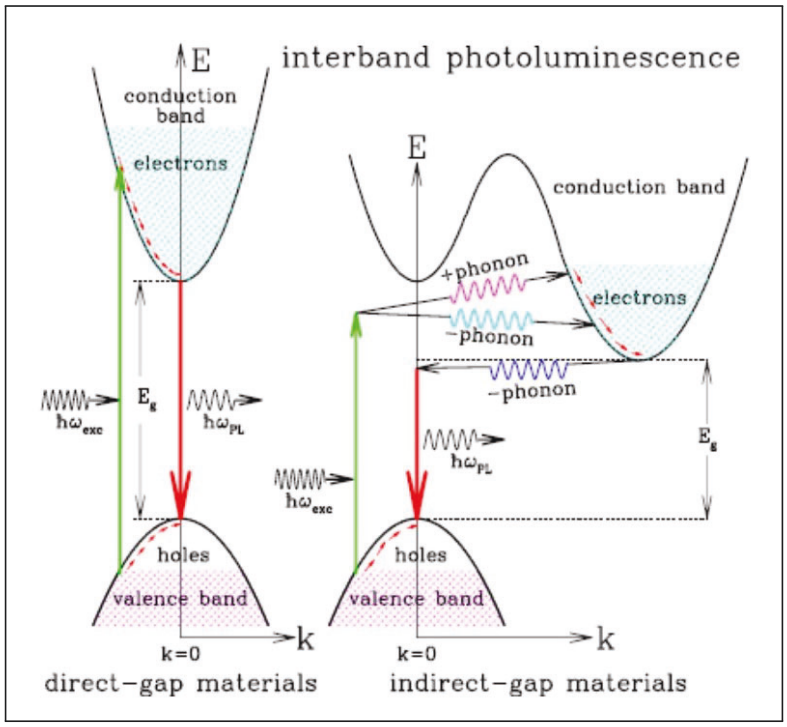

Figure 3.10 Schematic illustration of radiative and non-radiative recombination processes in both direct and indirect bandgap semiconductors. The radiative recombination process results in the emission of a photon, while non-radiative recombination results in the loss of energy as phonons. [5]

3.3.1.2 Experimental Setup

In this thesis, the study of photoluminescence (PL) spectroscopy involves exciting an AlN sample with laser light and measuring the resulting emission spectrum. The conventional PL setup was used for the measurements presented in Chapter.4. The PL spectra were acquired at room temperature using a 1 m-spectrometer (SPEX model) equipped with a cooled photomultiplier tube (Hamamatsu R2658 model). An 8 mW pulsed UV laser source emitting at 266 nm was used as the excitation source, and the laser beam was focused onto the sample surface with a spot diameter of approximately 200 μm. The laser beam was almost perpendicular to the c-plane surface of the AlN films, and the PL signals were recorded using a conventional lock-in technique. Figure.3.11 shows a schematic of the PL setup used in the study.

Chapter 5 utilized a laser source emitting photon pulses at a wavelength centered at 532 nm with a duration of approximately 80 ps for micro-photoluminescence (μPL) and time-resolved photoluminescence (TRPL) measurements. The experimental setup for μPL measurements is

illustrated in Figure 3.12. The photoluminescence (PL) spectroscopy measurements were carried out by placing the samples on a continuous flow liquid helium cryostat's cold finger, where the temperature could be varied

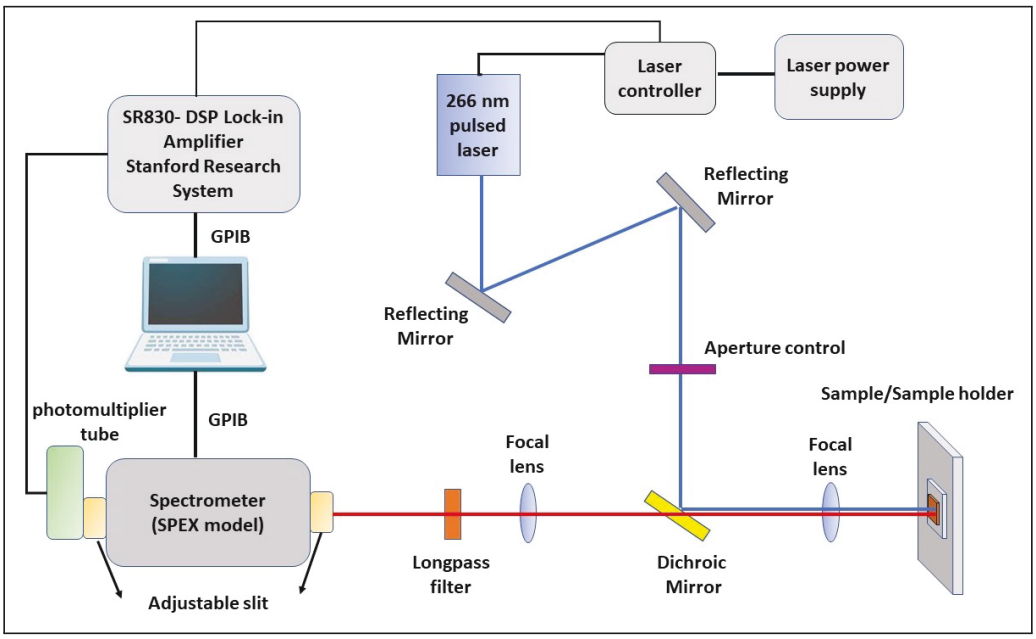

Figure 3.11 Schematic diagram of the conventional photoluminescence setup

.

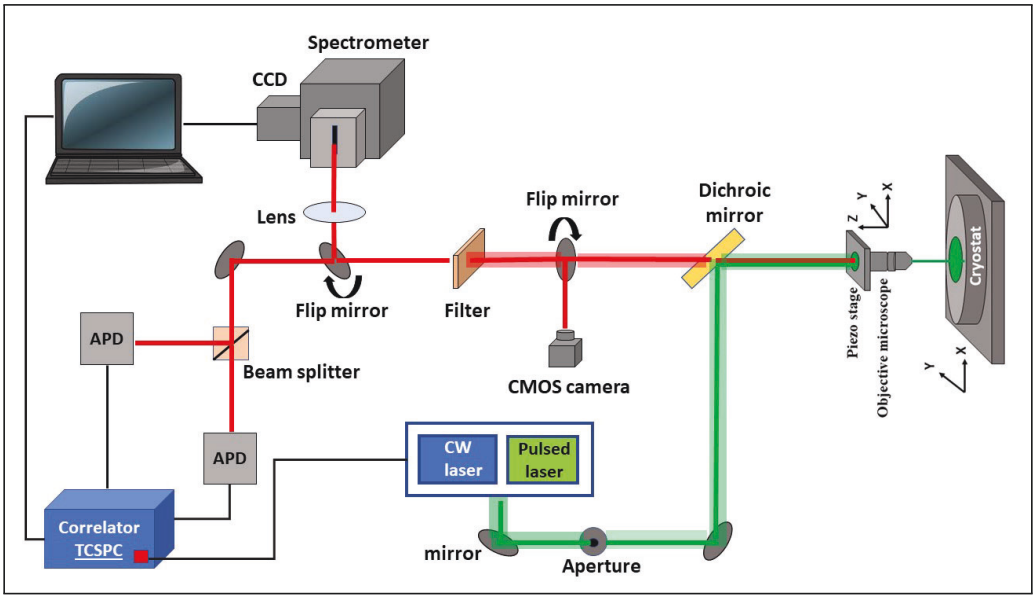

Figure 3.12 Schematic diagram of the micro-photoluminescence setup.

from 4 K to 290 K. A 60X microscope objective was used to focus the laser beam onto the sample surface at normal incidence. The same objective was used to collect the μPL emission from the sample, which can be imaged using a removable lens and flip mirror in conjunction with a CMOS camera. The μPL was then collected by a monochromator (Horiba Triax 320) and a Symphony Jobin-Yvon liquid nitrogen-cooled CCD camera. For TRPL, an avalanche photodiode (APD) was used with a time-correlated single photon counting (TCSPC) unit (MultiHarp 150 from PicoQuant).

3.3.2 Photoluminescence Excitation Spectroscopy

Photoluminescence Excitation Spectroscopy (PLE) is a technique used to investigate the electronic transitions in a material. It involves illuminating the sample with light of various wavelengths, while monitoring the resulting photoluminescence emission. By measuring the spectrum of the emitted light as a function of the excitation wavelength, one can obtain information about the electronic states and energy levels of the material.

In PLE, a monochromatic light source is used to excite the sample, typically a semiconductor or a luminescent material. The emitted light is then analyzed using a spectrometer, allowing the measurement of the photoluminescence spectrum. By varying the excitation wavelength and measuring the corresponding photoluminescence spectrum, one can map out the electronic transitions and energy levels of the sample.

PLE is particularly useful for investigating the energy band structure of semiconductors, which is important for understanding their electronic and optical properties. It is also used to study luminescent materials such as organic dyes and quantum dots, as well as defects and impurities in semiconductors [135–137].

3.3.2.1 Experimental Setup

The Photoluminescence Excitation (PLE) spectra were acquired in this study using an FLS980 Phosphorimeter manufactured by Edinburgh Instruments. The instrument is equipped with a 200-Watt Xenon lamp that is coupled to a monochromator (Princeton Instrument SP-2300i), which facilitates the selection of an excitation wavelength. The emission monochromator is connected to two detectors: an R928 PMT and an R3809U-50 (MCP-PMT), as shown in Figure.3.13.

The use of these detectors allows for the collection of emitted light intensity as a function of excitation wavelength at a fixed emission wavelength. This technique enables the characterization of a sample's optical properties by monitoring the excitation energy required to promote

electrons to higher energy states. By measuring the PLE spectrum of a material, one can determine the absorption and emission energies of the sample.

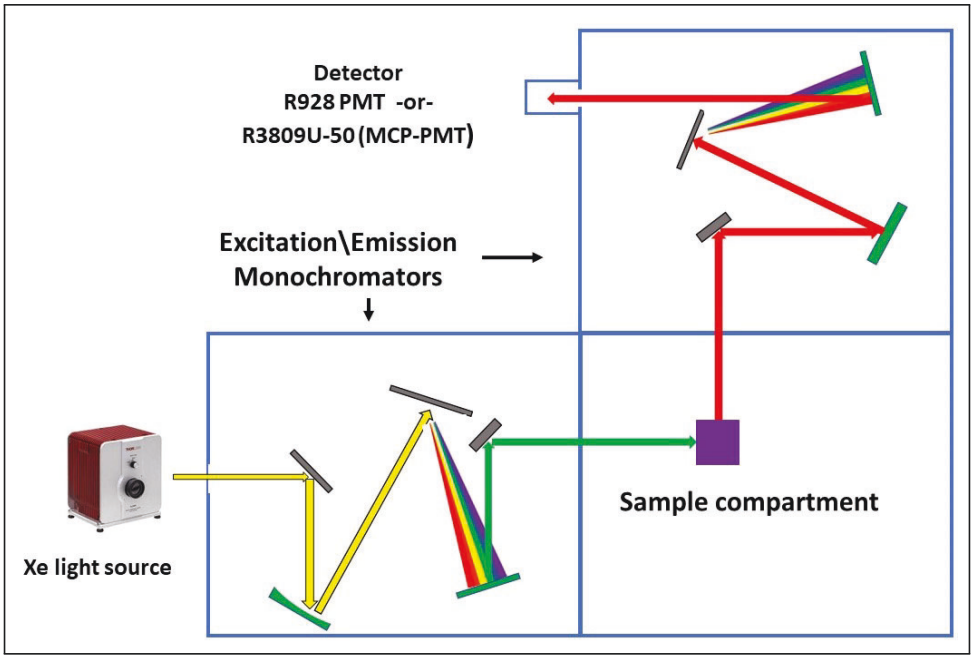

Figure 3.13 Schematic diagram of the FLS980 Phosphorimeter by Edinburgh Instruments used for obtaining photoluminescence excitation (PLE) spectra in this study

3.4 Electron Spin Resonance Spectroscopy

The phenomena of electron spin resonance (ESR), also called as electron paramagnetic resonance (EPR) was discovered by the soviet physicist Zavoisky [138], one year before the discovery of the nuclear magnetic resonance (NMR) technique. ESR and NMR are both based on the same physical principle of resonance, which is the absorption of electromagnetic radiation by a sample when the frequency of the radiation matches the energy difference between two energy states of the sample. However, the frequency range used for these techniques is different due to the difference in the magnetic moments and gyromagnetic ratios of the particles being studied.

In NMR, the sample is composed of nuclei that have a non-zero spin, such as hydrogen-1, carbon-13, or nitrogen-15. These nuclei have a small magnetic moment and a gyromagnetic ratio that is on the order of 10^7 Hz/T. To excite the nuclear spin states and observe resonance, radiofrequency (RF) radiation is used, typically in the range of 10-1000 MHz. This frequency range corresponds to the energy difference between the nuclear spin states, which is on the order of micro-electron volts (μeV).

In ESR, the sample is composed of unpaired electrons, which have a larger magnetic moment and a gyromagnetic ratio that is on the order of 10^{10} Hz/T. To excite the electron spin states and observe resonance, microwave (MW) radiation is used, typically in the range of 1-100 GHz. This frequency range corresponds to the energy difference between the electron spin states, which is on the order of milli-electron volts (meV).

Therefore, the choice of frequency range for NMR and ESR is based on the magnetic properties of the particles being studied and the energy difference between their spin states.

ESR spectroscopy is a highly sensitive technique that is primarily used for studying systems with unpaired electrons. These systems include organic or inorganic free radicals, triplet states, transition metal ions, their complexes, and metalloproteins with unpaired d-or f-electrons. The technique is based on the measurement of the energy difference between the two possible spin states of an unpaired electron in a magnetic field. However, the application of ESR spectroscopy is limited to such systems, where unpaired electrons are present.

ESR spectroscopy finds its applications in a wide range of fields such as material science, chemistry, biology, and physics. It is used for studying chemical reactions, characterizing free radicals, determining the structure of metal complexes, analyzing paramagnetic centers in biological systems, and investigating magnetic properties of materials. Despite its limitations, the high sensitivity of ESR spectroscopy makes it an important tool for the analysis of a variety of systems that have unpaired electrons [139, 140].

3.4.1 Fundamental Principles

3.4.1.1 Spin Hamiltonian of Electron Spin Resonance

The Spin Hamiltonian H_0 is a mathematical equation used for determining the energy levels of a spin system. In the case of a spin system consisting of nuclear spins and a single electron (or multiple strongly-coupled electrons within a single paramagnetic center), H_0 can be expressed as given by [141]:

$$H_0 = H_{EZ} + H_{NZ} + H_{HF} + H_{NQ} + H_{NN} + H_{ZFS} \tag{3.5}$$

$$H_0 = \beta_e B_0 g S/\hbar - \beta_n \sum_{k=1}^{I} g_{n,k} B_0 I_k/\hbar + \sum_{k=1}^{I} S A_k I_k + \sum_{k>\frac{1}{2}} I_k Q_k I_k + \sum_{i\neq k} I_i d_{ik} I_k + SDS \tag{3.6}$$

The six energy terms in the Spin Hamiltonian (given in angular frequency units) represent the electron Zeeman, nuclear Zeeman, hyperfine, nuclear quadrupole, nuclear-nuclear, and zero-field splitting interactions. The Bohr magneton (β_e) and nuclear magneton (β_n) are also

included in the equation. The electron spin operator, S, has an electron-spin quantum number S = n/2, where n is the number of unpaired electrons, while the nuclear spin operator, I, has a nuclear-spin quantum I that depends on the nucleus in NMR. If multiple non-interacting paramagnetic centers are present, each center has its own spin Hamiltonian. For interacting paramagnets, additional coupling terms need to be added [141].

The terms H_{NZ} and H_{NQ} are usually used in pulsed ESR measurements, but since this study utilized CW-ESR, these terms were not included. Additionally, H_{NN} is related to NMR measurements and therefore not included in the final Hamiltonian of this study. Thus, the final Hamiltonian for the unpaired electrons in AlN films is:

$$H_0 = H_{EZ} + H_{HF} + H_{ZFS} \tag{3.7}$$

3.4.1.2 The Electron Zeeman Interaction (H_{EZ})

Even in the absence of external forces, an isolated electron possesses intrinsic angular momentum referred to as "spin", denoted by $\overline{S}$. Being charged, the spinning motion of this charged particle creates a magnetic field. This means that the electron acts like a tiny bar magnet or magnetic dipole, with a magnetic moment denoted by $\overline{\mu}$. The difference in energy observed in ESR is due to the interaction between the magnetic moment of the unpaired electron and an external magnetic field B_0, known as the Zeeman Effect. The external magnetic field creates two energy states for the electron's magnetic moment. The unpaired electron occupies the lowest energy state when its spin projection is aligned with the magnetic field, while it occupies the highest energy state when the $\overline{\mu}$ is aligned in the opposite direction of the magnetic field. Since an electron is a spin 1/2 particle, these two spin projections are referred to as the parallel state ($m_s = -1/2$) and antiparallel state ($m_s = 1/2$). The energy of each orientation is determined by μ and B_0. For an electron, $\mu = m_s g_e \beta$, where m_s is the electron spin, g_e is the spectroscopic g-factor (2.0023192778 for a free electron), and β is the conversion constant called the Bohr magneton. Therefore, the energy difference between the two energy states is equal to $g_e \beta B_0$. Figure.3.14 illustrates the energy states of the unpaired electron.

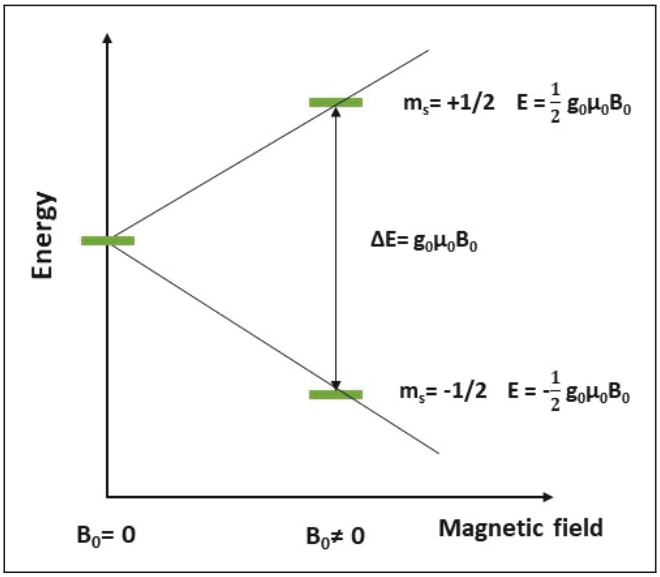

Figure 3.14 The variation of spin state energies with respect to the magnetic field B_0.

3.4.1.3 The Electron–Nuclear Hyperfine Interaction (H_{HF})

The magnetic moment of an electron behaves like a bar magnet and aligns itself with an external magnetic field. Similarly, it can interact with neighboring magnetic nuclei. The interaction between an unpaired electron and a nuclear magnetic moment is known as nuclear hyperfine interaction. When the hyperfine interaction results from the nucleus where the unpaired electron originates, it is referred to as hyperfine, and when it is from a neighboring nucleus, it is known as super hyperfine.

The Zeeman splitting is much larger than the hyperfine interaction because the Zeeman interaction arises from the interaction between the magnetic moment of the electron and the external magnetic field, which can be very strong. On the other hand, the hyperfine interaction arises from the interaction between the magnetic moment of the electron and the magnetic moments of the surrounding nuclei, which are typically much weaker than the external magnetic field.

As a result, the Zeeman interaction dominates over the hyperfine interaction and can be treated as the primary interaction governing the energy levels of the spin system. The hyperfine interaction can then be treated as a perturbation to the Zeeman interaction. This can be shown with the expression S.A.I, where A is the anisotropic hyperfine tensor. The hyperfine interaction terms split the Zeeman transition into 2I+1 lines of equal intensity. For instance, if an electron interacts with a nucleus with I = 1/2, an ESR spectrum with two lines will be produced. The local field of the nucleus either adds or subtracts from the applied magnetic field, resulting in the splitting of the ground-state and excited-state energy levels into two levels. Consequently,

we observe two lines instead of one in the EPR experiment. However, not all transitions are allowed due to selection rules (Figure.3.15). The selection rule for hyperfine transitions is given by $\Delta m_s = \pm 1; \Delta m_I = 0$ [141].

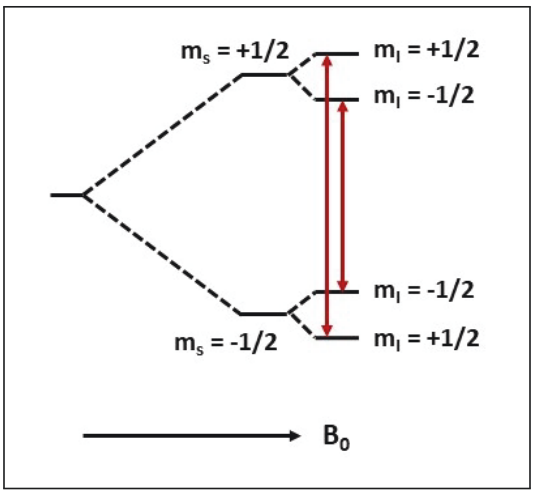

Figure 3.15 Splitting of electron spin energy levels hydrogen atom by magnetic field and due to effects of nuclear spin on these levels.

3.4.1.4 Spin- Orbit Interaction

Spin-orbit coupling is an interaction between the spin of an electron and its motion around a nucleus that can affect the energy levels and spectral properties of atoms and molecules. The coupling arises from the interaction between the magnetic field produced by the electron's motion and the intrinsic magnetic moment associated with its spin.

In the presence of spin-orbit coupling, the energy levels of an atom are split into sub-levels that have slightly different energies. This splitting can be observed in atomic spectra as fine structure, where spectral lines that would otherwise appear as single lines are split into multiple lines with slightly different energies.

$$\overline{\mu} \propto g_e \overline{S} + \text{spin- orbit coupling contribution} \tag{3.8}$$

The strength of spin-orbit coupling depends on several factors, including the atomic number of the nucleus, the size and shape of the electron's orbit, and the strength of the electron's magnetic moment. Elements with heavier nuclei tend to exhibit stronger spin-orbit coupling because the larger electric field generated by the nucleus affects the motion of the electron more strongly.

Spin-orbit coupling also plays a role in the behavior of electrons in magnetic materials and in the interaction between spin and orbital motion in electronic devices such as spintronic devices [141].

A different way to conceptualize spin-orbit coupling is to imagine an electron as if it were a tiny observer, experiencing the motion of the positively charged nucleus (or nuclei) as an orbiting charge. This creates a secondary magnetic field, denoted as δB, which interacts with the electron's intrinsic magnetic moment, causing the energy levels to split into fine structure.

$$h\nu = g_e\beta(B_e + \delta B) \tag{3.9}$$

or

$$h\nu = (g_e + \delta g_e)\beta B = g\beta B \tag{3.10}$$

The parameter 'g', which is defined as '$g_e + \delta g_e$', encodes valuable chemical information about the electronic structure and bonding in a molecule. Specifically, it reflects the nature of the bond between the electrons and the molecule, offering insights into the electronic properties of the molecule [142].

3.4.1.5 Strongly-Coupled Electrons: the Zero-Field Splitting Interaction (H_{ZFS})

Zero-Field Splitting (ZFS) is a type of interaction between the magnetic field created by an unpaired electron and its surrounding environment. This interaction can result in a splitting of the energy levels of the electron when it is in a zero magnetic field. The ZFS can be characterized by a tensor, known as the D tensor, which has both magnitude and direction. The D tensor represents the zero-field splitting of the electron spin energy levels in a magnetic field-free environment.

The D tensor can be represented as a symmetric matrix with three eigenvalues (Dx, Dy, and Dz) and associated eigenvectors (ex, ey, and ez). The eigenvalues of the D tensor correspond to the energy differences between the spin states of the electron in the absence of an external magnetic field. The eigenvectors represent the orientation of the principal axes of the tensor.

In some cases, a second-order contribution to the ZFS arises from an additional term, known as the E tensor. The E tensor is also a symmetric matrix with three eigenvalues (Exx, Eyy, and Ezz) and associated eigenvectors (exx, eyy, and ezz). The E tensor describes the deviation from spherical symmetry of the environment around the electron, which can cause a slight splitting

of the energy levels.

The D and E tensors can be combined to give the complete ZFS tensor, which can be written as [142]:

$$\mathbf{D} = \begin{pmatrix} D_x & 0 & 0 \\ 0 & D_y & 0 \\ 0 & 0 & D_z \end{pmatrix} \tag{3.11}$$

$$\mathbf{E} = \begin{pmatrix} E_{xx} & 0 & 0 \\ 0 & E_{yy} & 0 \\ 0 & 0 & E_{zz} \end{pmatrix} \tag{3.12}$$

,and

$$\mathbf{ZFS} = \mathbf{D} + \frac{1}{2}\mathbf{E} \tag{3.13}$$

where ZFS represents the complete zero-field splitting tensor, which is the sum of the D tensor and half of the E tensor. The ZFS tensor provides information about the electronic and geometric structure of a molecule or a solid-state material, and it can be determined experimentally using various spectroscopic techniques, such as electron paramagnetic resonance (EPR) spectroscopy or magnetic circular dichroism (MCD) spectroscopy [142].

3.4.1.6 Presentation of Electron Spin Resonance Spectra

In ESR spectroscopy, a paramagnetic sample is subjected to a uniform magnetic field B_0. This magnetic field causes the spin energy levels of the ground state to split, with the energy difference between the levels given by $\Delta E = h\nu = g\beta B_0$, where g is the g-factor. The g-factor determines the magnetic field position at which ESR transition occurs, and is obtained from the energy difference of spin energy (ΔE). The g-value can be determined by either sweeping the magnetic field while keeping the microwave (MW) frequency fixed or by scanning the MW frequency with a constant magnetic field. In our study, we used a JOEL FA-200, X-band spectrometer operating at 9.45 GHz, and fixed the MW frequency while sweeping the magnetic field until the energy of MW photons matched the energy difference between the field-induced energy levels. At this point, an absorption peak occurs when the condition of the equation $\Delta E = h\nu = g\beta B_0$ is satisfied. Direct detection of the absorption signal is only possible for samples with high concentrations of unpaired electrons, as noise components over a wide range of frequencies make signal detection difficult. To overcome this, field modulation using a phase-sensitive detector technique is used to yield a signal proportional to the first derivative, as shown

in Figure. 3.16 (a). Due to the short relaxation time of the paramagnetic system, absorption signals are typically broad, and hyperfine splittings are often buried and not seen (Figure. 3.16 (b)). However, using field modulation, the derivative signal exhibits well-resolved hyperfine features.

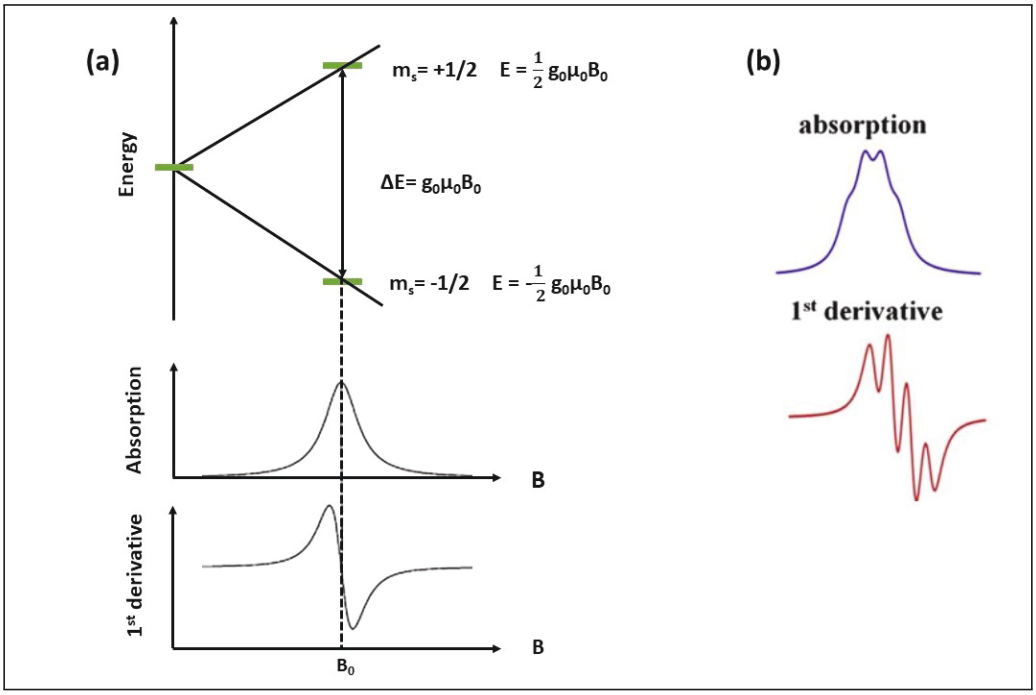

Figure 3.16 Absorption and first derivative electron paramagnetic resonance spectra for single line (a) and multiple lines (b) systems.

3.4.2 Experimental Setup

The ESR measurements presented in this work were carried out using a JOEL FA-200 ESR spectrometer located in the Chemistry department of Western University in London, Ontario (Figure. 3.17 (a)). The ESR setup, depicted in Figure. 3.17 (b), consists of a Gunn diode that generates a monochromatic X-band MW radiation at a frequency of 9.45 GHz. The MW radiation travels through a waveguide to the sample, which is held in a MW cavity positioned in a uniform magnetic field generated and controlled by an electromagnet inside the magnet system. The impedance of the cavity can be adjusted mechanically and electrically. The absorption of the MW radiation by the sample is monitored, amplified, and recorded by the detector and modulation system. To obtain spectra, the absorption of the MW radiation is measured while scanning the magnetic field strength. However, direct detection of the absorption signal is difficult for samples with low unpaired electron concentration due to noise components occurring over a wide range of frequencies. This difficulty is overcome using a phase-sensitive

detector technique with small-amplitude magnetic field modulation at a frequency of 100 kHz. The recorded signal corresponds to the first derivative of the absorption band, as shown in Figure. 3.16.

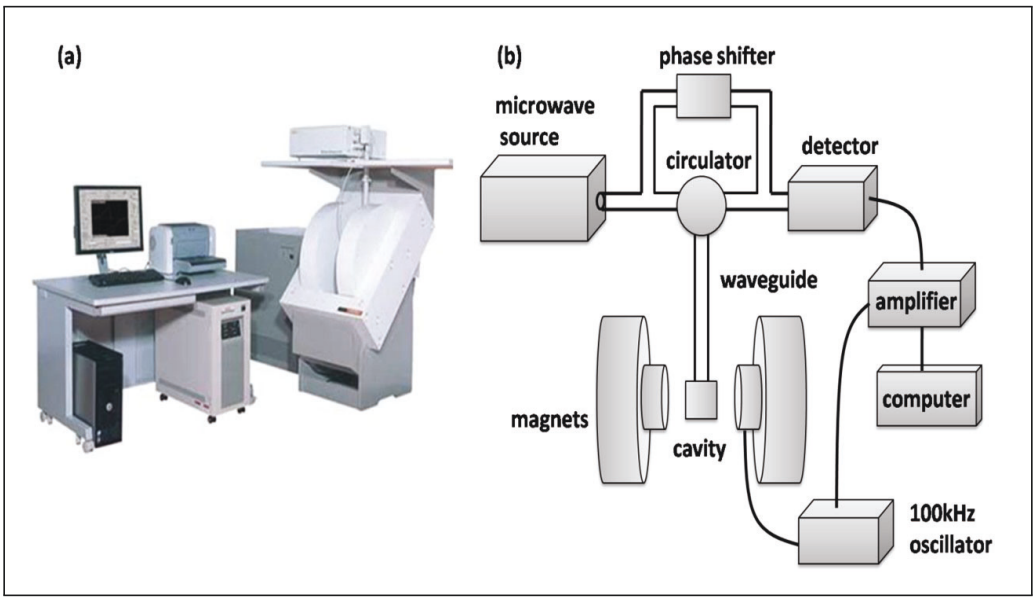

Figure 3.17 (a) Schematic diagram of electron spin resonance (ESR) spectrometer and (b) Photograph of ESR spectrometer.

CHAPTER 4 Engineering Visible Light Emitting Point Defects in Zr-implanted Polycrystalline AlN Films

4.1 Foreword

Abstract We studied the influence of thermal annealing under different gaseous atmospheres, namely argon, nitrogen, and forming gas, on the structural and optical properties of thin polycrystalline Aluminum nitride (AlN) films that underwent high-energy Zirconium ions implantation. Our analysis, based on X-ray diffraction, Raman spectroscopy, scanning electron microscopy (SEM), and atomic force microscopy (AFM) measurements, indicate that the structural and morphological features of the Zr-implanted AlN films are significantly affected by the annealing gaseous environment. Specifically, annealing the films under an argon atmosphere yields the lowest surface roughness with increased grain size. We used Photoluminescence spectroscopy (PL) to identify multiple emission bands in the visible range, originating from various point defects and defect complexes theoretically reported for AlN. Photoluminescence excitation spectroscopy reveals several absorption bands, and we attributed the new peaks at 1.7 eV and 2.6 eV to the $(Zr_{Al} - V_N)^0$ defect complexes. Our findings could potentially lead to the development of novel point defects in AlN, which could be promising for optoelectronics and quantum applications.

Authors and affiliations

- **Azin Aghdaei:** Ph.D candidate, Université de Sherbrooke, Faculty of science, Physics department, Sherbrooke, Quebec, Canada.
- **Rajesh Pandiyan:** R&D Researcher at 3IT Sherbrooke and Teledyne DALSA ,Semiconductor Inc., Bromont, Quebec, Canada.
- **Bouraoui Ilahi:** Research Associate, Université de Sherbrooke, Sherbrooke, Québec, Canada.
- **Martin Chicoine:** Research Associate, Département de Physique, Regroupement québécois sur les matériaux de pointe, Université de Montréal, Montréal, Quebec, Canada.
- **François Schiettekatte:** professor, Département de Physique, Regroupement québécois sur les matériaux de pointe, Université de Montréal, Montréal, Quebec, Canada.
- **Luc G. Fréchette:** Full professour, Université de Sherbrooke, Faculty of Engineering, Mechanical engineering department, Sherbrooke, Quebec, Canada.
- **Denis Morris:** Full professour, Université de Sherbrooke, Faculty of science, Physics de-

partment, Sherbrooke, Quebec, Canada.

Status of acceptance: Submitted: 21 September 2020, Accepted: 1 December 2020, Published Online: 22 December 2020.

Journal: Journal of Applied Physics, AIP publishing, Cite as: J. Appl. Phys. 128, 245701 (2020); doi: 10.1063/5.0030221

Contribution to the document: For this study, the study outline and methodology were proposed by my supervisor Denis Morris and me. I was responsible for determining the ion implantation and thermal annealing conditions, performing all post-implantation treatments, and carrying out most of the structural and all of the optical characterization measurements. Additionally, I analyzed the results and drafted the paper. The sample preparation was contributed by Rajesh Pandiyan, Mohammed El. Gowini, and L. Fréchette. Martin Chicoine and François Schiettekatte performed the ion implantation and ERD-TOF measurements on the AlN films. M. Dion and B. Ihali studied the X-ray diffraction patterns, while G. Laliberté and P-L. Karsenti participated in the preparation of the optical characterization experiments. All authors provided critical comments and contributed to the progress of this work until the article's finalization.

4.2 Introduction

During the last decades wide-bandgap materials like III-Nitride semiconductors and diamond attract considerable attention for their potential applications in the field of high-power electronics, photonics, sensing, and quantum information processing [6, 30, 92, 143–146]. Among the III-Nitrides materials, AlN has the widest direct bandgap of (6.12 eV) [66], high thermal conductivity (about 320 W/mK) [66], excellent optical [67] and dielectric properties, low dielectric constant and good mechanical strength [66], negative electron affinity [68–70] and high piezoelectric co-efficient [71]. These unique properties make AlN a potential candidate for optoelectronics devices [67, 147, 148], microelectromechanical systems (MEMS) [149], surface acoustic wave sensors (SAWs) [150] and electro-optic modulators [151].

Furthermore, point defects and defect complexes in AlN have recently received considerable attention due to their ability to act as qubits, with a spin character that can be tuned by strain engineering [24, 26, 27], and their application as room-temperature quantum emitters [25]. Indeed, negatively charged nitro-gen vacancies, group IV impurity (Ge, Sn, Ti) -vacancy pairs, and more recently large metal ion (Y, La, Zr, Hf) -vacancy pairs in AlN, have been theoreti-

cally reported as promising qubit candidates [24, 26, 27]. These studies have shown, in particular, that the formation of Zr-vacancy pairs is energetically favorable in AlN while such defects have spin-triplet ground states with an electronic configuration similar to that of the nitrogen-vacancy centers in diamond. It is possible to generate this type of defects using a post-growth ion-implantation technique. This can be achieved firstly by bombarding a lightly Zr-doped AlN film with low-energy protons (necessary to create vacancies in the doped film) or secondly by directly implanting heavy Zr ions into an unintentionally doped film. In both cases, it is necessary to perform a post-implantation thermal annealing treatment to remove most of the implantation damage and to promote the formation of Zr-vacancy pairs. The first method requires an optimization of the deposition conditions to obtain a film with the right doping level, which has not yet been done within our group. Moreover, it is still difficult to obtain this type of film commercially. The second method, which we have advocated for this study, controls the Zr concentration via the implantation dose and the depth distribution of these atoms through the choice of implantation energies. How-ever, the damage and defects caused by the implantation of heavy ions in the AlN film are more important. It is therefore essential to study the influence of thermal annealing conditions on the structural and optical properties of the implanted AlN films.

So far, the impact of different ion species (Si, Cd, Ag, Hf and Ti) on the structural properties of ion-implanted AlN thin films have been reported [152–158] but further studies are needed to better under-stand the influence of thermal annealing conditions on these properties .In this work, we report on the impact of high energy implantation of Zr ions and subsequent annealing in various gaseous atmosphere on the structural and optical properties of polycrystalline AlN thin films. Ti and Hf ions can also create defect complexes of interest for quantum technologies, but we chose Zr ions for their intermediate atomic number and because, to our best knowledge, Zr-implanted AlN films have never been studied before. A special attention has been devoted to the generation and identification of optically active point defects and defect complexes. This study paves the way to future studies exploiting these luminescent defects for single-photon source technologies.

4.3 Experimental Details

AlN thin films were deposited by a reactive DC magnetron sputtering (MS) technique on (100) oriented silicon (Si) substrate. Prior to the deposition process, the substrates were cleaned ex-situ using a standard RCA cleaning process carried out in two steps, called SC1 and SC2. The substrates were then rinsed with deionized water and dried under Nitrogen (N2) gas flow, prior to loading them in the sputtering chamber for the deposition. A commercial high purity

Aluminum (Al) disc with a diameter of 33 cm was used as a target, sputtered at 10 kW operating power. The sputtering process was carried out in an atmosphere composed of a mixture of high purity Argon (Ar) and Nitrogen (N2) gases. The flow rates of gases were regulated by two mass flow controllers and the total gas flow rate (Ar+N2) was kept constant at 70 sccm. The gas flow rates were monitored to maintain a constant pressure of 3 mTorr in the chamber during the sputter-deposition process. The substrates were radiatively heated to an on-substrate temperature of 350 °C and the holder was biased negatively to -37 V. The film thickness was measured using ellipsometry (Optiprime-TF system) and was found to be of 1 μm.

AlN samples of $5 \times 5mm^2$ were cut out of an 8-inch wafer. Before implantation, the samples were carefully cleaned with acetone, IPA and water. Ion implantation was performed at room temperature, using Zr ions at different kinetic energies (250 keV, 1 MeV, 1.75 MeV, and 2.5 MeV). The fluence is fixed at $1 \times 10^{14} cm^{-2}$ for each energy. The depth distribution of displacement damages and Zr atoms in the host material is estimated using SRIM [159] simulations (Figure 4.1).

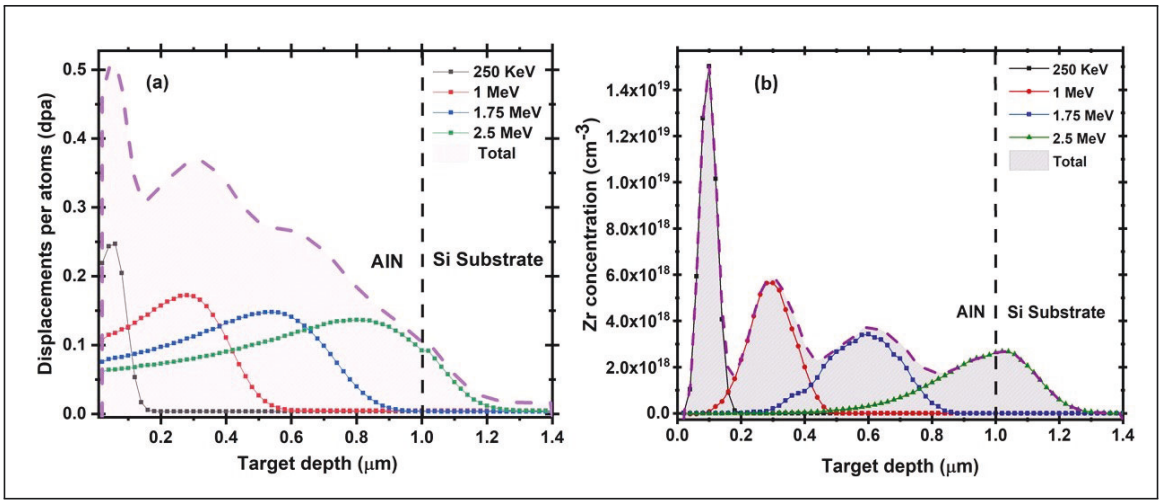

Figure 4.1 Depth profile of (a) displacement damage and (b) implanted ions concentration for different ion implantation energies, according to SRIM simulations. The implantation fluence was $1 \times 10^{14} ion/cm^2$

To partially repair the structural damage caused by ion bombardment, the implanted samples were annealed in a quartz tube furnace. Post-implantation annealing was performed under different atmospheres including argon, nitrogen, and forming gas (FG, 95 % nitrogen + 5 % hydrogen) at 1050 $°C$ for 1 h. Since the AlN films can be easily oxidized when they are exposed to air at high temperature, we allow the samples to cool down to room temperature at a rate of 5 $°C/min$, in the furnace, keeping the same annealing gaseous atmosphere.

The samples' structural properties were characterized using a combination of techniques. The film surface morphology was assessed using a Zeiss 1540 XB scanning electron microscope (SEM) operated at 20 kV. The surface topography and root-meansquare (RMS) roughness of the films were characterized by atomic force microscopy (AFM) measurements using a Dimension Icon Bruker system in a non-contact mode. The crystalline structure of the AlN films was investigated through for $\theta - 2\theta$ scans and rocking curve measurements using a Bruker (D8 Discover Model) x-ray diffractometer with high-intensity $Cu - K\alpha$ radiation ($\lambda = 1.5406$ Å). Micro-Raman measurements were carried out at room temperature using a backscattering configuration. A Labram-800 Raman spectrometer equipped with a nitrogen-cooled charge-coupled device (CCD) was used to record the Raman spectra. A He–Ne laser of wavelength 632.8 was used at a constant power of 1.3mW as the excitation source and a 50× microscope objective was used to focus the laser beam to a spot diameter of about $3\mu m$ on the sample surface.

The quantities of O, H, and C present in the AlN samples were depth-profiled by elastic recoil detection by time-of-flight (ERD-TOF) analysis [131] using a Co 40 MeV ion beam incident at 15° from the surface. The recoils are detected at 30° with respect to the beam axis, except H where it is at 46° through a beam-absorbing foil. The energy spectra were converted to elemental depth profiles using Allegria software [133].

The photoluminescence (PL) spectra were obtained at room temperature using a 1 m-spectrometer (SPEX model) equipped with a cooled photomultiplier tube (Hamamatsu R2658 model). A 266 nm pulsed UV laser source providing 8mW was used as an excitation source where the excitation beam was focused onto the sample surface on a spot diameter of about $200\mu m$. The laser beam was nearly perpendicular to the c-plane surface of the AlN films, and the PL signals were recorded using a conventional lock-in technique. Photoluminescent excitation (PLE) spectra were obtained using a 200-W Xenon lamp connected to a monochromator (Princeton Instrument SP-2300i). A second monochromator and a silicon photodiode were used for the detection of photons reemitted by the samples at specific wavelengths.

4.4 Results and Discussions

4.4.1 Structural Characterization

Figure. 4.2 shows the XRD spectra $\theta - 2\theta$ of the as-deposited AlN films Zr-implanted and after their annealing under different gaseous atmosphere at 1050 $^{\circ}C$ for 1 h. The as-deposited film presents features at 36° and 76.3° corresponding to the (0002) and (0004) AlN diffraction peaks [160] For the Zr-implanted film (Zr/AlN), these peaks are shifted to lower diffraction angles

while they return almost to their original positions after annealing. The shift in the diffraction peaks is attributed to a change in the strain amount in the AlN layer as a result of implantation and decreases significantly upon thermal annealing. The c-lattice parameter's values can be determined from the Bragg's law and the relationship between the distance separating the (000l) atomic planes and parameter c. The strain amount in the AlN films can be determined using the expression $\frac{\Delta c}{c} = \frac{c - c_{Bulk}}{c_{Bulk}}$, where $c_{bulk} = 4.980$ Å [161] is the c-lattice parameter of the bulk AlN material. The values of the c-lattice parameters and the strain amount in the different AlN layers, extracted from the diffraction patterns of Figure.4.2 are given in Table.6.1.

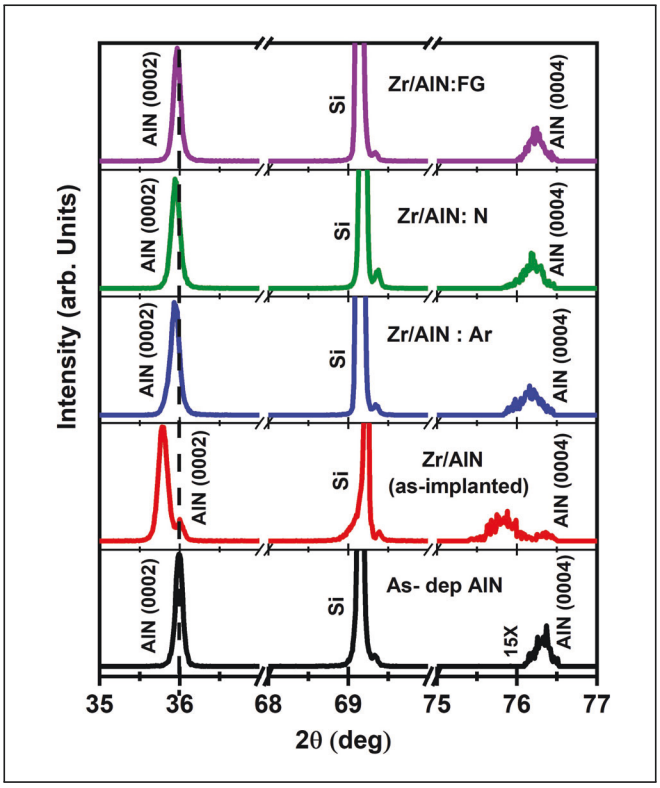

Figure 4.2 $\theta - 2\theta$ XRD patterns of the AlN films before and after Zr implantation and annealing under various atmospheres. The dashed line shows the position of the (0002) peak for the as-deposited AlN film. A peak related to the Si substrate is also shown.

For the as-deposited film, since no other peaks are observed in the XRD pattern, we conclude that the AlN polycrystalline film is purely c-axis oriented. For the sputtered films, the intrinsic defects, lattice or domain mismatch, and different thermal expansion coefficients are the three main sources of residual stress. However, as reported by Zhang et al., the large lattice mismatch (42.7%) between AlN films and the Si (001) substrate is the main contribution for the internal stress in the formed film [162]. Partial strain relaxation in the AlN layer is usually realized by the generation of interface steps and dislocations at the AlN/Si interface [163]. XRD measurements

Sample	c (A°)	Strain(%)	Raman E_2(high) peak position (cm^{-1})	Raman E_2(high) peak width (cm^{-1})	Annealing atmosphere
As-dep AlN	4.984	0.08	659.5	16	...
Zr/AlN (as-implant)	5.024	0.88	662.0	40	...
Zr:AlN/ Ar	4.992	0.24	661.9	17	Argon
Zr:AlN/ N	4.992	0.24	661.5	17	Nitrogen
Zr:AlN/ FG	4.985	0.10	661.0	16	Forming gas

Table 4.1 Lattice parameter, c-axis strain and, Raman $E_2(high)$ peak position, and peak width for different AlN films.

show that the residual amount of strain along the c-axis of this film is about 0.08%.

For the as-implanted film (Zr/AlN), the amount of strain induced in the c-axis direction reaches a value of 0.88%. A similar behavior, resulting from implantation induced damage, has been observed for ion-implanted GaN films [164]. The low intensity peaks observed at 36° and 76.3°, corresponding to the diffraction peaks of the as-deposited film, indicate that a small fraction of the film retains its structural properties even after ion implantation. For post-implantation annealed samples, the strain along the c-axis slightly depends on the thermal annealing conditions with values ranging from 0.10% to 0.24%. The (0002) and (0004) diffraction peaks are narrower than those of the Zr-implanted sample but wider than those of the as-deposited films. This behavior indicates that the crystalline quality of the film is partially restored after the thermal annealing treatment. The influence of the annealing gas atmosphere on the width (FWHM) of the XRD peaks is best illustrated using $\omega - scans$.

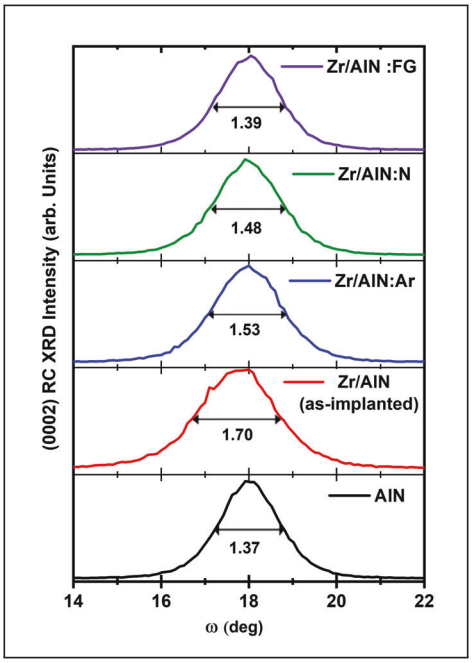

Figure 4.3 (0002) XRD rocking curves of the annealed AlN films using different gas atmospheres (Ar, N_2, and FG). The rocking curve of the as-deposited film is shown for comparison.

The XRD rocking curves of the AlN films annealed under Ar, N_2, and FG are shown in Figure.4.3 for a detector position centered on the AlN (0002) peak. The rocking curve of the as-deposited film is also shown for comparison. The values of the full width at half maximum (FWHM) of these peaks are also indicated in Figure.4.3 The broadening of the XRD peaks results from both size and strain fluctuations in the various AlN crystallites forming the film and amorphous zones in the as-implanted sample. The results show that thermal annealing performed under a forming gas atmosphere is the most effective treatment to restore the crystalline quality of the implanted film.

Figure. 4.4 illustrates the Raman spectra of the annealed AlN films using different gas atmosphere (FG, N_2, and Ar). The Raman spectra of the as-deposited and the as-implanted AlN films are shown for comparison. The laser excitation power of 1.3mW is low enough to avoid sample heating. The spectra can be reproduced by a sum of the three broadened peaks, corresponding to the active Raman vibration modes of the wurtzite structure of the AlN crystal: namely, the $A_1(TO)$, $E_2(high)$, and $E_1(TO)$ modes [91]. There are different broadening mechanisms already observed for crystalline AlN and the thin film of AlN nanocrystallites. These include (i) inhomogeneous broadening mechanisms due to strain fluctuations in the layer, [165] (ii) asymmetric line shape features caused by crystallite size effects on the $q \neq 0$ allowed modes and on the phonon dispersion relation, [166, 167] and (iii) homogeneous broadening mechanisms

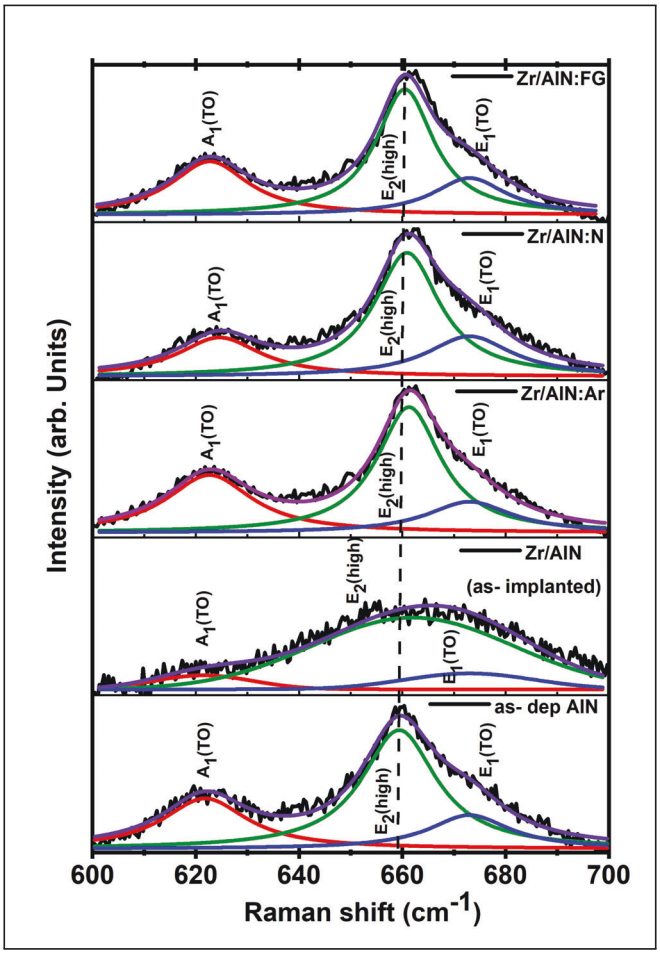

Figure 4.4 Raman spectra of the annealed AlN films using different gas atmospheres (Ar, N_2, and FG). The Raman spectra of the as-deposited and the as-implanted AlN films are shown for comparison. The dashed line shows the position of the $E_2(high)$ vibrational mode for the as-deposited film.

related to the finite phonon lifetime related to the phonon interaction with the crystallite boundaries [168, 169] Different fit functions (Gaussian, Lorentzian, or Voigt) have been used in the literature, [162,164,165,170] but since we are interested in the effect of the fabrication process (ion implantation + annealing) on the position of different allowed Raman modes and their related peak linewidths, we have simplified the analysis by using a sum of Lorentzian functions for each sample's spectrum, except for the Zr/ AlN sample that shows a clear Gaussian spectral line shape. The positions of these peaks are compatible with reported values for the w-AlN crystal [171–173]. For the as-implanted sample, heavy ion implantation in covalently bond materials usually results in the formation of amorphous zones featuring wider distribution of bond angle and interatomic distances than in the crystal that lifts the selection rules and results in much broader Raman peaks [174] as observed in Figure. 4.4 ,and Table. 6.1.

For the annealed samples, the width of the main Raman peak, associated with the $E_2(high)$ mode, comes back to its initial value in the as-deposited film. This is consistent with restored crystalline quality for the samples annealed in Ar, N, and FG atmosphere. This peak is also slightly shifted toward higher frequencies, compared to that of the as-deposited sample. The observed shifts are about 2.4, 1.9, and $2cm^1$ for samples annealed under an atmosphere of Ar, N_2, and FG, respectively. These Raman shifts are consistent with the amount of residual strain values in these films, deduced from the XRD measurements.

Figure.4.5 shows the ERD-TOF depth profiles of O, H, and C elemental species for the different AlN films. According to the lattice parameters we found by XRD and knowing their composition, the density of our films is $9.5 \times 10^{22} atom/cm^3$. Hence, the depth scale in these graphs corresponds approximately to nanometers. It is worth pointing out that the depth profiles cover only about $1/10$ of the film thickness near the surface. The C content is below 0.4% in all films and extends through the layer. It remains about the same for all samples. These are indications that it was introduced during the deposition process, probably as a result of low levels of organic molecules contamination in the deposition chamber. However, there is no excess C peak on the surface of the films, so post-treatments do not introduce additional C contamination. The H content is below 0.6% for all films, except for the film annealed under FG atmosphere, where a constant value of $\sim$ 0.9% is reached. Hydrogen typically favors the passivation of dangling bonds.

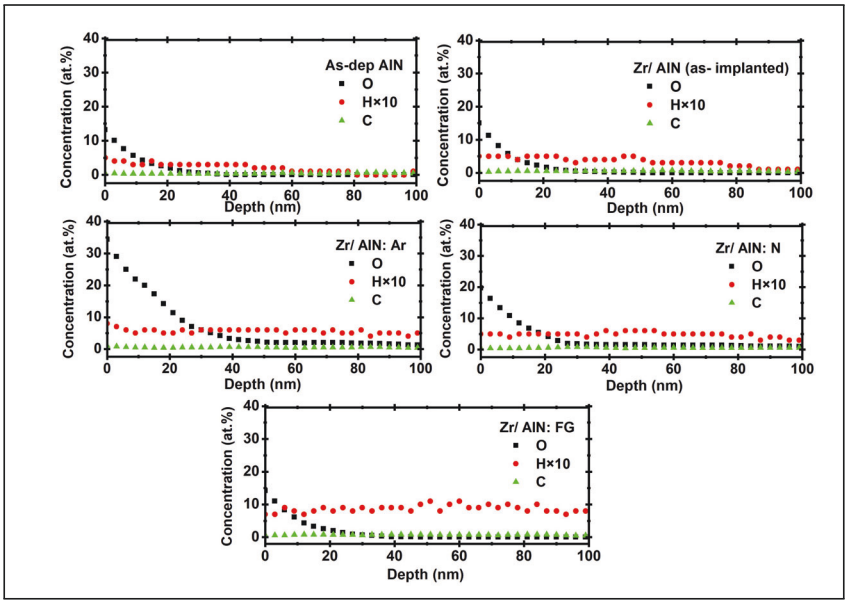

Figure 4.5 ERD-TOF depth profiles of O, H, and C elemental species for the different AlN films.

All films present an O content near the surface, which extends about $20 \times 10^{16} atom/cm^2$ in

depth, which corresponds to 20 nm. For the as-deposited film, the O content reaches about 13% at this free surface. Given the nanostructure of the films (see below), the incident ions hit the surface at various angles during the ERD-TOF measurement, resulting in a broadening of surface peaks. This depth profile is, therefore, compatible with the formation of a native aluminum oxide Al_2O_3 on the surface of the film, which is typically up to 10 nm thick for pure Al. Despite the low oxygen content in the furnace, thermal annealing under Ar or N_2 atmosphere promotes the incorporation of oxygen at the surface and in the AlN film, in which case it is detectable at $\sim$ 1% levels at depth of up to 150–200 nm in these films. While inherently quantitative, ERD-TOF sensitivity is limited to $\sim$ 0.1%. Some O contamination is probably present deeper in the sample given its high reactivity to Al. It is interesting to note that the O profile for the annealed film under FG atmosphere is almost identical to that of the as-deposited and as-implanted films. It, thus, seems that the H passivation of the dangling bonds limits the incorporation or diffusion of O in the film. According to our interpretation, this surface passivation phenomenon can also influence the residual strain in the film. Indeed, limiting the oxygen content in the AlN film during thermal annealing should promote the transfer of Zr interstitials into substitutional sites (Zr_{Al}) and thus reduce the internal strain, consistent with the micro-Raman and XRD results. Otherwise, the formation of ($V_{Al} - O_N$) defect complexes is favored over substitutional (Zr_{Al}) defects as predicted by density functional theory (DFT) calculations [24, 26, 27].

Figure. 4.6 shows the SEM and AFM topographical images of the different AlN films. The morphology of the as-deposited film was quite uniform and dense with a mean surface grain diameter of 41 nm and an RMS surface roughness of 1.5 nm. The ion implantation process alone does not noticeably alter the film morphology. Larger and relatively flat polycrystalline flakes (grain size > 59 nm and RMS surface roughness of $\sim$ 0.91 nm) are found on the surface of the films annealed under an atmosphere of Ar and N.

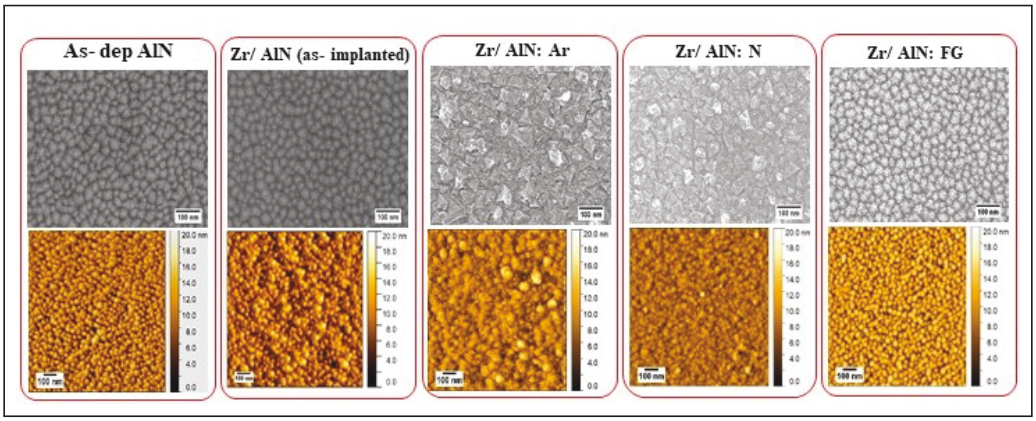

Figure 4.6 SEM micrographs (top) and AFM images (bottom) of the different AlN films.

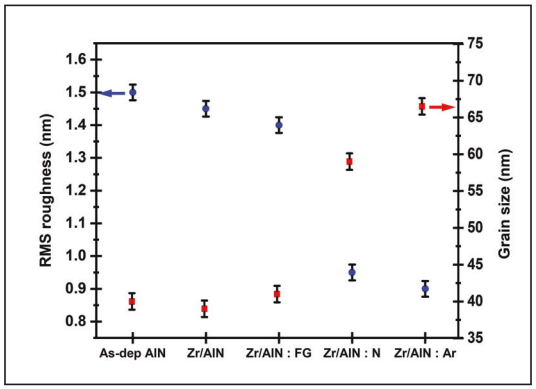

Figure 4.7 Summary of the statistical values of surface roughness and grain size extracted from the analysis of the SEM and AFM images of Figure.4.6

A summary of the statistical values of RMS surface roughness and grain size is given in Figure.4.7 for all samples. The reorganization of atoms on the film surface is governed by the thermal activation process. Higher number of dangling bonds help diffusion and reorganization of the atoms on the surface of these films, resulting in larger grains. For the film annealed under the FG atmosphere, the H-passivation of these bonds hampers these mechanisms and helps preserve the as-deposited structure.

4.4.2 Optical Characterization

The influence of ion implantation and thermal annealing process on the optical properties of AlN thin films was investigated using PL and PLE spectroscopies. Figure.4.8 shows the PL spectra of the different AlN films, except for the as-implanted film that shows a very weak PL signal due to amorphization and the presence of a large density of non-radiative recombination centers. Spectra of Figure.4.8 show the presence of several emission bands in the visible range between 420 nm and 770 nm. The different spectra can be reproduced using a sum of up to five Gaussian-like emission bands centered around 1.7 eV, 2 eV, 2.2 eV, 2.5 eV, and 2.8 eV. The inset in Figure.4.8 shows the best fitting curve of the Zr/AlN:Ar PL spectrum, obtained using a sum of five Gaussian-like emission bands.

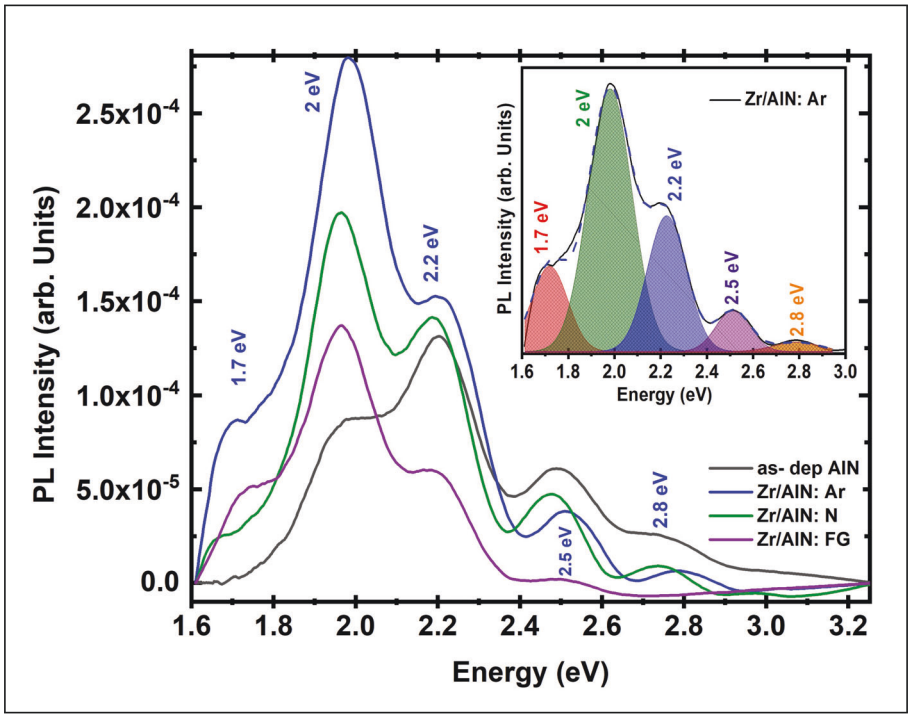

Figure 4.8 room-temperature PL spectra of the different AlN thin films. The inset shows the best fitting curve of the PL spectrum of the Zr/AlN:Ar film, obtained using a sum of five Gaussian-like emission bands.

Further discussion of the influence of the fabrication process on the different defects that may exist in our AlN films has to be given before interpreting the different PL features. Heavy ion bombardment creates a high density of amorphous zones and point defect clusters. Upon annealing, this usually results in a zoo of point defect complexes with complicated annealing dynamics [175]. In addition to the point defects, the O impurities incorporated during the deposition process mainly exist in the form of substitutional atom on N sites O_N. ERD-TOF results indicate non-negligible amount of C through the layers. However, according to the literatures, the C-related levels are in the 4–6 eV range, which is far from the area of our PL study [93–95]. Therefore, we do not study the C-related defects in this paper. Also, as a result of implantation, Zr atoms can substitute other atoms of the lattice structure Zr_{Al}, acting as point defects and/or defect complexes such as vacancy-interstitial aggregates. The non-homogeneous distribution of these defect complexes may result in a large fluctuation of the internal strain in the implanted layer. Thermal annealing promotes the displacement of vacancies and atoms to reduce the overall strain in the film. This can be accomplished in several ways: (i) annihilation of vacancies with Al and N interstitials, (ii) annihilation of vacancies by the transformation of O and Zr interstitials into substitutional defects, (iii) formation of complex vacancy-substitutional impurity such as $V_{Al}-O_N$ complexes, and (iv) dissociation of vacancies–interstitials aggregates.

Up to date, the energies of formation and dissociation of these point defects and defect complexes are still poorly known in AlN. Meanwhile, ab initio calculations using the DFT method can nevertheless be used to predict the existence of the defects most likely to form. These theoretical studies [24, 26, 27] notably predict a lower formation energy for the $V_{Al} - O_N$ complex compared to that of the Zr_{Al} substitutional defect. This may help understand the influence of the annealing conditions on the relative intensity of different emission bands, as will be seen later.

Theoretical and experimental results showed that V_N and V_{Al} point defects have shallow energy levels below the conduction band and above the valence band extrema, respectively [96, 176].Oxygen substitutional defect O_N and their related defect complexes, such as $V_{Al} - O_N$, have also been reported as an important defect in AlN [90, 91, 177–179]. Based on these studies and other DFT calculations [24, 26, 27, 180], the suggested origin of the different emission bands is given in Table.6.2 showing also the optical transition schemes involving these most common defects. The experimental evidence and identification of most of the absorption energy levels and some of the emission energy levels have not been yet experimentally presented. The emission band appearing around 2.8 eV can be attributed to transitions from the V_{Al} levels to the valence band (VB) [74, 180]. The AlN bandgap energy is sensitive to the internal strain, as reported by Seo et al. [24]. This is most likely the origin of the slight shift of the emission band at 2.8 eV, observed from one sample to the other in accordance with the strain variation revealed by XRD and Raman measurements. The second higher energy emission band, centered at $\sim$ 2.5 eV, is associated with transitions from the $V_{Al} - O_N$ levels to the VB [86]. There is also a slight shift in this band, from one sample to another, which can still be associated with changes in the internal strain in the films. The emission bands at 2.2 eV and around 2.0 eV can be associated to the $V_N \rightarrow (V_{Al}^{3-} - 3O_N)$ transitions [181] and to emission related to $V_{Al} - O_N$ energy levels [182] respectively. These four emission bands, between 1.9 eV and 2.9 eV, are present in the spectra of all samples, except the 2.8 eV band that seems to quench upon annealing under a forming gas atmosphere. Indeed, annealing under a forming gas might promote the incorporation of Zr atoms into substitutional sites Zr_{Al} that reduce the number of V_{Al} sites resulting in a significant decrease in corresponding emission intensity in the Zr/AlN :FG sample.

The most striking results are the increase in the intensity of the emission band peaked at 2 eV and the appearance of a new emission band at 1.7 eV after the post-implantation annealing treatment. The enhancement of the PL intensity at 2 eV is explained by an increase in the density of the $V_{Al} - O_N$ defect complexes, while the appearance of a new emission band at

Suggested transitions	**Absorption/ Emission**	**Energy (eV) (previous works)**	Reference	**Energy (eV) Expt. (this works)**
$VB \rightarrow V_{Al}$	Absorption	3.4	[180]	3.2
$(V_{Al}-O_N)^{2-}+V_N^{+} \rightarrow (V_{Al}-O_N)^{-}+V_N^{0}$	Absorption	3.03	[180]	3.0
$(V_{Al}^{3-}-V_N^{+}) \rightarrow (V_{Al}^{2-}-V_N^{0})$	Absorption	2.49	[180]	2.7
$(Zr_{Al}-V_N)^0$	Absorption	2.83	[27]	2.6
$V_{Al} \rightarrow VB$	Emission	2.77 , 2.78	[74, 180]	2.8
$(V_{Al}-O_N) \rightarrow VB$	Emission	2.53	[86]	2.5
$V_N \rightarrow (V_{Al}-O_N)$	Emission	2.16	[181]	2.2
$(V_{Al}-O_N)$	Emission	2.05	[182]	2.0
$(Zr_{Al}-V_N)^0$	Emission	1.91	[27]	1.7

Table 4.2 Suggested transitions for absorption and emission bands seen between 1.7 and 3.25 eV.

1.7 eV would be due to the formation of $Zr_{Al}-V_N$ defect complexes. However, the transition energy associated with later defect complexes in strain-free AlN has been predicted by Varley et al [27] around 1.9 eV. The position of our emission band at 1.7 eV seems to be redshifted by the residual strain in the AlN film. Optical experiments in the presence of external stress will be required to confirm this interpretation. In comparison with other samples, Zr/AlN:Ar shows the most intense and resolved emission peaks. Therefore, we will focus on this sample for a deeper analysis on the origin of transition energy bymPLE. Absorption spectroscopy measurements are very useful for confronting experimental results with theoretical predictions. Figure.4.9 shows the PLE spectra of the Zr/AlN:Ar film, detected at the energy position of the main emission bands at 1.7 eV, 2 eV, 2.2 eV, and 2.5 eV.

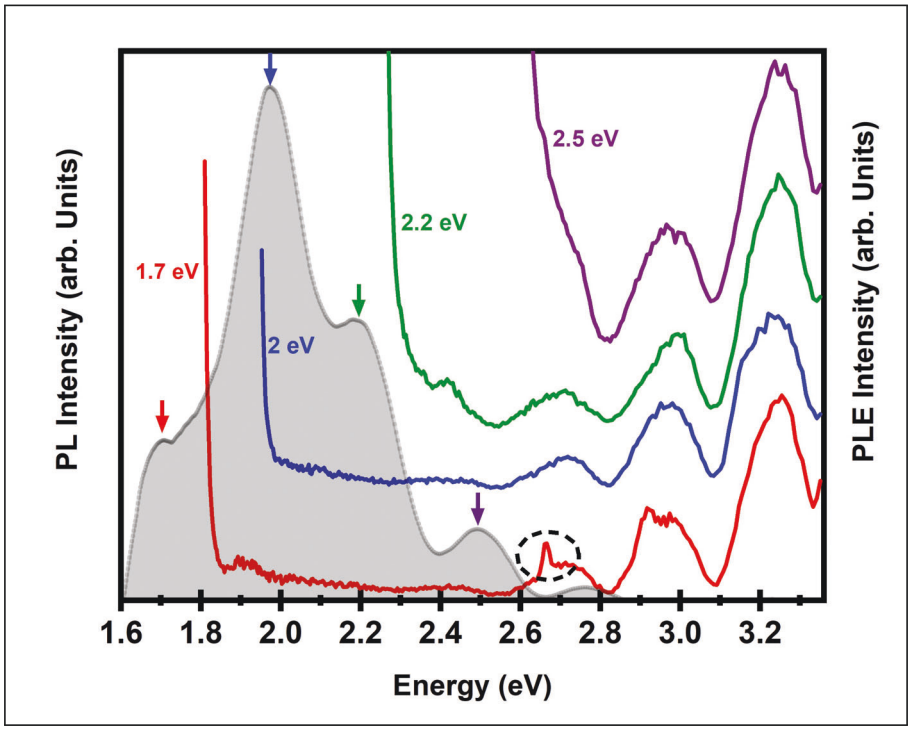

Figure 4.9 Photoluminescence spectrum (shaded surface) and photoluminescence excitation spectra (colored solid lines) of the Zr-implanted and Ar-annealed AlN film. The PL spectrum is obtained using a laser source at 266 nm and the PLE spectra are obtained using a wavelength tunable source and detection at specific energies, indicated by colored arrows on the PL spectrum.

The three emission bands at higher energy appear to be correlated with three main absorption bands peaked at 2.7 eV, 3.0 eV, and 3.2 eV. Hybrid functional calculation59 predicted that the isolated aluminum vacancies are responsible for the absorption band around 3.4 eV. The observed absorption band at 3.2 eV might be related to this $VB \rightarrow V_{Al}$ optical transition. For the 3 eV absorption band, it might originate from the charge transfer between a $(V_{Al}^{3-} - O_N)^{2-}$ complex defect and V_N^+ in its vicinity, as predicted by DFT calculations.59 The absorption band at 2.5 eV is most likely related to optical transitions involving V_{Al} in a 3 charge state and V_N in a + charge state ($V_{Al}^{3-} + V_N^+ \rightarrow V_{Al}^{2-} + V_N^0$) [180]. The slight shift of $\sim$ 200 meV observed between experimental and theoretical predictions might originate from the residual strain in the AlN films. Finally, the PLE spectrum detected at the 1.7 eV emission band shows an additional narrow absorption band at 2.6 eV. This narrow band is very likely related to $(Zr_{Al} - V_N)^0$ defects [27], which has been theoretically expected to have a S = 1 spin character. There has not been a previous experimental report for Zr-related defects in AlN. However, further experiment is necessary to investigate the spin character of these defects.

4.5 Conclusion

In summary, we have investigated the effect of Zr implantation and thermal annealing under different gas atmospheres on the structural and optical properties of polycrystalline AlN films. Results show that, after annealing under Ar and N atmosphere, samples show a higher amount of strain in comparison with the as-deposited AlN. These results could be interesting for strain engineering of AlN. Moreover, after annealing in the forming gas atmosphere, the results represent the nearly full implantation damage recovery of sample. Different emission and absorption bands related to the complex defects are identified by PL and PLE. The results reveal that the Zr implantation followed by thermal annealing results in formation of a new defect in AlN with emission and absorption energy at 1.7 eV and 2.6 eV respectively. Comparing with the results from first-principles calculations based on density functional theory (DFT), these energies could be assigned to $(Zr_{Al}-V_N)^0$ defect levels. Proton implantation in Zr-doped AlN films could also be considered in our future work as an alternative method to generate optically active Zr-vacancy pairs while minimizing the density of non-radiative recombination centers in the host crystal. This technique and such defects are potentially interesting for quantum technology applications.

4.6 Acknowledgments

This work was financed by the National Sciences and Engineering Council of Canada (NSERC), the Canada Foundation for Innovation (CFI), the Fonds de recherche du Québec—Nature et technologies (FRQNT), and the Canada First Research Excellence Fund (CFREF). We acknowledge Teledyne Dalsa for their expertise and for providing us with high-quality AlN films. The authors would like to thank also M. Dion for his support with XRD measurements, P. L. Karsenti for his support with PLE measurements, G. Laliberté for his technical support in the PL laboratory, and L. Godbout for his help with the maintenance and operation of the ion accelerator

CHAPTER 5 Optical Characterization of $(Zr_{Al} - V_N)^0$ Point Defects in Zr-implanted Polycrystalline AlN Films

This chapter provides a summary of the comprehensive optical studies conducted on $(Zr_{Al}-V_N)^0$ point defects in AlN films. The results of first-principles calculations based on density functional theory (DFT) have already indicated that these defects can be used as qubit defects for quantum applications [24, 26, 27]. However, to effectively leverage the potential of these defects, it is essential to gain control over their formation and fully investigate their structural and optical properties.

Chapter.4 presents the effect of implantation/annealing treatment on the strain in AlN films and establishes suitable protocols for creating $(Zr_{Al} - V_N)^0$ point defects. This chapter is dedicated to exploring the optical properties of these defects and comparing the findings with theoretical calculations. By understanding the optical properties of these defects, we can further advance their application in quantum technologies.

5.1 Experimental Details

The thin film samples used in this study were 1 μm thick, wurtzite-phase AlN films grown via reactive DC magnetron sputtering on highly-doped silicon substrates oriented along the c-axis, as described in Chapter.4. To introduce $(Zr_{Al}-V_N)^0$ point defects, the samples were ion-implanted with Zr atoms at a fluence of 10^{14} ions/cm^2 and then annealed in a FG environment to prevent surface oxidation. Different annealing treatments were tested with temperatures ranging from 500°C to 1050°C and annealing times from 30 minutes to 1 hour. Previous results showed almost full damage recovery for samples annealed at 1050°C in FG environment.

To characterize the samples, a home-made PL imaging setup with a 532 nm laser and a 60X microscope objective was used. The PL spectrum was filtered using a 560 nm long-pass filter and detected with a monochromator (Horiba Triax 320) equipped with a nitrogen-cooled CCD camera. Time-resolved photoluminescence measurements were also conducted using an avalanche photodiode for signal detection and a time-correlated single-photon counting unit coupled to a pulsed laser diode source at 532 nm. PL measurements showed that AlN samples annealed at temperatures above 900°C had a uniform PL background but no detectable isolated emitters. However, increasing the annealing temperature to 1050°C reduced the PL background and allowed for the detection of isolated emitters, which were optically investigated in this

chapter.

5.2 Spectral Analysis of $(Zr_{Al} - V_N)^0$ Point Defect

Initially, we directed the laser beam onto the sample's surface and collected the PL spectra at different locations on the sample to identify bright spots displaying a strong ZPL intensity. The low-temperature PL spectra of the emitters at 4 K are depicted in Figure.5.1. Our investigations uncovered a prominent ZPL peak at 685.6 nm (1.808 eV) accompanied by a phonon side band shifted towards the red, centered around 700 nm (1.77 eV). A Gaussian function was used to fit the ZPL, and the resulting FWHM was approximately 1.7 nm, which is wider than that observed previously for AlN emitters [4]. This broadening may be attributed to a group of emitters clustered in the bright spots.

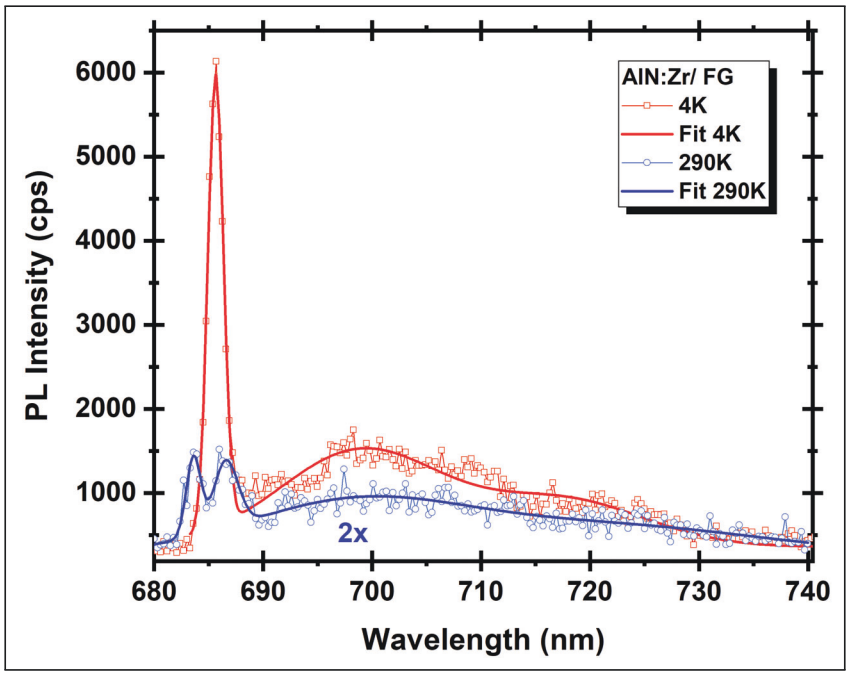

Figure 5.1 The figure displays the temperature-dependent photoluminescence (PL) spectra of a bright spot, with the red curve representing measurements at 4 K and the blue curve representing measurements at 290 K. At room temperature, a second peak at a shorter wavelength is observed in addition to the zero-phonon line (ZPL) peak.

Accordingly, the detection wavelength was set to the central wavelength of the ZPL (685 nm), and a PL map of the sample was generated by scanning at different positions on the sample. Figure 5.2 shows the low-temperature (4 K) PL scans of the AlN samples after annealing at 1050°C, taken at various positions. Initially, large-scale PL maps were acquired over areas of

$100 \times 100\ \mu m^2$ (Figure 5.2(a)) and $1000 \times 1000\ \mu m^2$ (Figure 5.2(b)). Our results revealed a dark background with micro-sized bright spots, which we attribute to point defects in the AlN film. The background counts were likely due to substrate fluorescence, laser reflections, and detector dark counts. These bright spots were distributed throughout the AlN film, with varying emission intensities that may be related to the position of emitters in the AlN layer. To investigate these bright spots more closely, we focused on the mapping area around the emitters. Figure 5.2(d-f) shows zoomed-in maps of Figures 5.2(a-c), respectively. The ratio of the PL intensity of emitters to the background intensity at the emitter's wavelength varied from 12 to 150, depending on the emitter's PL intensity. The diameter of the bright spots ranged from 5 μm to 30 μm, much larger than what has been observed for single AlN emitters [4]. These results are consistent with the broadening of the ZPL and suggest the presence of a cluster of defects in the bright spots.

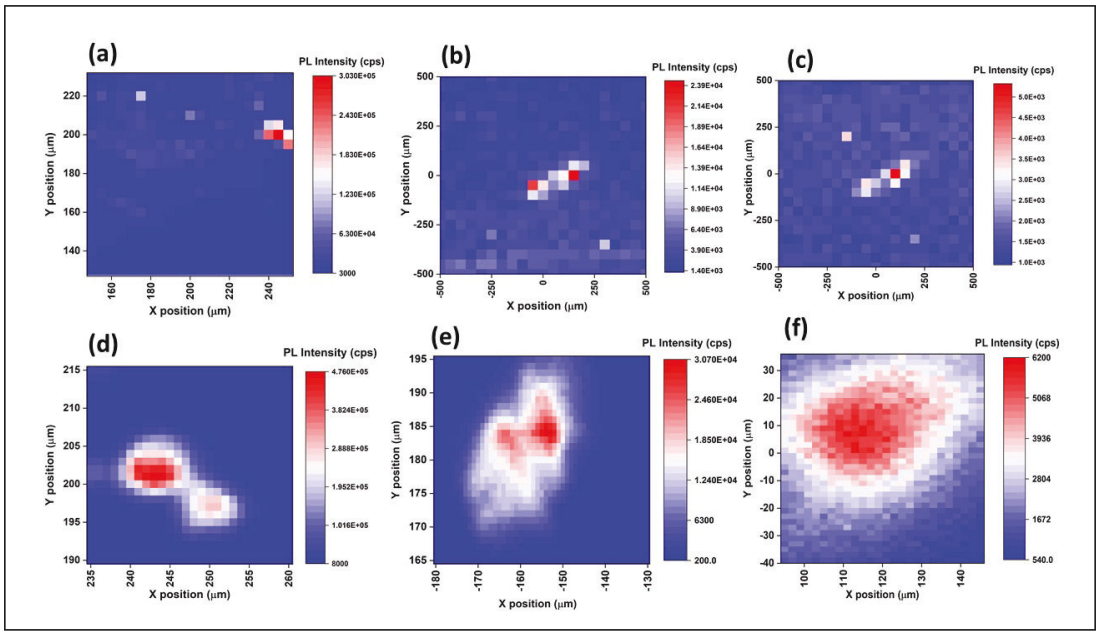

Figure 5.2 Rewritten: The figure shows the mapping of point-like emitters in AlN for two different areas: $100 \times 100\ \mu m^2$ (a) and $1000 \times 1000\ \mu m^2$ (b and c). Figures (d-f) provide a closer view of the PL map around the bright spots.

Previous research [183] has attributed the 700 nm peak to emission from states related to the $(Zr_{Al}-V_N)^0$ defect complexes. This suggests that the ZPL peak at 685.6 nm could also be related to the same point defects. However, predictions by Varley et al. [27] for the ZPL and phonon sideband associated with the $(Zr_{Al}-V_N)^0$ complex defects in strain-free AlN are at 2.3 eV and 1.9 eV, respectively. In contrast, the observed ZPL and phonon sideband in our study are at 1.85 eV and 1.77 eV, respectively, indicating a redshift. DFT calculations have demonstrated

that uniaxial and biaxial strain in AlN can affect the band gap and position of defect energy levels [24], and thus the redshift in the position of the ZPL and phonon sidebands may be attributed to the residual strain in the Zr-implanted AlN film.

Figure 5.1 presents the optical emission spectra of the $(Zr_{Al} - V_N)^0$ complex defects at room temperature, denoted by the curve labeled as 290 K. The spectra show two weak peaks at 684 nm and 687 nm, and a broad emission band ranging from approximately 680 to 740 nm.

PL spectra were acquired at various temperatures ranging from 4 K to 295 K to investigate the recombination mechanism of the luminescent defect states, as per our experimental methodology. The resulting PL spectra, depicted in Figure.5.3, illustrate that the intensity of the ZPL declines as the temperature rises, while the maximum shifts towards higher wavelengths. Moreover, a new emission peak arises at shorter wavelengths for temperatures exceeding 30 K. Peak A and peak B denote the ZPL and second peak, respectively. Peak B's intensity gradually rises with temperature, reaching a maximum before dramatically declining above 130 K. In contrast, Peak A's intensity only diminishes with temperature. Furthermore, these peaks undergo redshift and broadening with increasing temperature, as demonstrated in Figure.5.3(b) and (c).

The temperature dependence of the linewidth of the luminescent defect in AlN has been observed and compared to that of SPEs in h-BN [16]. The broadening of linewidth with temperature has been attributed to the mixing of vibrational states of the localized defect due to electron-acoustic phonon coupling. While the model used in [16] was not applicable to defects in AlN due to unknown parameters, it was observed that the linewidth broadening of our defect complexes in AlN was about 0.9 nm and 0.58 nm for peak A and peak B, respectively, from 4K to 290 K, while for SPEs in hBN, this value was about 1.7 nm over the same temperature range. As AlN is a piezoelectric material, it is likely that electron-phonon coupling is responsible for the observed linewidth broadening, but our results indicate that the coupling strength is less significant than that observed for hBN, which is a 2D material known to have strong electron-phonon coupling.

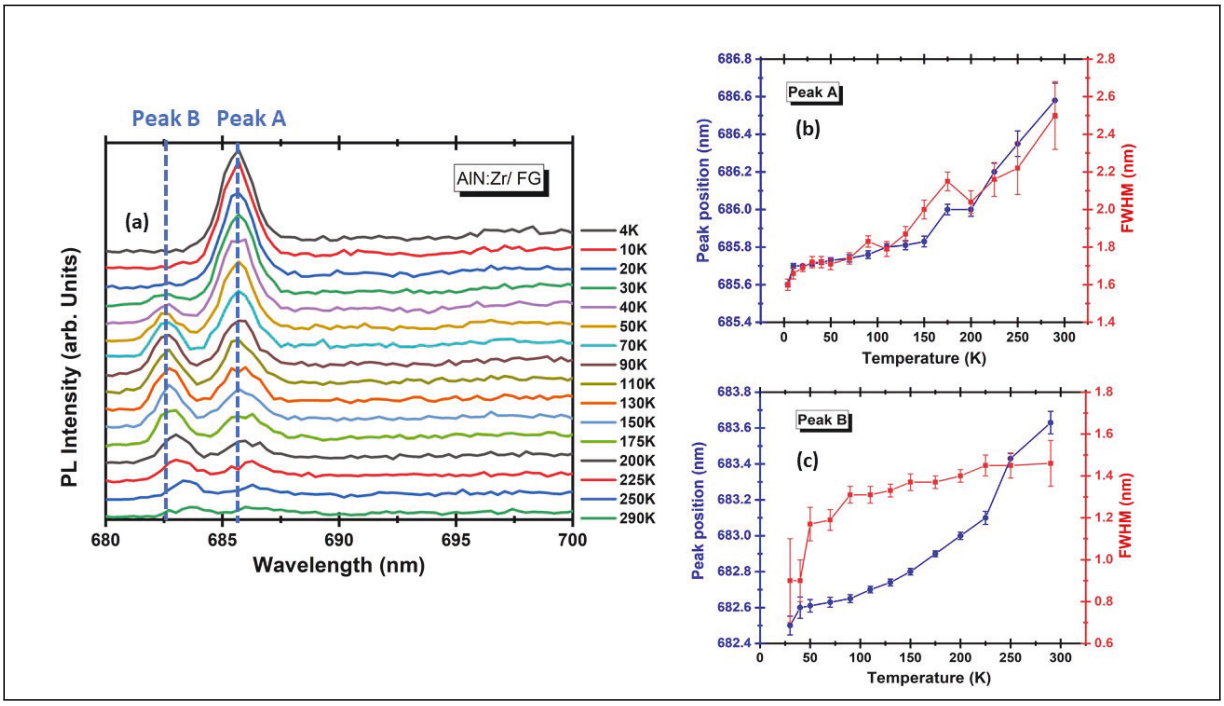

Figure 5.3 (a) Photoluminescence spectra of AlN:Zr/FG film obtained at various temperatures. (b-c) Temperature-dependent variations in the position and linewidth of peak A and peak B.

The photoluminescence of defects in semiconductors typically decreases with increasing temperature due to the opening of non-radiative channels, which is known as positive thermal quenching (PTQ) in PL [184, 185]. We observe PTQ in the PL evolution of peak A, but the PL spectra of peak B behave differently, as shown in Figure.5.3. Anomalous behavior where the PL intensity increases with increasing temperature, known as negative thermal quenching (NTQ), has been observed in various semiconductors [184, 186–190].

To better understand the underlying dynamics responsible for the evolution of the PL peaks, we fit the PL spectra in this wavelength region using a Gaussian function. We extract the PL intensities of these two peaks and plot them as a function of 1/T in Figure.5.4. The multi-level model developed by Shibata [191], which describes both PTQ and NTQ, is often used to analyze PL temperature dependence. This model is given by:

$$I^{PL}(T) = I_0^{PL} \frac{1 + \sum_{q=1}^{n} C_q exp(-E'_q/k_B T)}{1 + \sum_{j=1}^{m} D_j exp(-E_j/k_B T)} \tag{5.1}$$

where I_0^{PL} represents the PL intensity at low temperatures, k_B is the Boltzmann's constant, n is the number of intermediate states with an activation energy of E'_q, and m is the number of nonradiative processes with activation energy E_j. C_q and D_j are the coefficients for the

intermediate and nonradiative processes, respectively. The exponential term in the numerator describes the NTQ process, while the denominator term corresponds to the PTQ process.

For peak A, since there were no indications of the NTQ process, the experimental data were fitted using Eq.5.1 with two nonradiative channels (m=2) and $C_q = 0$, as shown in Figure.5.4. The experimental data for peak B are also shown in Figure.5.4, and the fitting curve corresponds to the model of Eq.5.1 with only one nonradiative channel (m=1) for the PTQ and only one intermediate state (n=1) for the NTQ. The characteristic energies extracted from the fitting procedure are $E_1 \approx 7.9meV$ and $E_2 \approx 71.3meV$ for peak A, and $E'1 \approx 76meV$ and $E1 \approx 85meV$ for peak B.

We propose a possible explanation for our findings based on the recombination dynamics of a discrete set of energy levels. Upon green laser excitation at 532 nm, photogenerated carriers are elevated to the excited states of defects (ES), after which they rapidly relax to the minimum energy of ES. At low temperatures, carriers in ES primarily recombine via photon emission (ZPL) or photon emission with one or more phonons (phonon replica or side-band). As the temperature increases, the phonon side-band becomes more significant.

Peak A exhibits an activation energy of 7.9 meV, equivalent to the energy difference between Peak A (1.808 eV) and Peak B (1.817 eV). Therefore, thermal quenching of Peak A is likely due to carriers depopulating to energy states of Peak B (EB) and an increase in the number of non-radiative (phonon-assisted) transfers. One other intermediate state in the bandgap of AlN occupies the excited state of Peak B, in addition to the excited state of Peak A. Therefore, as Peak A's intensity diminishes, Peak B's intensity begins to increase (NTQ) with a characteristic activation energy of around 76 meV.

However, at higher temperatures (above 140 K), Peak B undergoes PTQ, which may be associated with an increase in non-radiative (phonon-assisted) transfers at those temperatures. As a result, the intensity of Peak B decreases.

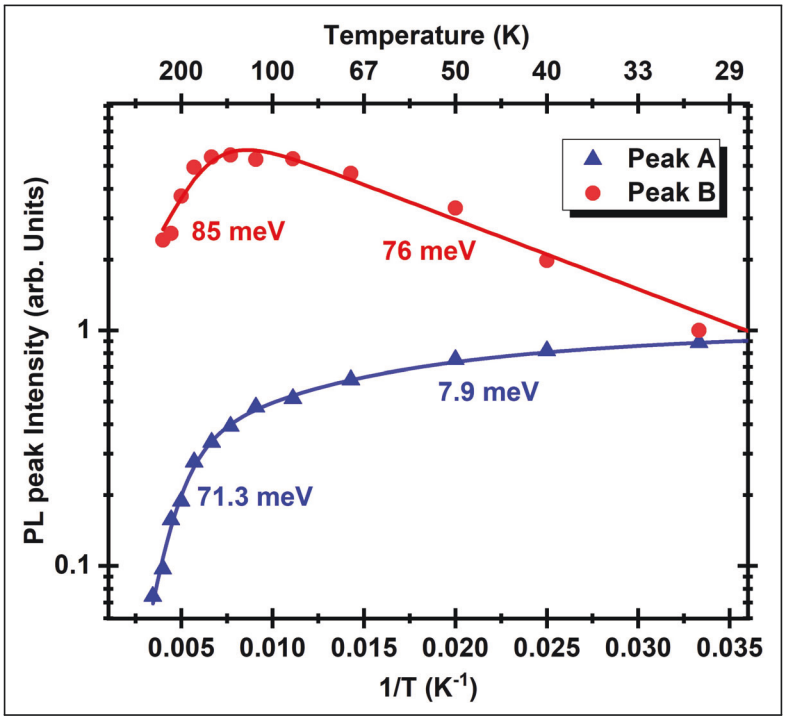

Figure 5.4 PL intensity of peak A and peak B as a function of 1/T. Solid lines are fits to the experimental data using the Eq.5.1

The ability of defects to function as good single-photon emitters is determined by the fraction of photons emitted in the zero-phonon line (ZPL), which is quantified by the Debye-Waller factor (DWF). The DWF is calculated as the ratio of the ZPL PL emission (I_{ZPL}) to the total PL emission (I_{TOT}), which is the sum of the ZPL and phonon-broadened PL (I_{PSB}). We obtain the DWF by separately fitting the ZPL and PSB peaks with Lorentzian functions. At low temperatures (4 K), the DWF is estimated to be $18.5 \pm 2\%$. This high DWF at cryogenic temperatures suggests that these defects could be promising single-photon emitters. However, further measurements of the second-order autocorrelation photon statistics of the defects are necessary to fully assess their potential for quantum emitting applications.

5.3 Photophysical Characterization

The time-resolved PL (TRPL) results of AlN:Zr/FG film are presented in Figure 5.5(a), where the decay lifetime of the TRPL spectra was fitted using a bi-exponential function in the following form [192]:

$$I(t) = A_1 \exp(-t/\tau_1) + A_2 \exp(-t/\tau_2) \tag{5.2}$$

where τ_1 and τ_2 are fast and slow decay times, and A_1 and A_2 are the weighting of the fast and slow components. The fitting results reveal a decay time of $\tau_1 = 0.37 \pm 0.006$ ns and $\tau_2 = 1.37 \pm 0.04$ ns. The slow decay relaxation time is similar to what has been calculated for single emitters in AlN films [2, 4, 25].

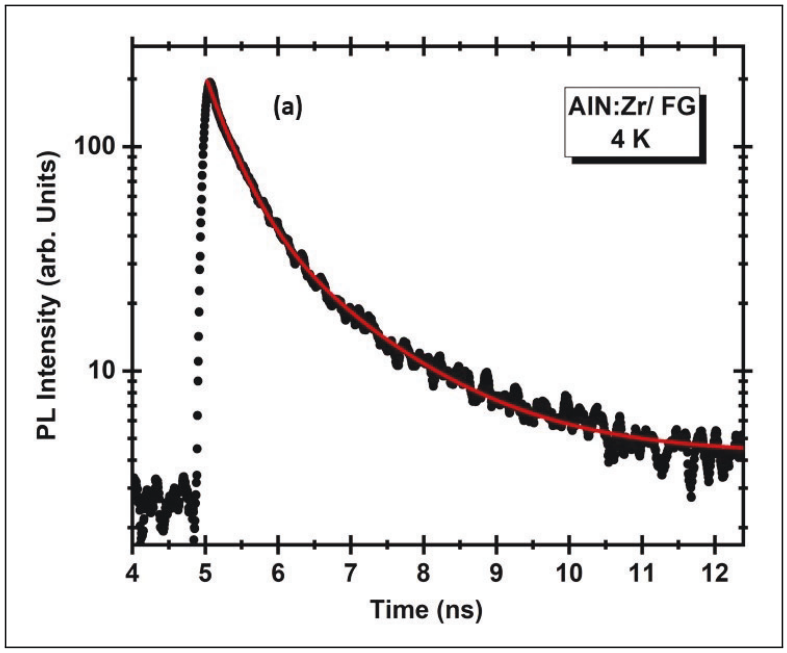

Figure 5.5 Excited state lifetime measurements of ZPL for $(Zr_{Al} - V_N)^0$ defects, fitted with a bi-exponential decay function, showing the fast and slow lifetimes of 0.37 ± 0.006 and 1.37 ± 0.04 ns, respectively.

The emission intensity of $(Zr_{Al} - V_N)^0$ defects is shown in Figure.5.6 as a function of excitation power from a 532 nm cw laser. The data was fitted using the following equation:

$$I = I_\infty \times P/(P + P_{sat}) \tag{5.3}$$

where I_∞ and P_{sat} represent the emission rate and excitation power at saturation, respectively. The fitting results indicate that I_∞ is approximately $2.8 \times 10^4 cps$, and P_{sat} is approximately 2.5 mW. These values suggest that the emission rate of these defects is lower than that observed for other single emitters in AlN film [2, 4, 25], which could pose a challenge for their use as a source for single-photon emission. Nevertheless, if future studies reveal strong antibunching emission from these defects, methods such as passivation, integration of single-photon emitters in cavities or plasmonic structures, and more [193] could potentially enhance the extraction efficiency of photons from these defects.

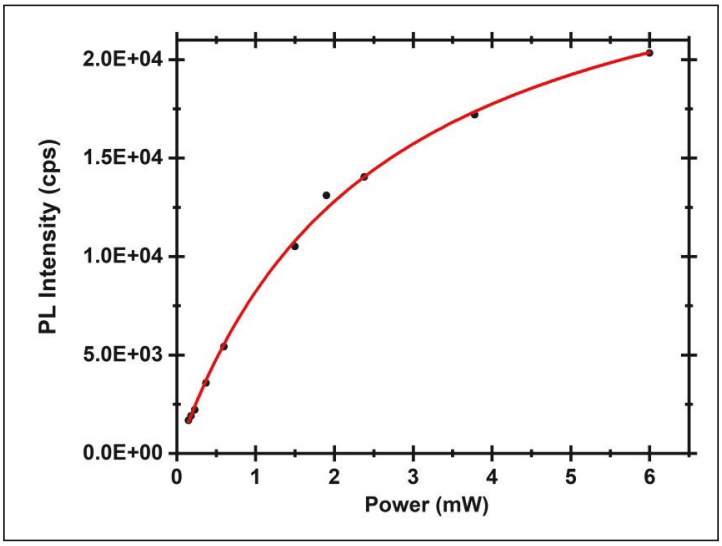

Figure 5.6 PL intensity saturation response of defects reached 2.8×10^4 counts per second at saturation, with a saturation power of 2.5 mW.

5.4 Conclusion

The aim of this study was to investigate the optical properties of AlN:Zr/ FG defects using photoluminescence (PL) spectroscopy. Low-temperature PL mapping with a μPL setup revealed the presence of micro-sized bright spots against a dark background. At cryogenic temperatures, PL measurements showed a zero-phonon line (ZPL) at 685.5 nm, along with a lower energy sideband at around 700 nm. We attribute these peaks to $(Zr_{Al} - V_N)^0$ defects in AlN.

Further investigation using temperature-dependent PL measurements indicated the emergence of a second peak at higher energies at temperatures above 30K. By combining the results from temperature-dependent PL and time-resolved PL (TRPL), we proposed a possible recombination mechanism for $(Zr_{Al} - V_N)^0$ complex defects. Additionally, our results showed a relatively high Debye-Waller factor of around 18.5

However, to fully assess the potential of these defects as single-photon emitters, we recommend conducting an Second-order photon correlation measurement ($g^{(2)}(\tau)$). Overall, this study provides important insights into the optical properties of $(Zr_{Al} - V_N)^0$ defects in AlN and their potential applications in quantum photonics.

CHAPTER 6 Experimental evidence for spin-triplet states in Titanium implanted AlN film: an electron spin resonance study

6.1 Foreword

The previous two chapters have presented the optical results obtained from the AlN films grown on Si substrates. In addition to these optical studies, we also attempted to measure ESR signals in these films in order to study the spin characteristics of defects present in these films. Unfortunately, our results indicate that no ESR signals were detected in these AlN samples, suggesting that the concentration of paramagnetic centers in these films is too low or that the main defects are not paramagnetic.

During our investigations of the various samples processed in this thesis it turned out that ESR signals could be detected on AlN films grown on sapphire and processed by our implantation/annealing process. This chapter presents and discusses the results of this study. Unfortunately, only Ti and H ions were used for the bombardment of these films on sapphire, which limits the scope of this study. It seems that the initial crystalline quality of these films and the amount of inner strain after implantation/annealing are responsible for the generation of these paramagnetic defects in sufficient quantity to be measurable via the ESR spectrometer at our disposal. Further structural characterization is still needed to unravel the mystery related to the absence of ESR signals on our AlN films grown on Si. It would also be interesting to try other more sensitive spin resonance measurement systems in order to carry out further in-depth studies of these AlN films.

Concerning the studies of the optical properties of the AlN films grown on sapphire, we made the choice not to present them in this thesis because the photoluminescence spectra of these samples (excited with a laser beam in the green, at 532 nm) are totally dominated by the emission of the colored centers in sapphire: we do not see any significant difference between the luminescence of the pristine sapphire substrate and that of the AlN films on sapphire.

Abstract Spin-carrying defects found in wide-bandgap semiconductors are promising candidates for the advancement of quantum sensing and quantum information technology. This study presents experimental evidence demonstrating the formation of paramagnetic defects in AlN films after subjecting them to high-energy hydrogen and titanium ion implantation. The amount of local strain in the AlN films was found to be affected by the ion species and implan-

tation process, as revealed by X-ray diffraction and Raman spectroscopy. Furthermore, electron spin resonance spectroscopy identified resonance peaks with g-values higher than that of a free electron (2.0023) for both H-implanted and Ti-implanted AlN films. The origin of these peaks was identified as different types of point defects. In the case of the Ti-implanted film, a half-field resonance peak was also detected and attributed to spin-triplet (S=1). These findings shed light on the electronic spin state of point defects in AlN and offer exciting prospects for their application in quantum devices.

Authors and affiliations

- **Azin Aghdaei:** Ph.D candidate, Université de Sherbrooke, Faculty of science, Physics department, Sherbrooke, Quebec, Canada.
- **Arash Akbari-Sharbaf:** Postdoctoral Fellow at Villanova University, Villanova, Pennsylvania, United States.
- **Martin Chicoine:** Research Associate, Département de Physique, Regroupement québécois sur les matériaux de pointe, Université de Montréal, Montréal, Quebec, Canada.
- **François Schiettekatte:** professor, Département de Physique, Regroupement québécois sur les matériaux de pointe, Université de Montréal, Montréal, Quebec, Canada.
- **Giovanni Fanchini:** Full professour, Western University, London, Ontario, Canada.
- **Denis Morris:** Full professor, Université de Sherbrooke, Faculty of science, Physics department, Sherbrooke, Quebec, Canada.

Status of acceptance: Submitted: 23 August 2022, Accepted: 2 February 2023, Published Online: 1 April 2023.

Journal: Physica B: Condensed Matter, Cite as: Physica B: Condensed Matter (2023): 414708.

Contribution to the document: The presented idea for this study was conceived and the analytical methods were verified by Azin Aghdaei and Denis Morris. Denis Morris supervised the investigation of the spin character of paramagnetic defects in Ti-implanted AlN films and encouraged Azin Aghdaei throughout the research. Azin Aghdaei conducted all the post-annealing treatment, structural characterization, and ESR measurements, developed a Matlab code, and performed ESR simulations using EasySpin software. Additionally, she analyzed the results and took the lead in writing the manuscript. Arash Akbari-Sharbaf supervised the ESR measurements and EasySpin simulations, while Martin Chicoine and François Schiettekatte performed the ion implantation on the AlN films. All authors provided critical feedback and contributed to shaping the research, analysis, and manuscript.

6.2 Introduction

Spin-defects embedded in a wide-bandgap semiconductor host are promising systems for a range of quantum technologies. Recently defects in diamond known as nitrogen-vacancy (NV^{-1}) attracted considerable attention as potential candidates for quantum technology applications [6–8]. The ground state of this colored center in diamond is spin-triplet (S=1) which consists of three sublevels with spin projections of $m_s = 0$, -1, and $+1$, where the $m_s = \pm 1$ sublevels are separated from $m_s = 0$, by the crystal field. The superposition of $m_s = 0$ and $m_s = \pm 1$ sublevels can be utilized as qubit states $\mid 0 >$ and $\mid 1 >$, which are the fundamental building blocks for quantum computers. Moreover, the separation between these sublevels and their dependence on external parameters such as electric and magnetic fields, temperature, and pressure, are the basis for the operation of new quantum sensors.

However, due to difficulties in growing and controlling the lattice of diamond, it is still desirable to identify other wide-bandgap materials as a host for qubits. Among these materials, AlN with one of the widest bandgap (6.12 eV) [66], small spin-orbit splitting (19 meV) [194] and mature high-quality crystal growth and doping techniques [195] is an interesting candidate for deployment of scalable quantum technologies. Additionally, AlN has piezoelectric properties [195, 196] which makes it a favorable host for a variety of control schemes for quantum spins. Recently, some theoretical studies revealed that point defects and defect complexes in AlN could act as qubits for quantum technologies [24, 26, 27, 197]. Results from density functional theory (DFT) calculations suggest that the spin character of nitrogen vacancies (V_N) in AlN could be altered by complexing with an adjacent impurity (such as Ti, Zr, or Hf) [26, 27] or by applying strain to the host material [24]. It is theoretically predicted that ($Ti_{Al} - V_N$) complex or V_N^- defects under realistic strain conditions, exhibit a spin-triplet ground state which represents promising qubit candidates. However, to our knowledge, the spin character of these defects, has not been examined experimentally. In this letter, using electron spin resonance (ESR) spectroscopy, we provide experimental evidence, confirming the formation of paramagnetic centers with spin-triplet (S=1) characteristics.

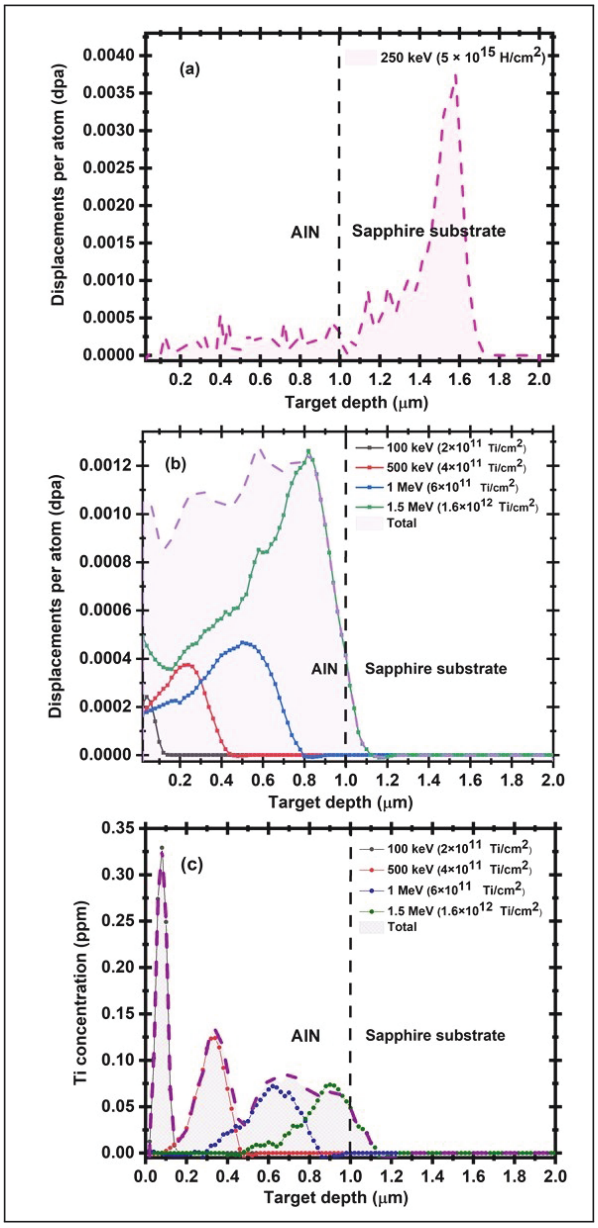

Figure 6.1 Depth profile of displacement damages for (a) 250 keV H atom implantation in AlN with a fluence of $5 \times 10^{15} H/cm^2$ and, (b) Ti implanted AlN films with different ion energy and implantation fluence and (c) Ti atom concentration for different ion implantation energies, according to SRIM simulations.

6.3 Material and Methods

In our study, we used AlN epitaxial films with a thickness of 1 micron on 450 microns sapphire single-crystal substrate (Dowa Electronics Materials Co.). These samples were grown by metal-organic chemical vapor deposition (MOCVD) and the crystal orientation is along the $< 0001 >$

c-axis, as we see below. To create vacancy-based defects, we used ion implantation with a variety of atoms including hydrogen and titanium. The first group of samples was ion-implanted using hydrogen atoms at the fluence of 5×10^{15} H/cm^2 with an acceleration voltage of 250 keV. For the other samples, ion implantation was performed using Ti atoms with implant energies of 100 keV, 500 keV, 1MeV, and 1.5 MeV, and fluences of 2×10^{11} Ti/cm^2, 4×10^{11} Ti/cm^2, 6×10^{11} Ti/cm^2 and 1.6×10^{12} Ti/cm^2, respectively. The ion implantation was carried out on a 1.7 MV tandem accelerator at room temperature and at an angle of 7° from the surface normal to avoid channeling. The depth distribution of displacement damage and Ti concentration in the host material is estimated using SRIM 2013 [198] simulations. We see from Figure.6.1 that the single H implantation produces a nearly uniform damage profile reaching 0.03% displacements per atom (dpa), while the Ti implantations produce a relatively uniform damage profile at a level of 0.1% dpa. We note that SRIM does not take into account effects such as dynamic annealing or the effects of damage concentration on its stability, so the actual damage level might be different. To partially remove the lattice damages caused by implantation, ion implantation was followed by thermal annealing at 1050°C for 1h in an Ar atmosphere.

The crystalline structure of the AlN films was investigated through $(\theta - 2\theta)$ scans using a Bruker (D8 Discover Model) X-ray diffractometer with high-intensity Cu-Kα radiation ($\lambda = 1.5406$ Å).

Micro-Raman measurements were carried out at room temperature using a backscattering configuration. A Labram-800 Raman spectrometer equipped with a nitrogen-cooled charge-coupled device (CCD) was used to record the Raman spectra. A He-Ne laser emitting at 632.8 nm was used at a constant power of 1.3 mW as the excitation source and a 50× microscope objective was used to focus the laser beam to a spot diameter of about 3 μm on the sample surface.

Electron spin resonance (ESR) measurements were recorded at room temperature, using a JEOL FA-200, X-band spectrometer operating at 9.45 GHz, and sweeping the magnetic field from 0 to 1000 mT. The ESR spectra of all samples were recorded with the magnetic field directed both parallel ($B \parallel C$) and perpendicular ($B \perp C$) to the c-axis of AlN crystal, to determine any spin anisotropy of the defects. ESR spectra were recorded in dark and under illumination with a solar simulator lamp, in order to determine if the paramagnetic states associated with these defects are optically active. All ESR simulations discussed in this work were performed using the EasySpin software based on an anisotropic spin Hamiltonian. [199].

6.4 Results and Discussion

In order to study the effects of implantation and thermal annealing on the structure of AlN films, XRD and Raman spectroscopy has been done. Figure.6.2 shows the XRD ($\theta - 2\theta$) patterns of as-grown AlN film, H-implanted , and Ti-implanted AlN films after heat treatment under Ar atmosphere at 1050°C for 1h. The as-grown film show features at 36° and 76.4°, which correspond to (0002) and (0004) AlN diffraction peaks [160]. The absence of other diffraction peaks reveals that the AlN film is purely c-axis oriented. For the H-implanted and Ti-implanted films after thermal annealing, the position of the diffraction peaks are shifted to the lower diffraction angles. This shift is associated with a change in the local strain in the AlN film as a result of the ion implantation and heat treatment. Using Bragg's law, we have calculated the c parameter of the different samples. The strain value can be determined by means of the expression $\Delta c = (c - c_{bulk})/c_{bulk}$, where $c_{bulk} = 4.980$ Åis the c-lattice parameter of the bulk AlN [161]. The value of the c parameter and strain for the different samples is shown in Table 6.1. The XRD results reveal that the amount of local strain along the c-axis of the as-grown AlN film is 0.08%. Such a residual strain in this film is due to the large mismatch in the lattice and thermal expansion coefficient of sapphire and AlN layer [200]. For the post-implantation annealed samples, the amount of strain along the c-axis depends on the implanted ion species, with values of 0.14% and 0.24% for the AlN:H/ Ar and AlN:Ti/ Ar samples, respectively. The (0002) and (0004) diffraction peaks of the H-implanted and Ti-implanted samples are wider than those of the as-grown films, however, no other XRD peaks were observed in these samples. This behavior indicates that the crystal quality of the films is partially changed after implantation and thermal annealing, but the films are still purely c-axis oriented.

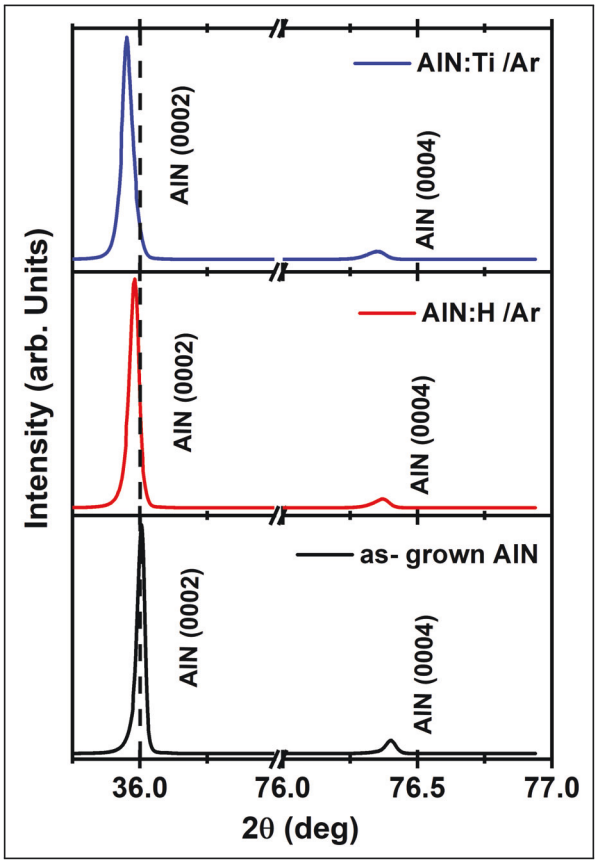

Figure 6.2 Diffractograms of Ti-implanted (top) and H-implanted (middle) AlN films after annealing. The bottom panel shows the diffractogram of the as-grown AlN film for reference. The dashed line represents the position of the (0002) diffraction peak for the as-grown AlN film.

To analyze the crystal quality and substantiate the observed strain in AlN films, Raman spectroscopy was performed. Typical Raman spectra of our samples are shown in Figure.6.3. To avoid sample heating, we used a low laser excitation power of 1.3 mW. The Raman spectra exhibits characteristic $E_2(high)$ and $A_1(TO)$ modes at 656.9 cm^{-1} and 632.5 cm^{-1} respectively, where the $E_2(high)$ mode is the strongest allowed mode in c-textured wurtzite AlN film [173]. There is no evidence of Raman scattering or local vibrational modes associated with the disorder, which is a signature of the good quality of our AlN films. The full-width at half-maximum of the $E_2(high)$ band measured on all samples varies between 4 and 5 cm^{-1}. These values are close to the value of 3 cm^{-1} reported for high-quality AlN bulk single crystals [165]. The inset of Figure.6.3 shows the central frequency of the $E_2(high)$ mode for the different samples. The observed shift was 1.9 cm^{-1} and 2.7 cm^{-1} for the AlN:H/ Ar and AlN:Ti/ Ar respectively. This mode has been shown to be dependent on the biaxial strain in the AlN film [201]. The inset of Figure.6.3 revealed that the Raman shifts are compatible with the calculated strain values from XRD measurements and demonstrate that, compared to the as-grown AlN film, the AlN:H/ Ar

Sample	c ($A°$)	Strain(%)	Raman E_2(high) (cm^{-1})
as-grown AlN	4.984	0.08	656.9
AlN:H/ Ar	4.987	0.14	655.1
AlN:Ti/ Ar	4.992	0.24	654.0

Table 6.1 Lattice parameter, c-axis strain and, position of the $E_2(high)$ vibrational peak for the different AlN films.

and AlN:Ti/ Ar films have a higher amount of residual strain.

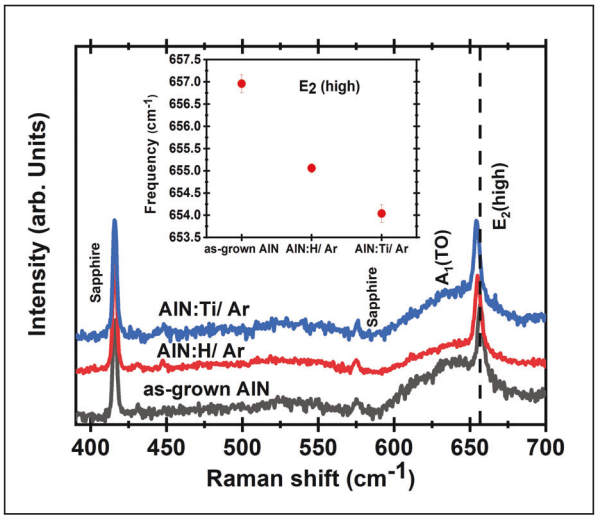

Figure 6.3 Raman spectra measured at room temperature from the ion-implanted and as-grown AlN films. The implanted samples are annealed under an Ar atmosphere. The dashed line shows the position of the $E_2(high)$ vibrational mode for the as-grown AlN film. The inset shows the Raman shift of the $E_2(high)$ vibrational mode, as a function of the strain for the different samples.

To study the spin character of the intrinsic and extrinsic defects in our AlN films, we used ESR spectroscopy. Precautions must be taken when analyzing the ESR spectra of our samples because the contribution of the sapphire substrate to the ESR signal is not negligible. Since the irradiation and thermal annealing procedure might affect the substrate, we recorded the ESR spectra of the AlN:H/ Ar and AlN:Ti/ Ar samples after removing the AlN layer in a KOH solution. The wet chemical etching was performed in a KOH-based solution with a concentration of 15% at the temperature of 60 $°C$. Such concentration is known not to etch or to add defects in sapphire. Our results show that the ESR spectra of samples with removed AlN layer (sapphire substrate) and the as-grown AlN film are very similar. This indicates that the sapphire is not responsible for the broad ESR peaks observed at $\sim$ 295 mT in the treated AlN films, which will

be described later in the text.

Room-temperature ESR spectra of the as-grown AlN films and sapphire substrates for both B-field parallel to the c-axis ($B \parallel C$) and B-field perpendicular to the c-axis ($B \perp C$) are shown in Figure.6.4 (a-f). The sharp spectral features observed in these spectra are assigned to color centers in the sapphire substrate. The ESR spectra of the films processed by ion implantation and annealing are shown in Figure.6.4 (g) to Figure.6.4 (k), respectively. On each of these spectra, we notice the appearance of an additional broad ESR feature, characteristic of the derivative of an absorption band. The ESR spectra of the AlN:H/ Ar film, shown in Figure.6.4 (g) and (h), display a broadband, characteristic for this type of signals and composed of a series of unresolved hyperfine lines, which are sensitive to the orientation of the B-field. The central resonance feature broadened and shifted to a higher resonance magnetic field value when the B-field orientation changed from parallel to perpendicular to the c-axis of the film. Note that two sharp features, seen at about 250 mT and 480 mT, are likely related to the paramagnetic defects in sapphire substrate. The spectra of AlN:Ti/ Ar film is shown in Figure.6.4 (i) and (k). Comparison between the spectra for $B \parallel C$ and $B \perp C$ orientations demonstrates that the location of the main resonance peak (around 295 mT) is mostly orientation independent, however, the resonance line profiles are slightly different for the two orientations. The intensity of this central feature is also lower than the one observed for the AlN:H/ Ar film, which could indicate a lower concentration of the paramagnetic defects in this sample. Spectra recorded for $B \perp C$ (Figure.6.4(k)) featured an extra distinct half-field signal around 140 mT, which can be assigned to spin-triplet paramagnetic defects.

Further discussion of the influence of the fabrication process on the different defects that may exist in our AlN films must be given before interpreting the different ESR features. Heavy ion implantation followed by thermal annealing creates a variety of point defects (vacancies, interstitial, and substitutional atoms) and defect complexes (vacancy-impurity pairs, aggregates, etc.) in AlN film. In addition to the point defects, O and C impurities were incorporated during the growth process and existed in form of substitutional atoms at the N site (O_N and C_N). Furthermore, the implanted Ti atoms can replace Al atoms (Ti_{Al}) and act as point defects and/or defect complexes such as vacancy-interstitial aggregates. Based on the previous studies [197, 202–204] the most likely candidates for the paramagnetic defects in AlN are nitrogen-vacancy (V_N), substitutional oxygen atoms in nitrogen site (O_N), substitutional carbon atoms in nitrogen site (C_N), and nitrogen-vacancy complexes. Previously, it was reported that [202], O_N and C_N defects form a shallow donor (SD) in AlN which are activated under illumination. However, after a thorough investigation using a solar simulator, we observed no distinction between ESR measured in dark vs, under illumination. Therefore, we exclude

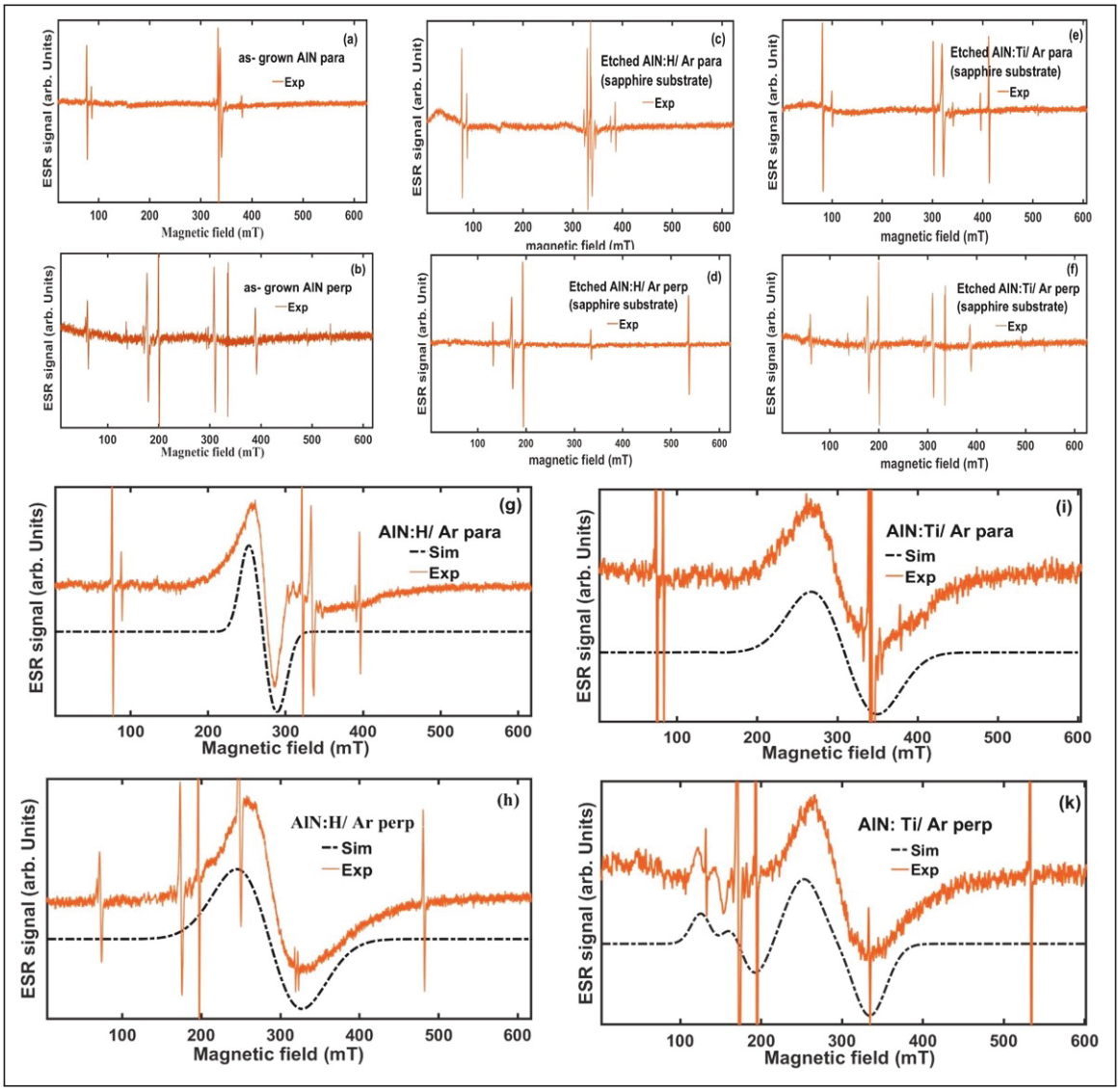

Figure 6.4 RT X-band ESR spectra of as-grown AlN (a,b), sapphire substrate from etched AlN:H/ Ar sample (c,d), sapphire substrate from etched AlN:Ti/ Ar sample (e,f), H-implanted AlN (g,h), and Ti-implanted AlN (i,k) films for the magnetic field parallel and perpendicular to the c-axis of AlN film. Simulation results from EasySpin are shown using dash lines.

Sample	g_x	g_y	g_z	spin	$lw_x(MHz)$	$lw_y(MHz)$	$lw_z(MHz)$	D(MHz)	E(MHz)
AlN:H/ Ar	2.36	2.36	2.49	1/2	616	616	840	-	-
AlN:Ti/ Ar	2.15	2.15	2.73	1	1900	1900	2400	2900	580

Table 6.2 ESR parameters of AlN:H/ Ar and AlN:Ti/ Ar films, calculated using the fit of experimental data to the EasySpin simulation, including the g-value, spin, ESR line width due to an anisotropic field-strain broadening (lw_x, lw_y, and lw_z), and zero-field splitting parameters.

O_N and C_N as a possible source of defects. This leaves nitrogen-vacancies and their associate complexes as the most likely source of the paramagnetic defects measured by ESR in our

AlN:H/ Ar sample. It is worth mentioning that previous ESR studies on the nitrogen-vacancies in AlN revealed resolved hyperfine structures originating from the interaction of electron spin with the magnetic nuclear lattice of ^{27}Al and ^{14}N [**?**]. However, these resolved hyperfine lines were not observed in our ESR spectra. In our study, we start from thin epitaxial AlN films with very low defect concentration: ESR spectra did not reveal the presence of a significant number of paramagnetic defects in the volume measured. However, after implantation and annealing, our results revealed the presence of a sufficiently large number of paramagnetic defects measurable by ESR. Since our implanted AlN films exhibit significant stress as reveled by XRD and Raman measurements, local fields at the site of defects will have a broad distribution compared to pristine single crystal AlN with zero or low stress. Consequently, this leads to broadening of the ESR lines leading to unresolved hyperfine and fine structure features. Furthermore, since we have a large number of defects in a small volume in our films, it would be expected that dipole-dipole interaction would play a role in broadening of the lines. ESR line broadening caused by the dipole-dipole interaction is well documented, for example in the case of paramagnetic defects in ZnO ([205]). This would explain why our ESR lines are so broad compared to previous studies of intrinsic defects in AlN. To the best of our knowledge implanted and annealed AlN films have not yet been studied by ESR.

Despite the unresolved fine and hyperfine features discussed above; we do still see clear features associated with anisotropy of the local crystal environment. The most notable anisotropic feature observed, when comparing the ESR spectra measured for the static field parallel and perpendicular to the c-axis of the crystal, is a resonance peak at half field of the main resonance for the perpendicular orientation of the static field. This is consistent with a D-tensor that has a specific orientation with respect to the crystal axes. The line shape profile of the main resonance peak is also different for the two field orientations as well, suggesting that the spin Hamiltonian parameters, such as the g-tensor and hyperfine tensor are anisotropic.

Furthermore, our results show that the implanted ion species has an impact on the type of

defects and the density of extrinsic defects resulting from the implantation/annealing process. Recently it was theoretically predicted that substitutional Ti dopant at an Al site can bind to a nitrogen-vacancy to form a (Ti_{Al}-V_N) complex in AlN [26, 27, 197]. Based on this recent work, these complexes were found to be energetically favorable and possess spin triplet ground state. As a result, (Ti_{Al}-V_N) complexes could be one of the major sources of paramagnetic defects in the AlN:Ti/ Ar sample.

To better understand the origin of the ESR features, we have used the EasySpin software. We have simplified the spin Hamiltonian by not adding the hyperfine interaction term since the nature of the observed broad lines does not allow us to determine the hyperfine interaction parameters concisely. Instead, we have introduced an anisotropic field-strain broadening for simulating our spectra. This anisotropic broadening is likely due to unresolved hyperfine broadening, dipole-dipole interaction, and g-strain broadening, which is expected since the AlN film is highly strained after implantation and annealing as discussed previously. The spin Hamiltonian used to simulate our spectra is given by:

$$H_{Zeeman} = \mu_B(g_x S_x B_x + g_y S_y B_y + g_z S_z B_z) \tag{6.1}$$

Here g_x, g_y, and g_z are the components of the g-tensor in the principal axes. For the nitrogen-vacancies, which are the most likely candidate for the observed ESR spectra, the wavefunction of an unpaired electron localized at a nitrogen-vacancy site. As a result, the hyperfine interaction would arise from the interaction of the electron spin at the defect site with surrounding ^{27}Al nuclei spins. Simulation of our spectra for (V_N^0) in both $B_\parallel$ and $B_\perp$ orientations, using Eq.6.1 are shown in Figure.6.4 (g) and (h). The values obtained from the simulation are listed in Table.6.2. The components of the g tensor extracted from our fit are 2.36, 2.36, and 2.49 for the g_x, g_y, and g_z respectively. These values are larger than the free-electron g-value, which indicates significant spin-orbit mixing of the paramagnetic defects observed in the AlN:H/ Ar samples [206].

For the AlN:Ti/ Ar film, since there is a notable ESR resonance peak at half the field of the primarily resonance peak which is likely associated with a "half-field" transition, we have added a zero-field splitting (ZFS) term to the spin Hamiltonian, given by:

$$H_{ZFS} = D_x S_x^2 + D_y S_y^2 + D_z S_z^2 \tag{6.2}$$

The above Hamiltonian is defined in the frame of the principal axes of the zero-field interaction. Since the zero-field interaction has no isotropic contribution, it is typically defined by a uniaxial and a rhombic parameter that is related to the diagonal matrix elements of the D-tensor by $D = \frac{3}{2}D_z$ and $E = \frac{D_x - D_y}{2}$, respectively.

The wurtzite crystal structure of AlN belongs to the C_{6v} space group, therefore we have used the C_{6v} space group to simulate our ESR. The uniaxial symmetry of the wurtzite crystal is expected to give rise to highly anisotropic ESR signals. We find that our simulations best fit our spectra when both the D-tensor and g-tensor principal axes are rotated perpendicular to the c-axis of the crystal. Our ESR spectra for the static field parallel and perpendicular to the c-axis of the crystal are shown in Figure.6.4 (i) and (k) of the paper. The simulated spectra were produced using the spin Hamiltonian in Eq.6.1 and 6.2 with the addition of an anisotropic strain to account for the line broadening. We have used HStrain function in Easyspin for this line broadening. The simulation parameters are provided in the Table.6.2, where the lw_x, lw_y, and lw_z are the ESR line broadening due to an anisotropic field-strain broadening.

Note several key points in our procedure for adjusting the parameters of our model. The first important point is related to the fact that a resonance peak is observed at about 120 mT only when the static magnetic field is oriented perpendicular to the c-axis of the crystal. This signature corresponds to the normally forbidden transition $\Delta m_s = \pm 2$, which becomes visible at half the field of the main resonance peak $\Delta m_s = \pm 1$, for a defect with $S > 1/2$. For the specified orientations of the g- and D-tensors with respect to the crystal axes, the resonance peak $\Delta m_s = \pm 2$ is enhanced due to the mixing of the m_s orbitals for the static field oriented perpendicular to the c-axis. For defects with spin S=1, our simulation results reproduce well the experimental spectra. When considering defects with a value of $S > 1$, a larger number of transitions become allowed, resulting in new or broadened peaks that do not match the shape of the observed ESR spectra.

Alternatively, we may attempt to simulate the ESR spectra by using a strongly anisotropic g tensor with a component $g_{||} = 5$ in order to generate a resonance peak at $\sim$ 120 mT for the perpendicular direction of the field. However, to the best of our knowledge, defects with such large g values have not been reported or predicted theoretically in AlN. On the other hand, results of recent DFT calculations have shown that AlN with Ti adatoms supports nitrogen-vacancy defects or complexes with a triplet ground state. Furthermore, it would be highly coincidental to observe a signal at half the field of the primary signal that is not associated with the primary defect center. For these reasons, we believe that our interpretation of the ESR spectra is more plausible than alternative interpretations. Also, given the observed line broadening that blurs the signatures of hyperfine structures, we do not believe that further angular-dependent ESR

measurements will be useful to validate our interpretation of the results. Instead, further studies using double electron nuclear resonance and high field ESR measurements would help to resolve the hyperfine structures of this defect, which would allow to determine its spin Hamiltonian parameters with reduced ambiguity. Although these studies are of interest to better understand the nature of this defect and the spin Hamiltonian parameters associated with it, the extent of these studies is far beyond the scope of our exploratory work presented here and will be produced in future work.

6.5 Conclusions

ESR was used to investigate the nature of the spin defects in AlN. Two types of films were studied: H-implanted AlN film and Ti-implanted film, and both samples are annealed under an Ar atmosphere. By comparing of quantum-mechanical ESR simulations and experimental results we conclude that ESR spectra of the AlN:H/ Ar film can be described by a spin Hamiltonian with $S = \frac{1}{2}$ and anisotropic g-values. These results are consistent with the presence of spin defects associated with neutral nitrogen-vacancies. For the AlN:Ti/ Ar sample, in addition to the central ESR signal, a lower intensity signal was observed at the half-field value of the main transition. These ESR spectra, for both $B \parallel C$ and $B \perp C$ orientations, can be reproduced by considering defects with a triplet spin character and anisotropic g-factor and a zero-field splitting of 2900 MHz. DFT calculations indicate that the point defects, such as V_N^- and $(Ti_{Al} - V_N)$ complexes could be candidates for these paramagnetic centers. However, the exact origin is still unknown and needs further investigation. This work provides a new insight into the electron spin properties of defects in AlN which might find applications for quantum information and quantum sensing technology.

Acknowledgments

This work is supported by NSERC, CFI, FRQNT, and Institut quantique de l'Université de Sherbrooke. Some of the work was carried out on central facilities of the RQMP. The authors would like to thank also M. Dion for his support with XRD measurements, and L. Godbout for his help with the maintenance and operation of the ion accelerator.

CHAPTER 7 Concluding Remarks

This work has made significant strides in various areas pertaining to point defects found in AlN films. Specifically, we have delved into the development of protocols aimed at creating, managing, identifying, and forecasting properties of defects. The research has concentrated on exploring the impact of group IV impurities and their interactions with V_N on the properties of the defects.

The main focus of this study has been on investigating two types of defects, $(Zr_{Al} - V_N)^0$ and $(Ti_{Al} - V_N)^0$. We have carefully scrutinized their characteristics to understand their properties, formation, and impact on AlN films. The findings of this study have the potential to contribute significantly to the field of materials science and advance our knowledge of defect engineering in AlN films.

The initial phase of this thesis focused on the creation and analysis of $(Zr_{Al} - V_N)^0$ defects in AlN films. To achieve this, we utilized the Zr ion implantation technique and carried out thermal annealing using various protocols. This resulted in the successful formation of $(Zr_{Al} - V_N)^0$ point defects in the AlN films. We used a combination of structural characterization techniques and photoluminescence spectroscopy to identify the defects and analyze the impact of the implantation and annealing processes on the amount of strain in the AlN films. The results of these studies have enabled us to gain a better understanding of the properties and behavior of $(Zr_{Al} - V_N)^0$ defects in AlN films.

Furthermore, we conducted first-principles calculations based on density functional theory (DFT) to explore the impact of strain on the spin character of point defects in AlN films. The findings suggest that strain engineering of AlN films could be an effective method for controlling the spin character of defects. These results are expected to be valuable for future studies on defect engineering in AlN films and could have implications for the development of advanced electronic and optoelectronic devices.

In addition, a custom μPL spectroscopy setup was designed to investigate the properties of $(Zr_{Al} - V_N)^0$ complex defects in AlN films. Using this technique, bright micro-size spots with dark backgrounds on the AlN:Zr/FG film were detected. A sharp and narrow zero-phonon line (ZPL) at 685.5 nm with a phonon sideband around 700 nm was observed, which was attributed to the $(Zr_{Al} - V_N)^0$ complex defects.

Furthermore, the temperature-dependence behavior and time-resolved photoluminescence spectra of these defects were studied, and a scenario for the optical decay mechanism of the

$(Zr_{Al} - V_N)^0$ complex defects was proposed based on the results. The $(Zr_{Al} - V_N)^0$ complex defects also showed a relatively high Debye-Waller factor up to 18.5%, suggesting their potential as single-photon emitters in AlN films.

However, the excitation-power-dependent behavior of the $(Zr_{Al} - V_N)^0$ defects displayed a saturation count rate of approximately 2.8×10^4, which is lower than what has been observed for other defect-related single-photon emitters. Therefore, further investigation, such as a second-order autocorrelation measurement, is necessary to explore the possibility of using these defects as single-photon emitters. These findings contribute to the growing understanding of the properties and potential applications of defect complexes in AlN films.

In the final section of this research, we utilized electron spin resonance (ESR) spectroscopy to investigate the nature of spin defects in H-implanted and Ti-implanted AlN films. By combining experimental results with quantum mechanical ESR simulations, we were able to gain insights into the properties of these defects.

For the AlN:H/Ar sample, we observed ESR spectra that could be explained with a spin Hamiltonian with $S = \frac{1}{2}$ and anisotropic g-value. Through our simulations, we were able to confirm that the spin character of the defects was consistent with the spin Hamiltonian. Our findings suggest that the defects in the AlN:H/Ar sample are likely related to hydrogen point defects.

In the AlN:Ti/Ar sample, in addition to the central resonance peak, a low-intensity signal was observed at a half-field value of the main transition. By using simulations, we determined that the spin character of these defects was consistent with a triplet spin system with S = 1, an isotropic g-factor of 2.22, and a zero-field splitting of 2800 MHz. Our DFT calculations suggest that the origin of these paramagnetic centers might be related to $(Ti_{Al} - V_N)^0$ or $(V_N)^-$ point defects in AlN. These results provide important insights into the nature of spin defects in AlN films, and our combined experimental and theoretical approach has proven to be a powerful tool for studying these defects. These findings have potential implications for the development of new materials and devices that rely on the properties of spin defects.

In summary, this thesis has shed new light on the optical properties and spin characteristics of defects in aluminum nitride (AlN), offering fresh perspectives that could prove instrumental in a range of quantum technologies. This research has the potential to pave the way for a host of innovative applications, such as quantum sensing and the development of single-photon emitters. By delving deeper into the fundamental properties of defects in AlN, this study could have far-reaching implications for the future of quantum research and technology. As such, the findings presented in this thesis represent a significant contribution to the field and may inspire further investigations and breakthroughs in the exciting and rapidly-evolving realm of quantum science.

7.1 Suggestions for Further Works

This thesis has made significant strides in uncovering crucial correlations and introducing methodologies that offer valuable insights into the field. However, there is still much more to be discovered, and the techniques presented here can be further developed to yield even more impactful results. As such, the following suggestions are proposed for further work:

Firstly, based on the optical characterization results, it appears that the $(Zr_{Al} - V_N)^0$ defects in AlN may have the potential to serve as an exciting source of single-photon emitters. However, to confirm this possibility, a thorough investigation using excitation-power-dependent $g^{(2)}(\tau)$ measurement is required. By conducting such experiments, we can gain a deeper understanding of the quantum properties of these defects and potentially unlock their full potential as a source of single-photon emitters.

Secondly, the spin character of the $(Zr_{Al} - V_N)^0$ defects in AlN could be further examined using electron spin resonance (ESR) techniques. Such investigations could shed light on the spin dynamics of these defects, and help to develop a more comprehensive understanding of their behavior and potential applications.

Lastly, given that AlN is a piezoelectric material, one interesting idea for future work would be to design a surface acoustic wave resonator (SAW) on top of an AlN film. This approach could potentially be used to achieve strain-driven spin control of defects in AlN, leading to exciting new possibilities for quantum sensing and other applications.

In conclusion, the present thesis has laid a solid foundation for future investigations into the properties and applications of defects in AlN. By pursuing the suggested avenues of further work, researchers can continue to build on this foundation and unlock new and exciting possibilities in the rapidly evolving field of quantum science.

REFERENCES

[1] J. Weber *et al.*, "Quantum computing with defects," *Proceedings of the National Academy of Sciences*, vol. 107, no. 19, pp. 8513–8518, 2010.

[2] Y. Xue *et al.*, "Single-photon emission from point defects in aluminum nitride films," *The Journal of Physical Chemistry Letters*, vol. 11, no. 7, pp. 2689–2694, 2020.

[3] Y. Xue, "Experimental optical properties of single-photon emitters in aluminum nitride film," *The Journal of Physical Chemistry C*, 2021.

[4] T.-J. Lu *et al.*, "Bright high-purity quantum emitters in aluminum nitride integrated photonics," *ACS Photonics*, vol. 7, no. 10, pp. 2650–2657, 2020.

[5] A. Li, "Interaction of nanoparticles with radiation," *arXiv preprint astro-ph/0311066*, 2003.

[6] M. W. Doherty *et al.*, "The nitrogen-vacancy colour centre in diamond," *Physics Reports*, vol. 528, no. 1, pp. 1–45, 2013.

[7] G. Davies, "Vibronic spectra in diamond," *Journal of Physics C: Solid state physics*, vol. 7, no. 20, p. 3797, 1974.

[8] A. Gruber *et al.*, "Scanning confocal optical microscopy and magnetic resonance on single defect centers," *Science*, vol. 276, no. 5321, pp. 2012–2014, 1997.

[9] A. Gali *et al.*, "Theory of neutral divacancy in sic: a defect for spintronics," in *Materials science forum*, vol. 645. Trans Tech Publ, 2010, pp. 395–397.

[10] J. Weber *et al.*, "Defects in sic for quantum computing," *Journal of Applied Physics*, vol. 109, no. 10, p. 102417, 2011.

[11] L. Gordon *et al.*, "Quantum computing with defects," *MRS bulletin*, vol. 38, no. 10, pp. 802–807, 2013.

[12] W. F. Koehl *et al.*, "Room temperature coherent control of defect spin qubits in silicon carbide," *Nature*, vol. 479, no. 7371, pp. 84–87, 2011.

[13] A. L. Falk *et al.*, "Polytype control of spin qubits in silicon carbide," *Nature communications*, vol. 4, no. 1, pp. 1–7, 2013.

[14] A. L. Exarhos *et al.*, "Magnetic-field-dependent quantum emission in hexagonal boron nitride at room temperature," *Nature communications*, vol. 10, no. 1, pp. 1–8, 2019.

[15] G. Grosso *et al.*, "Tunable and high-purity room temperature single-photon emission from atomic defects in hexagonal boron nitride," *Nature communications*, vol. 8, no. 1, pp. 1–8, 2017.

[16] N. R. Jungwirth *et al.*, "Temperature dependence of wavelength selectable zero-phonon emission from single defects in hexagonal boron nitride," *Nano letters*, vol. 16, no. 10, pp. 6052–6057, 2016.

[17] T. T. Tran *et al.*, "Quantum emission from hexagonal boron nitride monolayers," *Nature nanotechnology*, vol. 11, no. 1, pp. 37–41, 2016.

[18] J. Li *et al.*, "Band structure and fundamental optical transitions in wurtzite aln," *Applied Physics Letters*, vol. 83, no. 25, pp. 5163–5165, 2003.

[19] S.-H. Wei and A. Zunger, "Valence band splittings and band offsets of aln, gan, and inn," *Applied Physics Letters*, vol. 69, no. 18, pp. 2719–2721, 1996.

[20] J. C. Rojo *et al.*, "Report on the growth of bulk aluminum nitride and subsequent substrate preparation," *Journal of crystal growth*, vol. 231, no. 3, pp. 317–321, 2001.

[21] M. Bickermann *et al.*, "Uv transparent single-crystalline bulk aln substrates," *physica status solidi c*, vol. 7, no. 1, pp. 21–24, 2010.

[22] H. Okumura, T. Kimoto, and J. Suda, "Reduction of threading dislocation density in 2h-aln grown on 6h-sic (0001) by minimizing unintentional active-nitrogen exposure before growth," *Applied physics express*, vol. 4, no. 2, p. 025502, 2011.

[23] Y. Taniyasu, M. Kasu, and T. Makimoto, "Electrical conduction properties of n-type si-doped aln with high electron mobility (> 100 cm 2 v- 1 s- 1)," *Applied Physics Letters*, vol. 85, no. 20, pp. 4672–4674, 2004.

[24] H. Seo, M. Govoni, and G. Galli, "Design of defect spins in piezoelectric aluminum nitride for solid-state hybrid quantum technologies," *Scientific reports*, vol. 6, no. 1, pp. 1–10, 2016.

[25] S. G. Bishop *et al.*, "Room-temperature quantum emitter in aluminum nitride," *ACS photonics*, vol. 7, no. 7, pp. 1636–1641, 2020.

[26] H. Seo *et al.*, "Designing defect-based qubit candidates in wide-gap binary semiconductors for solid-state quantum technologies," *Physical Review Materials*, vol. 1, no. 7, p. 075002, 2017.

[27] J. Varley, A. Janotti, and C. Van de Walle, "Defects in aln as candidates for solid-state qubits," *Physical Review B*, vol. 93, no. 16, p. 161201, 2016.

[28] G. Zhang *et al.*, "Material platforms for defect qubits and single-photon emitters," *Applied Physics Reviews*, vol. 7, no. 3, p. 031308, 2020.

[29] A. Acín *et al.*, "The european quantum technologies roadmap," *arXiv preprint arXiv:1712.03773*, 2017.

[30] C. L. Degen, F. Reinhard, and P. Cappellaro, "Quantum sensing," *Reviews of modern physics*, vol. 89, no. 3, p. 035002, 2017.

[31] R. P. Feynman, "Simulating physics with computers," in *Feynman and computation*. CRC Press, 2018, pp. 133–153.

[32] P. W. Shor *et al.*, "Polynomial-time algorithms for prime factorization and discrete logarithms on a quantum computer. los alamos physics preprint archive," 1995.

[33] T. D. Ladd *et al.*, "Quantum computers," *nature*, vol. 464, no. 7285, pp. 45–53, 2010.

[34] A. Steane, "Quantum computing," *Reports on Progress in Physics*, vol. 61, no. 2, p. 117, 1998.

[35] N. Gisin and R. Thew, "Quantum communication," *Nature photonics*, vol. 1, no. 3, pp. 165–171, 2007.

[36] S. Wang *et al.*, "Twin-field quantum key distribution over 830-km fibre," *Nature Photonics*, pp. 1–8, 2022.

[37] S. Slussarenko and G. J. Pryde, "Photonic quantum information processing: A concise review," *Applied Physics Reviews*, vol. 6, no. 4, p. 041303, 2019.

[38] Y. A. Pashkin *et al.*, "Josephson charge qubits: a brief review," *Quantum Information Processing*, vol. 8, no. 2, pp. 55–80, 2009.

[39] H.-L. Huang *et al.*, "Superconducting quantum computing: a review," *Science China Information Sciences*, vol. 63, no. 8, pp. 1–32, 2020.

[40] D. P. DiVincenzo, "The physical implementation of quantum computation," *Fortschritte der Physik: Progress of Physics*, vol. 48, no. 9-11, pp. 771–783, 2000.

[41] S. Mahajan, "Defects in semiconductors and their effects on devices," *Acta materialia*, vol. 48, no. 1, pp. 137–149, 2000.

[42] Y. Peter and M. Cardona, *Fundamentals of semiconductors: physics and materials properties*. Springer Science & Business Media, 2010.

[43] C. Merckling, "Monolithic integration of ingaas on si (001) substrate for logic devices," in *High Mobility Materials for CMOS Applications*. Elsevier, 2018, pp. 71–114.

[44] C. Freysoldt *et al.*, "First-principles calculations for point defects in solids," *Reviews of modern physics*, vol. 86, no. 1, p. 253, 2014.

[45] S. M. Sze, *Semiconductor devices: physics and technology*. John wiley & sons, 2008.

[46] F. Williams, "Donor—acceptor pairs in semiconductors," *physica status solidi (b)*, vol. 25, no. 2, pp. 493–512, 1968.

[47] D. G. Thomas, M. Gershenzon, and F. Trumbore, "Pair spectra and" edge" emission in gallium phosphide," *Physical review*, vol. 133, no. 1A, p. A269, 1964.

[48] I. Pelant and J. Valenta, *Luminescence spectroscopy of semiconductors*. OUP Oxford, 2012.

[49] J. Davidsson, "Color centers in semiconductors for quantum applications: A high-throughput search of point defects in sic," Ph.D. dissertation, Linköping University Electronic Press, 2021.

[50] P. V. Klimov *et al.*, "Quantum entanglement at ambient conditions in a macroscopic solid-state spin ensemble," *Science advances*, vol. 1, no. 10, p. e1501015, 2015.

[51] N. Bar-Gill *et al.*, "Solid-state electronic spin coherence time approaching one second," *Nature communications*, vol. 4, no. 1, pp. 1–6, 2013.

[52] G. Fuchs *et al.*, "Gigahertz dynamics of a strongly driven single quantum spin," *Science*, vol. 326, no. 5959, pp. 1520–1522, 2009.

[53] T. Kennedy *et al.*, "Single-qubit operations with the nitrogen-vacancy center in diamond," *physica status solidi (b)*, vol. 233, no. 3, pp. 416–426, 2002.

[54] J. Loubser and J. Van Wyk, "Electron spin resonance in annealed type 1b diamond," *Diamond Res*, vol. 11, pp. 4–7, 1977.

[55] M. G. Dutt *et al.*, "Quantum register based on individual electronic and nuclear spin qubits in diamond," *Science*, vol. 316, no. 5829, pp. 1312–1316, 2007.

[56] H. Bernien *et al.*, "Heralded entanglement between solid-state qubits separated by three metres," *Nature*, vol. 497, no. 7447, pp. 86–90, 2013.

[57] B. Gil, *III-Nitride Semiconductors and their modern devices*. OUP Oxford, 2013, vol. 18.

[58] I. A. I. Akasaki and H. A. H. Amano, "Crystal growth and conductivity control of group iii nitride semiconductors and their application to short wavelength light emitters," *Japanese journal of applied physics*, vol. 36, no. 9R, p. 5393, 1997.

[59] b. H. Morkoc *et al.*, "Large-band-gap sic, iii-v nitride, and ii-vi znse-based semiconductor device technologies," *Journal of Applied physics*, vol. 76, no. 3, pp. 1363–1398, 1994.

[60] M. Akiyama *et al.*, "Enhancement of piezoelectric response in scandium aluminum nitride alloy thin films prepared by dual reactive cosputtering," *Advanced Materials*, vol. 21, no. 5, pp. 593–596, 2009.

[61] M. A. Caro *et al.*, "Piezoelectric coefficients and spontaneous polarization of scaln," *Journal of Physics: Condensed Matter*, vol. 27, no. 24, p. 245901, 2015.

[62] M. Moreira *et al.*, "Aluminum scandium nitride thin-film bulk acoustic resonators for wide band applications," *Vacuum*, vol. 86, no. 1, pp. 23–26, 2011.

[63] F. Tasnadi *et al.*, "Origin of the anomalous piezoelectric response in wurtzite sc x al 1- x n alloys," *Physical review letters*, vol. 104, no. 13, p. 137601, 2010.

[64] C. Fei *et al.*, "Aln piezoelectric thin films for energy harvesting and acoustic devices," *Nano Energy*, vol. 51, pp. 146–161, 2018.

[65] X.-H. Xu *et al.*, "Morphological properties of aln piezoelectric thin films deposited by dc reactive magnetron sputtering," *Thin solid films*, vol. 388, no. 1-2, pp. 62–67, 2001.

[66] a. S. Strite and H. Morkoç, "Gan, aln, and inn: a review," *Journal of Vacuum Science & Technology B: Microelectronics and Nanometer Structures Processing, Measurement, and Phenomena*, vol. 10, no. 4, pp. 1237–1266, 1992.

[67] Y. Taniyasu, M. Kasu, and T. Makimoto, "An aluminium nitride light-emitting diode with a wavelength of 210 nanometres," *nature*, vol. 441, no. 7091, pp. 325–328, 2006.

[68] R. Nemanich *et al.*, "Negative electron affinity surfaces of aluminum nitride and diamond," *Diamond and Related Materials*, vol. 5, no. 6-8, pp. 790–796, 1996.

[69] M. Benjamin *et al.*, "Observation of a negative electron affinity for heteroepitaxial aln on α (6h)-sic (0001)," *Applied physics letters*, vol. 64, no. 24, pp. 3288–3290, 1994.

[70] C. Wu *et al.*, "Electron affinity at aluminum nitride surfaces," *Applied physics letters*, vol. 73, no. 10, pp. 1346–1348, 1998.

[71] R. Karabalin *et al.*, "Piezoelectric nanoelectromechanical resonators based on aluminum nitride thin films," *Applied Physics Letters*, vol. 95, no. 10, p. 103111, 2009.

[72] T. Koyama *et al.*, "Relation between al vacancies and deep emission bands in aln epitaxial films grown by nh 3-source molecular beam epitaxy," *Applied physics letters*, vol. 90, no. 24, p. 241914, 2007.

[73] T. Hoshi *et al.*, "Correlation between the violet luminescence intensity and defect density in aln epilayers grown by ammonia-source molecular beam epitaxy," *physica status solidi c*, vol. 5, no. 6, pp. 2129–2132, 2008.

[74] A. Sedhain *et al.*, "The origin of 2.78 ev emission and yellow coloration in bulk aln substrates," *Applied Physics Letters*, vol. 95, no. 26, p. 262104, 2009.

[75] W.-Y. Wang *et al.*, "Effect of high-temperature annealing on aln thin film grown by metalorganic chemical vapor deposition," *Chinese Physics B*, vol. 23, no. 8, p. 087810, 2014.

[76] Q. Hu *et al.*, "In-situ luminescence measurement for aln ceramics under reactor irradiation," *Radiation effects and defects in solids*, vol. 147, no. 4, pp. 283–292, 1999.

[77] B. Bastek *et al.*, "Analysis of point defects in aln epilayers by cathodoluminescence spectroscopy," *Applied Physics Letters*, vol. 95, no. 3, p. 032106, 2009.

[78] U. Vetter *et al.*, "Effective reduction of aln defect luminescence by fluorine implantation," *Diamond and related materials*, vol. 20, no. 5-6, pp. 782–784, 2011.

[79] Z. Wu *et al.*, "Effect of temperature on growth and ultraviolet photoluminescence of zn doped aln nanostructures," *Materials Letters*, vol. 136, pp. 95–98, 2014.

[80] L. Trinkler and B. Berzina, "Recombination luminescence in aluminum nitride ceramics," *physica status solidi (b)*, vol. 251, no. 3, pp. 542–548, 2014.

[81] S. Bellucci *et al.*, "Luminescence, vibrational and xanes studies of aln nanomaterials," *Radiation measurements*, vol. 42, no. 4-5, pp. 708–711, 2007.

[82] L. Shen, N. Wang, and X. Xiao, "Strong orange luminescence from aln whiskers," *Materials Letters*, vol. 94, pp. 150–153, 2013.

[83] S. Schweizer *et al.*, "Investigation of oxygen-related luminescence centres in aln ceramics," *physica status solidi (b)*, vol. 219, no. 1, pp. 171–180, 2000.

[84] B. Berzina *et al.*, "Oxygen-related defects and energy accumulation in aluminum nitride ceramics," *Radiation effects and defects in solids*, vol. 156, no. 1-4, pp. 241–247, 2001.

[85] M. Bickermann *et al.*, "Point defect content and optical transitions in bulk aluminum nitride crystals," *physica status solidi (b)*, vol. 246, no. 6, pp. 1181–1183, 2009.

[86] H. Hu *et al.*, "Synthesis and photoluminescence of aln: Mn hexagonal maze-like complex nanostructure," *Materials Letters*, vol. 70, pp. 34–36, 2012.

[87] J. Pastrňák, S. Pačesová, and L. Roskovcova, "Luminescent properties of the oxygen impurity centres in a1n," *Czechoslovak Journal of Physics B*, vol. 24, no. 10, pp. 1149–1161, 1974.

[88] J.-C. Nappé *et al.*, "Effect of swift heavy ion irradiations in polycrystalline aluminum nitride," *Nuclear Instruments and Methods in Physics Research Section B: Beam Interactions with Materials and Atoms*, vol. 269, no. 2, pp. 100–104, 2011.

[89] M. Benabdesselam *et al.*, "Thermoluminescence of aln. influence of synthesis processes," *The Journal of Physical Chemistry*, vol. 99, no. 25, pp. 10 319–10 323, 1995.

[90] A. Uedono *et al.*, "Vacancy-oxygen complexes and their optical properties in aln epitaxial films studied by positron annihilation," *Journal of Applied Physics*, vol. 105, no. 5, p. 054501, 2009.

[91] D. Spiridonov *et al.*, "Cathodoluminescence of oxygen-vacancy centers in structures of aluminum nitride," *Bulletin of the Russian Academy of Sciences: Physics*, vol. 79, no. 2, pp. 211–214, 2015.

[92] S. Chichibu *et al.*, "Excitonic emission dynamics in homoepitaxial aln films studied using polarized and spatio-time-resolved cathodoluminescence measurements," *Applied Physics Letters*, vol. 103, no. 14, p. 142103, 2013.

[93] R. Collazo *et al.*, "On the origin of the 265 nm absorption band in aln bulk crystals," *Applied Physics Letters*, vol. 100, no. 19, p. 191914, 2012.

[94] T. Nagashima *et al.*, "Structural and optical properties of carbon-doped aln substrates grown by hydride vapor phase epitaxy using aln substrates prepared by physical vapor transport," *Applied Physics Express*, vol. 5, no. 12, p. 125501, 2012.

[95] B. E. Gaddy *et al.*, "The role of the carbon-silicon complex in eliminating deep ultraviolet absorption in aln," *Applied Physics Letters*, vol. 104, no. 20, p. 202106, 2014.

[96] T. Schulz *et al.*, "Ultraviolet luminescence in aln," *physica status solidi (b)*, vol. 248, no. 6, pp. 1513–1518, 2011.

[97] N. Nepal *et al.*, "Optical properties of the nitrogen vacancy in aln epilayers," *Applied physics letters*, vol. 84, no. 7, pp. 1090–1092, 2004.

[98] R. Yu *et al.*, "Ultrawide-bandgap semiconductor aln crystals: Growth and applications," *Journal of Materials Chemistry C*, vol. 9, no. 6, pp. 1852–1873, 2021.

[99] M. Kneissl *et al.*, "The emergence and prospects of deep-ultraviolet light-emitting diode technologies," *nature photonics*, vol. 13, no. 4, pp. 233–244, 2019.

[100] R. Dalmau *et al.*, "Growth and characterization of aln and algan epitaxial films on aln single crystal substrates," *Journal of The Electrochemical Society*, vol. 158, no. 5, p. H530, 2011.

[101] D. Ehrentraut and Z. Sitar, "Advances in bulk crystal growth of aln and gan," *MRS bulletin*, vol. 34, no. 4, pp. 259–265, 2009.

[102] K. Lakin *et al.*, "Improved bulk wave resonator coupling coefficient for wide bandwidth filters," in *2001 IEEE Ultrasonics Symposium. Proceedings. An International Symposium (Cat. No. 01CH37263)*, vol. 1. IEEE, 2001, pp. 827–831.

[103] J. H. Kim *et al.*, "Aln piezoelectric materials for wireless communication thin film components," *Journal of Ceramic Processing Research*, vol. 3, no. 1, pp. 25–28, 2002.

[104] T. Palacios *et al.*, "Nanotechnology for saw devices on aln epilayers," *Materials Science and Engineering: B*, vol. 93, no. 1-3, pp. 154–158, 2002.

[105] M. Clement *et al.*, "Saw characteristics of aln films sputtered on silicon substrates," *Ultrasonics*, vol. 42, no. 1-9, pp. 403–407, 2004.

[106] C. Zuo, J. Van der Spiegel, and G. Piazza, "1.05-ghz cmos oscillator based on lateral-field-excited piezoelectric aln contour-mode mems resonators," *IEEE transactions on ultrasonics, ferroelectrics, and frequency control*, vol. 57, no. 1, pp. 82–87, 2009.

[107] G. Piazza, P. J. Stephanou, and A. P. Pisano, "Single-chip multiple-frequency aln mems filters based on contour-mode piezoelectric resonators," *Journal of Microelectromechanical Systems*, vol. 16, no. 2, pp. 319–328, 2007.

[108] D. J. Christle *et al.*, "Isolated electron spins in silicon carbide with millisecond coherence times," *Nature materials*, vol. 14, no. 2, pp. 160–163, 2015.

[109] ——, "Isolated spin qubits in sic with a high-fidelity infrared spin-to-photon interface," *Physical Review X*, vol. 7, no. 2, p. 021046, 2017.

[110] D. Lee *et al.*, "Topical review: spins and mechanics in diamond," *Journal of Optics*, vol. 19, no. 3, p. 033001, 2017.

[111] J. Teissier *et al.*, "Strain coupling of a nitrogen-vacancy center spin to a diamond mechanical oscillator," *Physical review letters*, vol. 113, no. 2, p. 020503, 2014.

[112] P. Ovartchaiyapong *et al.*, "Dynamic strain-mediated coupling of a single diamond spin to a mechanical resonator," *Nature communications*, vol. 5, no. 1, pp. 1–6, 2014.

[113] Y. Zhang, W. Liu, and H. Niu, "Native defect properties and p-type doping efficiency in group-iia doped wurtzite aln," *Physical Review B*, vol. 77, no. 3, p. 035201, 2008.

[114] Y. Tu *et al.*, "A paramagnetic neutral valon center in wurtzite aln for spin qubit application," *Applied Physics Letters*, vol. 103, no. 7, p. 072103, 2013.

[115] X. Wang *et al.*, "Spin-polarization of vgaon center in gan and its application in spin qubit," *Applied physics letters*, vol. 100, no. 19, p. 192401, 2012.

[116] I. Aharonovich, D. Englund, and M. Toth, "Solid-state single-photon emitters," *Nature Photonics*, vol. 10, no. 10, pp. 631–641, 2016.

[117] D. D. Awschalom *et al.*, "Quantum technologies with optically interfaced solid-state spins," *Nature Photonics*, vol. 12, no. 9, pp. 516–527, 2018.

[118] M. Atatüre *et al.*, "Material platforms for spin-based photonic quantum technologies," *Nature Reviews Materials*, vol. 3, no. 5, pp. 38–51, 2018.

[119] D. Chen, N. Zheludev, and W.-b. Gao, "Building blocks for quantum network based on group-iv split-vacancy centers in diamond," *Advanced Quantum Technologies*, vol. 3, no. 2, p. 1900069, 2020.

[120] A. J. Morfa *et al.*, "Single-photon emission and quantum characterization of zinc oxide defects," *Nano letters*, vol. 12, no. 2, pp. 949–954, 2012.

[121] A. M. Berhane *et al.*, "Bright room-temperature single-photon emission from defects in gallium nitride," *Advanced Materials*, vol. 29, no. 12, p. 1605092, 2017.

[122] X. Ding *et al.*, "On-demand single photons with high extraction efficiency and near-unity indistinguishability from a resonantly driven quantum dot in a micropillar," *Physical review letters*, vol. 116, no. 2, p. 020401, 2016.

[123] M. A. Nastasi and J. W. Mayer, *Ion implantation and synthesis of materials*. Springer, 2006, vol. 5.

[124] J. F. Ziegler and J. P. Biersack, *The Stopping and Range of Ions in Matter*. Boston, MA: Springer US, 1985, pp. 93–129. [Online]. Available: https://doi.org/10.1007/978-1-4615-8103-1_3

[125] D. Yuan *et al.*, "Structural and optical properties of ion-implanted titanium thin films studied by x-ray diffraction and spectroscopic ellipsometry," *Journal of Applied Physics*, vol. 101, no. 6, p. 063515, 2007.

[126] Z. Zhang *et al.*, "Determination of thickness and optical constants of thin films by x-ray diffraction and ellipsometry," *Thin Solid Films*, vol. 555, pp. 120–126, 2014.

[127] L. Molina-Luna *et al.*, "Structural and interfacial characterization of cu thin films on si (100) substrates grown by magnetron sputtering," *Journal of Materials Science: Materials in Electronics*, vol. 28, no. 3, pp. 2827–2832, 2017.

[128] C. V. Raman and K. S. Krishnan, "A new type of secondary radiation," *Nature*, vol. 121, no. 3048, pp. 501–502, 1928.

[129] G. Binnig, C. F. Quate, and C. Gerber, "Atomic force microscope," *Physical review letters*, vol. 56, no. 9, p. 930, 1986.

[130] D. Nečas and P. Klapetek, "Gwyddion: an open-source software for spm data analysis," *Open Physics*, vol. 10, no. 1, pp. 181–188, 2012.

[131] M. Chicoine *et al.*, "Oxy-nitrides characterization with a new erd-tof system," *Nuclear Instruments and Methods in Physics Research Section B: Beam Interactions with Materials and Atoms*, vol. 406, pp. 112–114, 2017.

[132] H. J. Whitlow *et al.*, "Time detector design for time-of-flight elastic recoil detection analysis (tof-e erda)," *Nuclear Instruments and Methods in Physics Research Section B: Beam Interactions with Materials and Atoms*, vol. 450, pp. 385–389, 2019.

[133] F. Schiettekatte *et al.*, "Allegria: a new interface to the erd program," *Nuclear Instruments and Methods in Physics Research Section B: Beam Interactions with Materials and Atoms*, vol. 219, pp. 125–129, 2004.

[134] A. Srivastava, "Photoluminescence spectroscopy of semiconductors," *INDIAN JOURNAL OF PURE & APPLIED PHYSICS*, vol. 27, no. 7-8, pp. 386–389, 1989.

[135] S. Wang, C. Shan, and X. Gao, "Photoluminescence excitation spectroscopy of semiconductors," *Journal of Semiconductors*, vol. 37, no. 2, p. 021001, 2016.

[136] W. Bu and Y. Zhang, "Photoluminescence excitation spectroscopy study of semiconducting quantum dots," *Journal of Materials Chemistry C*, vol. 5, no. 13, pp. 3197–3208, 2017.

[137] V. Butkus and L. Valkunas, "Photoluminescence excitation spectroscopy: applications to photosynthetic systems," *Journal of Luminescence*, vol. 134, pp. 266–273, 2013.

[138] E. Zavoisky, "Paramagnetic relaxation of liquid solution for perpendicular fields," *J. Phys. USSR*, vol. 9, p. 211p, 1945.

[139] C. P. Poole, "Electron spin resonance: a comprehensive treatise on experimental techniques," 1996.

[140] S. L. Talagala and I. J. Lowe, "Introduction to magnetic resonance imaging," *Concepts in Magnetic Resonance*, vol. 3, no. 3, pp. 145–159, 1991.

[141] M. M. Roessler and E. Salvadori, "Principles and applications of epr spectroscopy in the chemical sciences," *Chemical Society Reviews*, vol. 47, no. 8, pp. 2534–2553, 2018.

[142] J. A. Weil and J. R. Bolton, *Electron paramagnetic resonance: elementary theory and practical applications*. John Wiley & Sons, 2007.

[143] D. B. Bucher *et al.*, "Quantum diamond spectrometer for nanoscale nmr and esr spectroscopy," *Nature Protocols*, vol. 14, no. 9, pp. 2707–2747, 2019.

[144] T. Oder *et al.*, "Iii-nitride photonic crystals," *Applied Physics Letters*, vol. 83, no. 6, pp. 1231–1233, 2003.

[145] N. Tansu *et al.*, "Iii-nitride photonics," *IEEE Photonics Journal*, vol. 2, no. 2, pp. 241–248, 2010.

[146] J. Li, J. Lin, and H. Jiang, "Growth of iii-nitride photonic structures on large area silicon substrates," *Applied physics letters*, vol. 88, no. 17, p. 171909, 2006.

[147] Q. Zhao *et al.*, "Optical properties of highly ordered aln nanowire arrays grown on sapphire substrate," *Applied Physics Letters*, vol. 86, no. 19, p. 193101, 2005.

[148] S. Zhao *et al.*, "Aluminum nitride nanowire light emitting diodes: Breaking the fundamental bottleneck of deep ultraviolet light sources," *Scientific reports*, vol. 5, no. 1, pp. 1–5, 2015.

[149] G. Piazza, P. J. Stephanou, and A. P. Pisano, "Piezoelectric aluminum nitride vibrating contour-mode mems resonators," *Journal of Microelectromechanical systems*, vol. 15, no. 6, pp. 1406–1418, 2006.

[150] X. Le *et al.*, "Surface acoustic wave humidity sensors based on uniform and thickness controllable graphene oxide thin films formed by surface tension," *Microsystems & nanoengineering*, vol. 5, no. 1, pp. 1–10, 2019.

[151] C. Xiong, W. H. Pernice, and H. X. Tang, "Low-loss, silicon integrated, aluminum nitride photonic circuits and their use for electro-optic signal processing," *Nano letters*, vol. 12, no. 7, pp. 3562–3568, 2012.

[152] W. Wesch *et al.*, "Defect production during ion implantation of various a iii bv semiconductors," *Journal of applied physics*, vol. 65, no. 2, pp. 519–526, 1989.

[153] K. Lorenz and R. Vianden, "Defect recovery in aln and inn after heavy ion implantation," *physica status solidi (c)*, no. 1, pp. 413–416, 2003.

[154] E. Wendler, W. Wesch, and G. Götz, "Defects in weakly damaged ion-implanted gaas and other iii–v semiconductors," *physica status solidi (a)*, vol. 112, no. 1, pp. 289–299, 1989.

[155] S. Miranda *et al.*, "Cd ion implantation in aln," *Nuclear Instruments and Methods in Physics Research Section B: Beam Interactions with Materials and Atoms*, vol. 289, pp. 43–46, 2012.

[156] ——, "Ion implantation of cd and ag into aln and gan," *physica status solidi c*, vol. 9, no. 3-4, pp. 1060–1064, 2012.

[157] M. Borowski, A. Traverse, and J. Dallas, "Structural characterization of ti implanted aln," *Journal of materials research*, vol. 10, no. 12, pp. 3136–3142, 1995.

[158] M. Kanechika and T. Kachi, "n-type aln layer by si ion implantation," *Applied physics letters*, vol. 88, no. 20, p. 202106, 2006.

[159] F. Schiettekatte *et al.*, "Erd, 15n external beam for nrra in air, hirbs: ion beam analysis developments on the hvec en-1 tandem," *Nuclear Instruments and Methods in Physics Research Section B: Beam Interactions with Materials and Atoms*, vol. 219, pp. 430–434, 2004.

[160] S. Khan *et al.*, "Texture of the nano-crystalline aln thin films and the growth conditions in dc magnetron sputtering," *Progress in Natural Science: Materials International*, vol. 25, no. 4, pp. 282–290, 2015.

[161] D. Nilsson, E. Janzén, and A. Kakanakova-Georgieva, "Lattice parameters of aln bulk, homoepitaxial and heteroepitaxial material," *Journal of Physics D: Applied Physics*, vol. 49, no. 17, p. 175108, 2016.

[162] J. Zhang *et al.*, "Growth of aln films on si (100) and si (111) substrates by reactive magnetron sputtering," *Surface and Coatings Technology*, vol. 198, no. 1-3, pp. 68–73, 2005.

[163] W. Wang *et al.*, "Interfacial reaction control and its mechanism of aln epitaxial films grown on si (111) substrates by pulsed laser deposition," *Scientific reports*, vol. 5, no. 1, pp. 1–12, 2015.

[164] B. Pipeleers, S. M. Hogg, and A. Vantomme, "Defect accumulation during channeled erbium implantation into gan," *Journal of applied physics*, vol. 98, no. 12, p. 123504, 2005.

[165] V. Lughi and D. R. Clarke, "Defect and stress characterization of aln films by raman spectroscopy," *Applied physics letters*, vol. 89, no. 24, p. 241911, 2006.

[166] P. Yogi *et al.*, "Interplay between phonon confinement and fano effect on raman line shape for semiconductor nanostructures: Analytical study," *Solid State Communications*, vol. 230, pp. 25–29, 2016.

[167] Y. Gao and P. Yin, "Origin of asymmetric broadening of raman peak profiles in si nanocrystals," *Scientific Reports*, vol. 7, no. 1, pp. 1–4, 2017.

[168] L. Bergman *et al.*, "Raman analysis of phonon lifetimes in aln and gan of wurtzite structure," *Physical Review B*, vol. 59, no. 20, p. 12977, 1999.

[169] J. Wang *et al.*, "Influence of the crystal texture on raman spectroscopy of the aln films prepared by pulse laser deposition," *Journal of spectroscopy*, vol. 2013, 2013.

[170] T. Prokofyeva *et al.*, "Vibrational properties of aln grown on (111)-oriented silicon," *Physical Review B*, vol. 63, no. 12, p. 125313, 2001.

[171] M. Kuball *et al.*, "Raman scattering studies on single-crystalline bulk aln under high pressures," *Applied physics letters*, vol. 78, no. 6, pp. 724–726, 2001.

[172] M. S. Liu *et al.*, "Micro-raman scattering properties of highly oriented aln films," *International Journal of Modern Physics B*, vol. 12, no. 19, pp. 1963–1974, 1998.

[173] L. E. McNeil, M. Grimsditch, and R. H. French, "Vibrational spectroscopy of aluminum nitride," *Journal of the American Ceramic Society*, vol. 76, no. 5, pp. 1132–1136, 1993.

[174] S. Roorda *et al.*, "Structural relaxation and defect annihilation in pure amorphous silicon," *Physical review B*, vol. 44, no. 8, p. 3702, 1991.

[175] L. K. Béland *et al.*, "Replenish and relax: Explaining logarithmic annealing in ion-implanted c-si," *Physical review letters*, vol. 111, no. 10, p. 105502, 2013.

[176] K. Laaksonen, M. G. Ganchenkova, and R. M. Nieminen, "Vacancies in wurtzite gan and aln," *Journal of Physics: Condensed Matter*, vol. 21, no. 1, p. 015803, 2008.

[177] M. Kazan *et al.*, "Oxygen behavior in aluminum nitride," *Journal of applied physics*, vol. 98, no. 10, p. 103529, 2005.

[178] T. Mattila and R. M. Nieminen, "Ab initio study of oxygen point defects in gaas, gan, and aln," *Physical Review B*, vol. 54, no. 23, p. 16676, 1996.

[179] G. A. Slack *et al.*, "Some effects of oxygen impurities on aln and gan," *Journal of Crystal Growth*, vol. 246, no. 3-4, pp. 287–298, 2002.

[180] Q. Yan *et al.*, "Origins of optical absorption and emission lines in aln," *Applied Physics Letters*, vol. 105, no. 11, p. 111104, 2014.

[181] Y. Tang *et al.*, "Synthesis and photoluminescent property of aln nanobelt array," *Diamond and related materials*, vol. 16, no. 3, pp. 537–541, 2007.

[182] M. Lamprecht *et al.*, "Model for the deep defect-related emission bands between 1.4 and 2.4 ev in aln," *physica status solidi (b)*, vol. 254, no. 8, p. 1600714, 2017.

[183] A. Aghdaei *et al.*, "Engineering visible light emitting point defects in zr-implanted polycrystalline aln films," *Journal of Applied Physics*, vol. 128, no. 24, p. 245701, 2020.

[184] S. Jana *et al.*, "Negative thermal quenching and size-dependent optical characteristics of highly luminescent phosphorene nanocrystals," *Advanced Optical Materials*, vol. 8, no. 12, p. 2000180, 2020.

[185] M. A. Reshchikov, "Mechanisms of thermal quenching of defect-related luminescence in semiconductors," *physica status solidi (a)*, vol. 218, no. 1, p. 2000101, 2021.

[186] H.-S. Kwack *et al.*, "Anomalous temperature dependence of optical emission in visible-light-emitting amorphous silicon quantum dots," *Applied physics letters*, vol. 83, no. 14, pp. 2901–2903, 2003.

[187] M. Watanabe *et al.*, "Negative thermal quenching of photoluminescence in zno," *Physica B: Condensed Matter*, vol. 376, pp. 711–714, 2006.

[188] Y. Wu *et al.*, "Negative thermal quenching of photoluminescence in annealed zno–al 2 o 3 core–shell nanorods," *Physical Chemistry Chemical Physics*, vol. 17, no. 7, pp. 5360–5365, 2015.

[189] J. Huang, T. B. Hoang, and M. H. Mikkelsen, "Probing the origin of excitonic states in monolayer wse2," *Scientific reports*, vol. 6, no. 1, pp. 1–7, 2016.

[190] J. Dolado *et al.*, "Li-doping effects on the native defects and luminescence of zn 2 geo 4 microstructures: Negative thermal quenching," *Available at SSRN 4233771*.

[191] H. Shibata, "Negative thermal quenching curves in photoluminescence of solids," *Japanese journal of applied physics*, vol. 37, no. 2R, p. 550, 1998.

[192] L. Wang *et al.*, "Study on carrier lifetimes in ingan multi-quantum well with different barriers by time-resolved photoluminescence," *physica status solidi (b)*, vol. 252, no. 5, pp. 956–960, 2015.

[193] F. Lenzini *et al.*, "Diamond as a platform for integrated quantum photonics," *Advanced Quantum Technologies*, vol. 1, no. 3, p. 1800061, 2018.

[194] M. Cardona and N. Christensen, "Spin–orbit splittings in aln, gan and inn," *Solid state communications*, vol. 116, no. 8, pp. 421–425, 2000.

[195] T.-Y. Seong *et al.*, *III-Nitride based light emitting diodes and applications*. Springer, 2013.

[196] G. Piazza *et al.*, "Piezoelectric aluminum nitride thin films for microelectromechanical systems," *MRS bulletin*, vol. 37, no. 11, pp. 1051–1061, 2012.

[197] M. M. Azmat *et al.*, "First-principles study of antiferromagnetic superexchange interactions between tial-vn complexes in aln," *Journal of Superconductivity and Novel Magnetism*, pp. 1–10, 2022.

[198] J. F. Ziegler and J. P. Biersack, "The stopping and range of ions in matter," in *Treatise on heavy-ion science*. Springer, 1985, pp. 93–129.

[199] S. Stoll and A. Schweiger, "Easyspin, a comprehensive software package for spectral simulation and analysis in epr," *Journal of magnetic resonance*, vol. 178, no. 1, pp. 42–55, 2006.

[200] Y. Qi *et al.*, "Fast growth of strain-free aln on graphene-buffered sapphire," *Journal of the American Chemical Society*, vol. 140, no. 38, pp. 11 935–11 941, 2018.

[201] H. Trodahl *et al.*, "Raman spectroscopy of sputtered aln films: E 2 (high) biaxial strain dependence," *Applied physics letters*, vol. 89, no. 6, p. 061905, 2006.

[202] V. A. Soltamov *et al.*, "Shallow donors and deep-level color centers in bulk aln crystals: Epr, endor, odmr and optical studies," *Applied Magnetic Resonance*, vol. 44, no. 10, pp. 1139–1165, 2013.

[203] V. Soltamov *et al.*, "Identification of the deep-level defects in aln single crystals: Epr and tl studies," *Diamond and related materials*, vol. 20, no. 7, pp. 1085–1089, 2011.

[204] I. V. Ilyin *et al.*, "Deep-level defects in aln single crystals: Epr studies," in *Materials Science Forum*, vol. 645. Trans Tech Publ, 2010, pp. 1195–1198.

[205] A. Pöppl and G. Völkel, "Esr investigation of the oxygen vacancy in pure and bi2o3-doped zno ceramics," *physica status solidi (a)*, vol. 115, no. 1, pp. 247–255, 1989.

[206] F. Froning *et al.*, "Strong spin-orbit interaction and g-factor renormalization of hole spins in ge/si nanowire quantum dots," *Physical Review Research*, vol. 3, no. 1, p. 013081, 2021.